Title

Speciation and Health Risks of Atmospheric Nanoparticulates

Permalink

https://escholarship.org/uc/item/6pn0z7qg

Author

Nguyen, Kennedy Dai

Publication Date

2016

Peer reviewed|Thesis/dissertation

UNIVERSITY OF CALIFORNIA, MERCED

Speciation and Health Risks of Atmospheric Nanoparticulates

by

Kennedy Nguyen

A thesis submitted in partial fulfillment
of the requirement for the degree of
Master of Science
in
Biological and Small-scale Technologies

Committee in charge
Professor Valerie Leppert, Chair
Professor Henry Jay Forman
Professor Vincent Tung
Professor Christopher Viney

2016

The thesis of Kennedy Nguyen is approved by:

_____

Dr. Valerie Leppert, Chair   Date

_____

Dr. Henry Jay Forman   Date

_____

Dr. Christopher Viney   Date

_____

Dr. Vincent Tung   Date

ACKNOWLEDGEMENTS

Shelby Skelton, Joseph Silva, Ian Ojeda-Vasquez, Moses Chun, and all the other students who worked with me in our lab.

My friends from UC Merced, Patrick Gray, Jason Le, Ngoc Tran, Alan Yu, Cristian Ramos, Karen Avalos, Daisy Alvarado, Tracy Fang, Jacob Pinkston, Jonathan Flemming, Kenneth Kao, Patrick Wu, Ivan Tang, Miguel Diaz, Emily Reed, Tzu-I-Chao, Yang Liu, Shelley Wang, who contributed to my professional and personal growth and made my life enjoyable at UC Merced.

A special thanks to the members of the Martial Arts Club, Vietnamese Student Association at UC Merced, and "Rayford's Shorin-ryu Karate and Kobudo" in downtown Merced, CA that provided me with several second homes away from home.

My warm thanks and love goes to siblings: My Duyen, Hung, Hoa, Hiep, Steven, and Nancy, for their continuing support and encouragement.

A shout out to my best friends: Bao Ngoc Rossi Huynh, Vy Thanh Nguyen, Cu Huynh, Linda Trinh Cheung, and Stanley Cheung, keeping me sane throughout my journey with help, advice, encouragement, and food at each stage.

Last but not the least; I would like to thank my parents, Thinh Dai Nguyen and Kieu Thi Vo, for their never-ending love and support.

TABLE OF CONTENTS

ABBREVIATIONS

SEM: *Scanning Electron Microscopy*
SEI: *Secondary Electron Imaging*
BEI: *Backscatter Electron Imaging*
EDX: *Energy-Dispersive X-ray Spectroscopy*
TEM: *Transmission Electron Microscopy*
STEM: *Scanning Transmission Electron Microscopy*
EELS: *Electron Energy Loss Spectroscopy*
ICP-MS: *Inductively Coupled-Plasma Mass Spectroscopy*
ALS: *Advanced Light Source*
STXM: *Scanning Transmission X-ray Microscopy*
XAS: *X-Ray Absorption Spectroscopy*
DLS: *Dynamic Light Scattering*
XRD: *X-Ray Diffraction*
BET: *Brunauer–Emmett–Teller Analysis*
PM: *Particulate Matter*
PAHs: *Polycyclic Aromatic Hydrocarbons*
MCM-41: *Mobil Composition of Matter No. 41(type of mesoporous silica structure)*
VOCs: *Volatile Organic Carbon*
NOx: *Oxides of Nitrogen*
MTT Assay: *3-(4, 5-Dimethylthiazol-2-yl)-2, 5-diphenyltetrazolium bromide) assay*
mRNA: *Messenger Ribonucleic Acid*
RT-PCR: *Real-time Polymerase Chain Reaction*
DPPP: *Diphenyl-1-pyrenylphosphine*
PMA: *Phorbol 12-Myristate-13-Acetate*
TNF-α: *Tumor Necrosis Factor – Alpha*
IL-1β: *Interleukin 1 Beta*
GAPDH: *Glyceraldehyde 3-Phosphate Dehydrogenase*
HO-1: *Heme Oxygenase One*
GCLC: *Glutamate-Cysteine Ligase Catalytic subunit*

ABSTRACT

Exposure to air pollution causes several adverse health effects such as asthma, respiratory disease, cardiovascular disease, cancer, and premature death; and the San Joaquin Valley is one of the most heavily polluted regions in the US. The mountains that surround the valley allow air pollution, including particulate matter, to remain stagnant, prolonging the exposure of valley populations to it. The primary sources of particulate matter for this region are aluminosilicate dust from agricultural activities, and soot emissions from diesel trucks and vehicular traffic. A substantial fraction of emitted material is nanoparticulate matter (<100 nm), which contains trace iron and polycyclic aromatic hydrocarbons that can traverse into human organs via the lungs, initiate inflammation, and lead to disease.

The traditional approach of reducing the total mass of emitted material is beginning to reach its limit of effectiveness for mitigating the negative health impacts of particulate matter. There is a need for chemical speciation of particulate matter that will allow the identification of the chemical and physical properties of particulates by source, the creation of well-controlled proxy particles with those properties for testing in cell culture studies, and correlation of particulate properties and sources with their negative health impacts. These results can help identify the sources of air pollution to prioritize for mitigation for the greatest health benefit. In addition, further chemical speciation can help monitor the results of such mitigation efforts.

Here, natural particulate matter samples from Merced and Fresno, two cities in the San Joaquin Valley, were analyzed. Ultrafine particles present were 40 to 50 nm in diameter and mostly composed of aluminum, silicon, oxygen, and iron hydroxide. XAS data confirmed the presence of the aluminosilicate as smectite clay and the iron hydroxide as ferrihydrite (Fe $(OH)_3$). Furthermore, a chemical speciation study investigated industrial emissions of air particulate matter. Samples were analyzed using electron microscopy for elemental composition and size distribution, and found to contain fine metal particulates (lead and iron) that can lead to lung inflammation.

From characterization data, in order to create a simplified proxy particle system for cell culture studies, amorphous silica particles were synthesized using a modified Stöber Synthesis and coated with iron hydroxide. A range of iron hydroxide concentrations (0.06 to 1.63 mmol of iron per gram of silica) were used to test the effect of iron contamination on THP-1 cells, and higher concentrations of iron with silica (0.43 and 1.63 mmol of iron per gram of silica) were found to increase production of pro-inflammatory mediators compared to silica alone. Iron alone did not induce an effect relative to the control, demonstrating a synergistic effect when iron is combined with silica at low doses. It was found that crystalline silica was more toxic than amorphous silica (70% vs 80% respectively at 100 μg/ml). In addition, mesoporous silica was found to be more toxic than solid silica (73% vs 82% respectively at 100 μg/ml), likely due to a higher surface area (60.2 m^2/g for mesoporous external surface area without internal pores vs 1.72 m^2/g for solid 2 μm silica and 54.5 m^2/g for 50 nm silica) and increased particle loading at the same dose. Finally, a preliminary investigation of Printex 90 as a proxy material for soot, with and without the addition of iron and quinones, was conducted.

CHAPTER 1: Introduction and Literature Review

The San Joaquin Valley (SJV) in California, USA, is at high risk of air pollution exposure, which can increase morbidity and mortality [1]. According to the 2009 US Census, the SJV has nearly 4 million people in its eight counties: San Joaquin, Stanislaus, Merced, Madera, Fresno, Kings, Tulare, and Kern. The SJV cities that contain the most population density and also the highest concentrations of particulate matter (PM) are Stockton in San Joaquin County, Modesto in Stanislaus County, Fresno in Fresno County, and Bakersfield in Kern County [2, 3]. Air pollution can lead to several health risks related to respiratory and cardiovascular health, such as the development of asthma in young children [2]. The SJV can benefit from efforts to reduce air pollution. In the past, the reduction strategies for air pollution focused on decreasing the total mass of emission sources, regardless of the improvements on air quality. Recently, the strategy has been focused on the mitigation efforts with direct improvements in air quality and public health, based on scientific evidence, known as the health-risk based approach [4, 5].

Chemical speciation is the identification of the different chemical and physical properties of elements within a sample [6], beyond simple elemental composition identification. For effective reduction of air pollution, chemical speciation can identify the properties of particulate matter (PM) that have the biggest impact on human health for mitigation strategies, based on biological tests. However, PM can be composed of a variety of constituents with chemical and physical properties that depend on the different sources of its emission, making it difficult to determine which variables cause biological effects, such as inflammation and toxicity. To simplify PM, proxy PM particles are synthesized based on known chemical speciation data of SJV PM. Chemical speciation of the proxy PM particles along with biological tests can be used to determine their health risks by relating their properties to their biological effects. These proxy PM particles can be modified accordingly to further match natural PM and to understand biological effects of specific constituents of PM. Here, we discuss the health risks of particulate matter, the health risk-based approach compared to the mass-based approach to reducing air pollution, the major sources of pollution in the SJV, the importance of chemical speciation, and the reasons behind a proxy particle of air pollution to help improve health conditions in the SJV.

1.1 Particulate Matter and Health Risks

Air pollution particles are a mixture of solids and liquids of varying composition, ranging from completely solid to completely liquid, which can cause respiratory and cardiovascular health diseases [3, 7, 8]. These particles are composed of organic and inorganic matter as well as trace metals [9]. Generally, particulate matter (PM) is defined by its size fractions: less than 10 micrometer (PM_{10}), less than 2.5 micrometer ($PM_{2.5}$), and less than 0.1 micrometers ($PM_{0.1}$ also known as "ultrafine particles") [10]. Over the years, several studies have shown the adverse health effects of exposure to PM, such as increased rates of mortality and morbidity, with the development of respiratory disorders like emphysema and pulmonary fibrosis, particularly in the elderly [10-23].
Exposure can cause illness, hospitalization, and premature death for sensitive groups, such as infants, children, and teens, who are developing their respiratory systems.

Other groups with increased health risks are the elderly (over age 65 years), people with existing respiratory issues (asthma, bronchitis, and emphysema, etc.), those with diabetes, those with cardiovascular disease, and those who work out-doors [3, 24-26]. Even healthy individuals are at risk. A study by Thaller et al. [27], found that moderate increases (even below federal standards) in ambient air pollution decreased lung capacity and increased air way obstruction in lifeguards. There are also health risks with short-term and long-term chronic exposure to air pollution. Air pollution can also fluctuate throughout the day and cause pre-mature deaths for sensitive groups when the PM concentration spikes. Although the exposure during PM spikes may be short-term, a study by Zanbetti et al. [28] found that the effects last more than one month after exposure and can contribute to potential cardiovascular and respiratory deaths [29].

There are several benefits to reducing air pollution. In a heavily polluted urban region, when exposure to fine particulates decreased, then the average life expectancy increased [30, 31]. According to epidemiology study by Correia et al. [32], when comparing data among 545 US Counties between 2000 and 2007, the average life expectancy increased by almost 4 months each time the $PM_{2.5}$ concentration was decreased by 10 $\mu g/m^3$. In a similar study by Pope et al. [31] on 51 US Metropolitan areas from 1970 to 2000, the same decrease in PM concentration increased life expectancy by 7 months. A study by Lepeule et al. [26] found, from studying six cities (1974 to 2009) in the US, that increasing $PM_{2.5}$ concentration by 10 $\mu g/m^3$ was correlated with a 14% increase in all types of mortality, a 26% increase in cardiovascular-related mortality, and a 37% increase in lung-cancer related mortality. A more conservative study by Pope et al. [33] found an increase of 10 $\mu g/m^3$ in fine PM led to an increase in mortality by 4-8%. As these studies show, decreasing the mass concentration of air pollution can potentially save lives, increase life expectancy, and improve human health. However, there are limitations to the mass-based approach, as will be discussed next.

1.2 Reducing Air Pollution: Mass-Based Approach vs. Health Risks-Based Approach

The Clean Air Act and its amendment require all states to focus efforts on reducing air pollution for two National Ambient Air Quality Standards (NAAQS). The primary objective is to protect the general public, especially sensitive groups such as infants, young children, and senior citizens, from unhealthy air exposure. The secondary objective is to protect the environment, which includes improving air visibility and minimizing damage to animals, crops, vegetation, and buildings. The US EPA's six criteria pollutants are carbon monoxide, lead, sulfur dioxide, nitrogen dioxide, ozone, and particulate matter ($PM_{2.5}$ and PM_{10}) [3, 34]. The standard approach to fulfill the NAAQS has been mainly focused on reducing total mass from emissions sources [4].

The Clean Air Act has greatly improved public health in the US since 1970; however, efforts in continuing to reduce air pollution by total mass of emissions will be increasingly difficult and may not be cost effective [4, 8]. Reductions of total source emissions do not necessarily reduce air pollution because different precursors of the same pollutants may have different effects on the environment. For example, under NAAQS planning for ozone reduction, progress was measured by total mass emissions reduction of nitrogen oxide (NOx) and volatile organic carbon (VOCs), two precursors of ozone,

regardless of any net reduction of total ozone concentrations or gain in public health benefits in the region of interest [4]. In this case, VOCs reductions did not affect ozone production in the SJV, but they were still enforced. Clearly, the specific sources identification, such as differences in PM_{10} vs. $PM_{2.5}$ and gasoline vs. diesel emissions vehicles, will make an impact on health risks. A study by Zhou et al. [35] modeled the effects of specific reductions in emissions sources (NOx, SO_2, VOCs, Primary PM, and Secondary PM) and found that reductions of $PM_{2.5}$ and sulfur dioxide would provide the greatest benefits (12,000 less deaths per ton of emissions reduced annually). This shows that mass reduction for one source may have a bigger impact on health risks compared to another. This may be true for other cases, such as fine vs. coarse PM, but we would need further proof [4, 36].

With limited resources, it may be better to focus efforts on strategies that seek to realize the greatest health benefits, rather than simply reducing the total mass of all emissions. Recently, the San Joaquin Valley Air Pollution Control District (SJVAPCD) adopted a health risk based approach as their air pollution strategy, letting science lead the way to target specific pollutants [4, 8]. The targets will be the reduction of emissions that have the greatest effect on public health benefits. For instance, there will be health risks analysis on fine particle emissions vs. coarse particle emissions, nitrogen oxides vs. volatile organic carbon emissions, and primary pollutants vs. secondary pollutants. The measure of progress and success will be based on actual health benefits from air pollution reduction [4]. This requires identification of the sources of air pollution to target for reduction in order to most improve air quality and population health.

1.3 San Joaquin Valley Air Pollution Sources

The major sources of air pollution in the San Joaquin Valley come from PM and ozone. Particulate pollution emits into the atmosphere by mechanical and chemical processes. Bulk materials, such as road dusts, can be mechanically broken down to coarse and finer material with the same chemical properties as the bulk material [37]. The chemical process involves the combustion of fuels and the emission of PM, such as soot [3, 11]. PM emitted directly into the air (such as soot and dust) is primary PM. PM formed in the atmosphere from photochemical reactions or interactions with gaseous molecules is known as secondary PM [8]. Ozone is not emitted, but is formed from photochemical reactions with sunlight, nitrogen oxides (NOx), and volatile organic carbon (VOCs) [8]. Figure 1.1A shows that ozone concentrations increase primarily in the SJV during the summer months [38].

To make matters worse, the SJV's unique geography and climate makes the area efficient at producing ozone and secondary pollutants, while stagnating these pollutants within the region [3, 37]. During the winter months, cooled PM from the mountain slopes traverses to the warmer valley floor. This dense cold air is trapped by the warm daytime air above, concentrating the ground level PM in the SJV [37]. In Figure 1.1B, the average total number of days per month (2002 to 2013) that 24 hour $PM_{2.5}$ concentrations exceed the $PM_{2.5}$ 2006 Standard peak during the winter months [38, 39].

In the SJV, the majority of the coarse air pollution particles come from dust particles. For PM_{10}, the majority of the estimated 2015 emissions in SJV were from miscellaneous processes and natural sources such as farming operations (93.9 tons per

day), road dust (75.8 tons per day), windblown dust (43.8 tons per day), and wildfires (40.5 tons per day). The total estimated 2015 PM_{10} emissions were 318.6 tons per day. In 2015, the major sources for the estimated emissions for $PM_{2.5}$ were from farming operations (13.5 tons per day), road dust (9.3 tons per day), windblown dust (7.5 tons per day), and wildfires (34.3 tons per day). The total estimated emissions for $PM_{2.5}$ were 107 tons per day [40]. The percentages are in Figure 1.2A for PM_{10} and 1.2B for $PM_{2.5}$. For the dust particles, the majority of the sources emit significantly more coarse particles (PM_{10}) than fine particles ($PM_{2.5}$). However, wildfires emit nearly the same mass for either PM_{10} or $PM_{2.5}$. The majority of the sources for PM_{10} are from dust; however, the majority of $PM_{2.5}$ sources are from combustion processes that produce soot.

The elements present will identify the source of the particles in the PM. The primary elements of PM_{10} in road dust, fugitive dust, and farm operations are carbon, aluminum, silicon, potassium, calcium, titanium, and iron, which are part of natural soil [41]. Carbon can also come from soot from diesel exhaust, ground plant debris, and tire wear [42]; and iron can come from fuel combustion in vehicles [43-45]. The different sources of dust may also contain different elements. For example, paved road dust contains lead, carbon, gallium, zirconium, tin, and barium, while construction site dust contains transition metals (titanium, vanadium, and manganese) and toxic metals (palladium, rubidium, and strontium, and thallium) [41]. They can also be correlated with the time, since the SJV has more fugitive dust and coarse iron concentration in the summer and fall, while it has more agricultural, engine exhaust, and wood burning components in the winter [46-48].

There are many different emission sources for air pollution and reducing all emissions may not be a viable option. Some reductions may be more beneficial. Chemical speciation can determine which air pollution components need mitigation for improved air quality.

1.4 Importance of Chemical Speciation for Air Pollution

Chemical speciation is the identification of the various chemical and physical forms of elements within a sample [6]. This is important for establishing the link between these characteristics and their health effects. Within the air pollution literature, there are several trends in PM mass concentration and health effects [15, 30, 49-51]; however, there is limited chemical speciation of the PM itself and its constituents that cause the correlated health effects with mass [52]. PM larger than 10 microns is usually not of concern because the cilia and mucus in the lungs prevent PM from going further into the lungs [53]. However, PM_{10} can enter and deposit deep inside the lungs as far as the bronchioles and alveoli. In addition, $PM_{2.5}$ can travel further into the gas exchange region in the alveoli [53]. PM_{10} is generally composed of salts, carbonaceous materials, metals, ultrafine particles, and biological material. Aside from known toxic substances, such as transition metals, organics, and endotoxins, most of the components of PM_{10} are generally non-toxic. This has led scientists to conclude that ultrafine particles are the cause of the toxic effects of PM_{10} [10, 54, 55].

Chemical speciation of ultrafine particles, which usually occur as aggregates in PM_{10}, can help determine their harmful effects. The toxic effects of the ultrafine particles can be attributed to their smaller size, increased surface area relative to mass, and greater

potential for reaction due to greater surface area [10, 54, 55]. For example, studies on fine and nano-sized titanium oxide and silicon oxide particles revealed that, at the same dose, ultrafine particles gave a greater inflammatory response [56, 57] and silica toxicity was dependent on the particle nano-size and surface area [58-62]. Furthermore, ultrafine particles can readily penetrate the lungs; enter the blood stream; travel to sensitive organs, such as the lymph nodes, spleen, bone marrow, and heart; and potentially impair their function [63]. Studies by Oberdörster et al. [64] found that ultrafine particles respired by rats traversed the lungs to the liver and brain, and Kreyling et al. [65] found that the ability of ultrafine particles to traverse to different regions in the body depends on size.

Chemical speciation may also allow identification of the emission source, which would help target problematic air pollution species for mitigation. This can also be modeled as discussed previously by the Zhou study in China [35]. In addition, chemical speciation can track mitigation efforts and periodic chemical speciation can help determine if reductions of specific emission sources were effective. The changes in the composition with biological tests can determine the health effects. For example, the ban of lead gasoline in the US has greatly reduced the presence of lead near roadways [66] reflecting direct health benefits of the ban. Furthermore, new chemical speciation compositions can correlate with new health risks. For example, chemical speciation can identify the oxidation state of the air particulates and trace transition metals. Studies have found that exposure to silica and carbonaceous nanoparticles induced some inflammatory response, however, the response was enhanced when these particles were oxidized by ozone or contained iron oxide [56, 67].

Natural ambient pollution is complex. As discussed in prior sections, air pollution has many variables and it is difficult to determine exactly which constituent in PM specifically to reduce for the most benefits in public health. Different components in air pollution may be present depending on the region as well. Furthermore, the bulk characterization of particle size, solubility, and chemistry of ultrafine particles from sites in the southern SJV has demonstrated complex mixtures of particulates. These consist of elemental carbon and organic compounds attributed to petroleum and wood combustion, cooking and agriculture, secondary hydrocarbons formed from vehicle emissions, secondary nitrate and sulfate aerosols, and inorganic components associated with mineral and road dust, vegetative burning, agriculture, and marine air intrusion [68-70]. With a multitude of components, it will be difficult to determine which individual components correlate to which the health effects. We need a simple model of air pollution particles to test and determine which variables we need to focus on mitigating to reap the most benefits based on the chemical speciation.

1.5 Importance of Proxy PM System

Due to the complex nature of PM, to test the health effects, we need a simplified proxy PM to test the components identified by chemical and physical speciation. Ultrafine particles are good candidates to model as air pollution particles. Natural sources of human exposure to ultrafine particles are volcanic ash/dust and soot from forest fires. Ultrafine particle exposure has risen since the industrial revolution and will continue to rise [54, 55]. With the rise of nanotechnology, it will be easier to synthesize

nanoparticles to model after ultrafine particles. Nanomaterials are less than 100 nm in diameter and are the same size dimensions as ultrafine particles. Ultrafine particles are complex and contain varying compositions of different trace metals and poly-aromatic hydrocarbons [10, 71]. Aerosols and other contaminants may also be present during their formation due to incomplete combustion of carbonaceous fuels [48, 72-74].

A simple model of PM can be made of nanoparticles for biological tests. Currently, there have been several tests done on nanomaterials in comparison to their bulk equivalents. Nanoparticles can be more toxic compared to micron sized particles [54]. Studies have shown the effects of nano and micron size particles are different for copper, copper (II) oxide and zinc powder. Wang et al. (2006) found that nano-sized zinc powder was more lethal and was more likely to induce lethargy in mice; while Midander et al. (2009) found that nano-size copper oxide was more likely to cause DNA damage and cell death compared to micron sized copper oxide [75, 76]. Due to the greater presence of surface atoms as particle size decreases on the nano-scale, this favors the production of free radicals, which can initiate oxidative stress and inflammation [77]. Many diseases are initiated by long term inflammation [78]; and cytokine mediated inflammation appears to be related to diseases such as Type II diabetes, arthritis, atherosclerosis, asthma, and cystic fibrosis [79-81].

By analyzing ultrafine particles with chemical speciation, the important parameters to test in biological studies for using the proxy PM can be determined and synthesized. Prior work on micrometer and nanometer sized silica particles [57, 82] studied the effects of iron on the silica surface in relation to a pro-inflammatory mediator production mechanism (Figure 1.3). In our previous mechanism, silica interaction with a macrophage receptor activates NADPH oxidase on the cell membrane. NADPH oxidase reduces oxygen molecules to produce superoxide ($O_2^{.-}$). Superoxide can react with iron (III) to form iron (II), and superoxide can dismutate to hydrogen peroxide and molecular oxygen. Iron (II) ions can react with hydrogen peroxide to form hydroxyl radicals [83-86]. The hydroxyl radical can react with the cell membrane, causing lipid peroxidation and leading to enhanced activation of the respiratory burst and production of inflammatory mediators [57, 82]. The proxy particulate systems can test the same or similar mechanisms to see alterative effects.

1.6 Goals

The overarching goal of this work was to develop an understanding of the SJV PM's constituents that are the highest priority for mitigation efforts in order to improve human health. To achieve this goal, PM was collected from two cities in SJV (Merced and Fresno) during the winter, and analyzed to understand the constituents that are present at these locations. This included characterizing PM collected from an automobile shredding plant. Although the specific plant studied was not in the SJV, it is typical of similar plants in the SJV and was therefore of interest as a potential source of particulate matter. The identified proxy particles are silica to represent aluminosilicate road dusts and carbon to represent soot from mobile sources and wildfires. Commercial particles and various synthesis methods used for creating these proxy particle systems tested the specific chemical and physical properties of the resulting systems, followed by preliminary bioassay measurements to assess their toxic potential. For the proxy

particles, iron hydroxide on the surface of the proxy particles represented natural iron on PM. 1,4-Naphthoquinone was used on the carbon particles as a oxidized proxy PM with high carbon content [87] and a representative quinone in diesel exhaust [88]. Mesoporous silica investigations determined the effect of surface area relative to particle size.

1.7 Figures and Figure Legends
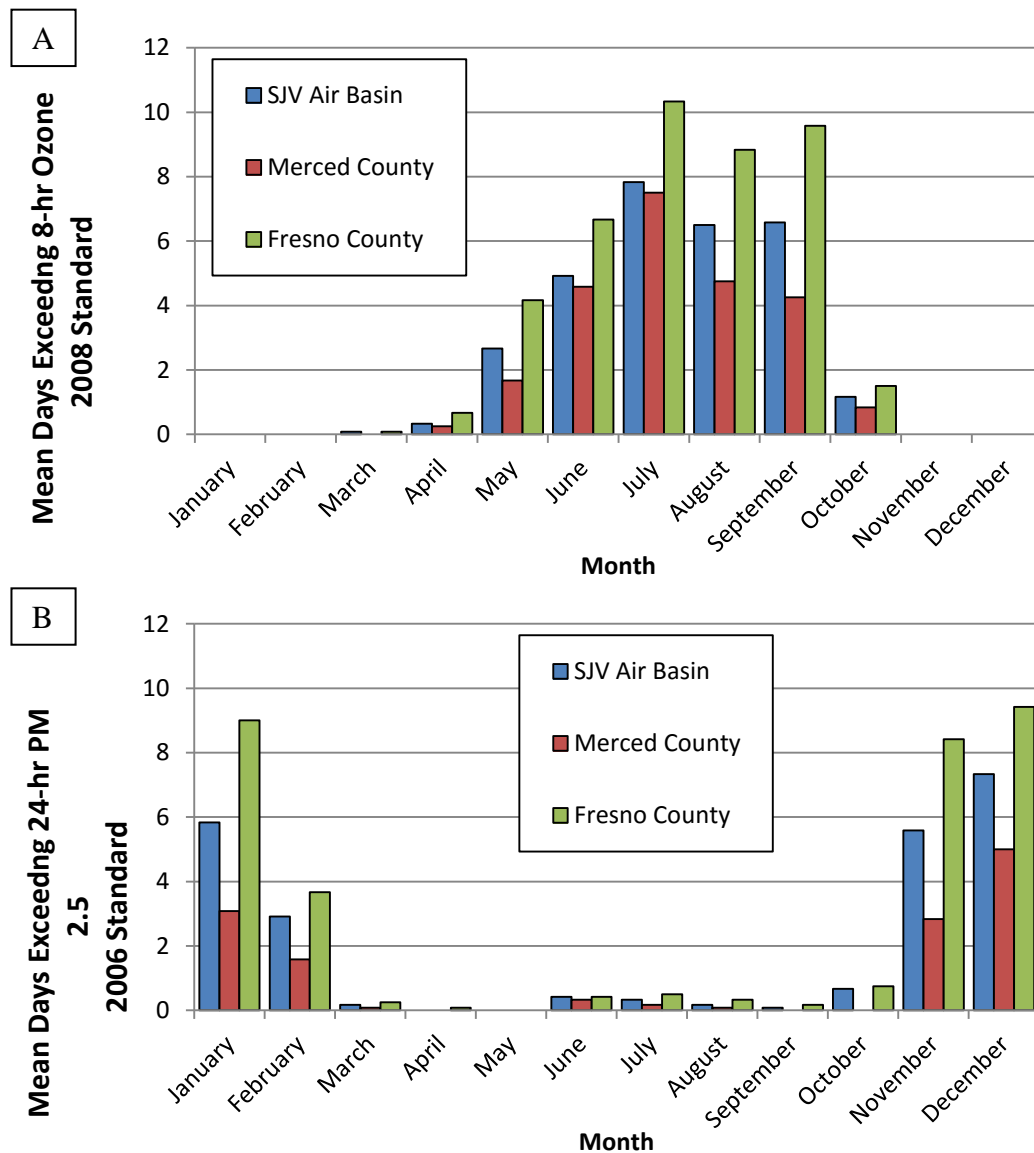
Figure 1.1: Average Monthly Exposures from 2002 to 2013. Average days per month when (A) 8 hr - Ozone Exceeds the "2008 Ozone Standards" (>75ppb) and (B) 24-hour PM 2.5 Exceeds the "2006 PM Standards" (>35 µg/m^3). Source: [38]
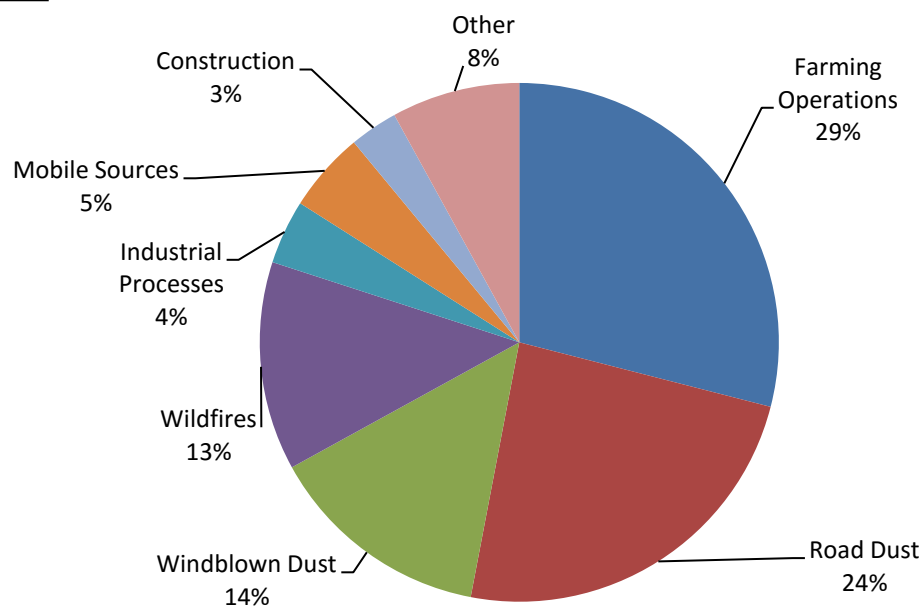
Figure 1.2: Estimated 2015 Particulate Matter Emissions in the SJV. (A) PM_{10} and (B) $PM_{2.5}$. Source: [40].

Extracellular

Intracellular

$O_2^{\cdot-}$: Superoxide
H_2O_2: Hydrogen peroxide
$HO^{\cdot}$: Hydroxyl radical
LOOH: Lipid hydroperoxide
PC-PLC: Phosphatidylcholine specific phospholipase C
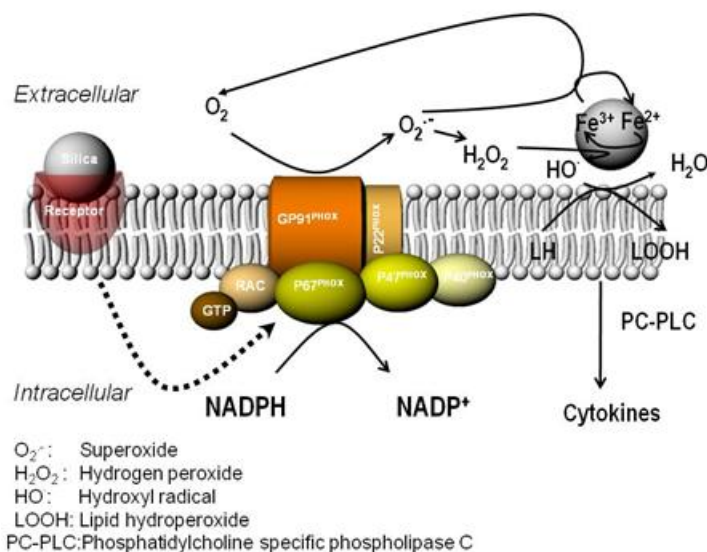
Figure 1.3: Mechanisms of silica surface chemistry and oxidant dependent cytokine production. Silica binds to a macrophage receptor resulting in signaling for activation of NADPH oxidase. NADPH oxide produces $O_2^{\cdot-}$ (superoxide). $O_2^{\cdot-}$ dismutates to H_2O_2 and O_2. $O_2^{\cdot-}$ or by reductants, such as ascorbate, in lung lining fluid or secreted from cells, reduce Fe^{3+} on the silica surface. H_2O_2 reacts with Fe^{2+} in the Fenton reaction to produce hydroxyl radical ($HO^{\cdot}$) which can initiate lipid (LH) peroxidation. Both H_2O_2 and lipid peroxidation products may activate PC-PLC producing diacylglycerol (DAG) which signals for the production of cytokines and enhancement of the respiratory burst.

CHAPTER 2: Experimental Techniques

Several different techniques, such as scanning electron microscopy, transmission electron microscopy, and scanning transmission x-ray spectroscopy characterized the samples collected, synthesized, and prepared. Preliminary biological tests determined the potential health risks of the proxy PM particles.

2.1 Materials Preparation

SEM and TEM characterized the PM particles extracted from their air pollution filters. The proxy PM particles were silica as a proxy for aluminosilicate dusts and Printex 90 as a proxy for diesel soot. Centrifugation size separated the mesoporous silica particles and solid silica particles. The proxy PM particles coated with iron and quinones mimicked natural and anthropogenic air pollution found on the natural samples.

2.1.1 Sample Collection

Particulate air filters collected Merced and Fresno samples: Merced 1/7/12 (#171007121) and Fresno 12/26/11 (#241360111). UC Davis Group 8 stage DRUM impactors collected automobile shredding plant samples from August to September of 2008. The 8-stage collector size separated particles into different size ranges between 10-5.0 µm to 0.26 - 0.09 µm based on aerodynamic diameter, which adhered to greased plastic film for each of the different stages [89]. The plastic collection film moved 1 mm every 6 hours, so each section of the sample corresponded to a date and time. SEM and TEM sections described the sample preparation for analysis.

2.1.2 Silica Size Separation

Using the zeolite particle size-separation technique by Vaniman (2001) [90], both engineered solid (2 µm) and mesoporous silica particles were sonicated and separated to 1-3 µm size fractions with centrifugation. The solid silica particles were uniform in size; however, the mesoporous silica particles were not uniform, but aggregated. Centrifugation size separated mesoporous silica particles and aggregates of similar size to the solid silica particles for biological tests.

2.1.3 Silica Stöber Synthesis

Two different sources of silica tested as a proxy PM particle were 50 nm silica particles purchased from Microspheres and Nanospheres, and 50 nm silica particles synthesized via Stöber synthesis. Commercial samples were in a 5% solution in 10 ml of water and dried as a fine powder, and referred to as Commercial Silica or C-Silica (C-Si) nanoparticles. Solid colloidal silica was synthesized following a modified method by Stöber et al. [91]. First, 28.58 ml of ethanol (Anhydrous, *Fisher Scientific*) mixed with 1.50 ml of 29% ammonium hydroxide (*Sigma Aldrich*) in a glass bottle (100ml, *Wheaton*). A magnetic stir bar stirred the solution for 5 minutes at room temperature. Once mixed, a pipette added 0.75 ml of tetraethyl orthosilicate, TEOS (*Sigma Aldrich*), drop by drop while maintaining vigorous stirring of the solution. Then, the solution stirred for 12 hours. After centrifugation at 10,000 rpm for 10 minutes, decantation removed the supernatant, and DI (deionized) water re-suspended in particles with

vortexing. Samples not dried after syntheses are Synthesized Silica or S-Silica (S-Si) nanoparticles. The evaporation of water from several milliliter sample aliquots determined the average silica mass per volume of DI water. For iron addition, DI water diluted the solution to 2 mg SiO_2/ml.

2.1.4 Iron Coating of Proxy PM

To mimic trace transition metals on the surface of natural PM, proxy PM particles (silica and Printex 90) were mixed with iron solutions following a modified method by Ghio et al. [92]. For iron coated C-Silica nanoparticles, 1 ml of silica in water (2 mg SiO_2/ml) mixed with 1 ml of 1 mM $FeCl_3$ (Ferric Chloride Anhydrous, *Scientific Company*), vortexed and agitated for 15 minutes, equilibrated overnight, and then centrifuged at 10,000 rpm for 10 minutes. Decantation and drying in air for 24 hours at 37°C removed water content, and then DI water re-suspended the particles for TEM and biological tests. As for S-Silica, 1 ml of 2 mg/ml of the silica particles mixed with 1ml concentrations of either 10 and 100 μM $FeCl_3$, vortexed, agitated, rested as above, remained in solution, and then prepared for TEM and biological tests. These coated particles are iron coated C-Silica particles (Fe C-Si) and iron coated S-Silica (Fe S-Si).

For iron coating of Printex 90, 1 ml of Printex 90 (2 mg/ml) mixed with 1 ml of 100 μM $FeCl_3$ solution. Then, samples agitated for 15 minutes via vortexing and then equilibrated overnight on a shaker table for 24 hours.

2.1.5 1, 4-Naphthoquinone Coating of Proxy PM

1, 4-Naphthoquinone (*Fluka*), representative of quinones derived from diesel combustion [88], coated quinone on Printex 90 or P90. A stock solution of 200 mM 1, 4-Naphthoquinone in ethanol diluted 50 fold in ethanol was used to make a 4 mM 1, 4-Naphthoquinone solution. For coating, 1 ml of 2 mg/ml Printex 90 was mixed with 1 ml of 4 mM 1, 4-Naphthoquinone and agitated for 15 minutes via vortexing and a shaker table. This is Quinone-Coated Printex 90 or Q-P90. Both iron and quinone were coated on Printex 90 similar to the previously described methods, except the 1, 4-Naphthoquinone stock solutions used 100 μM $FeCl_3$ for the dilution instead of water. This is Iron/Quinone-Coated Printex 90 or FeQ-P90. A ratio of 1 ml of 2 mg/ml Printex 90 was mixed with 1 ml of 4 mM 1, 4-Naphthoquinone in 100 μM $FeCl_3$. In addition, this protocol coated S-Silica nanoparticles with quinones for cell viability tests as well.

2.1.6 Mesoporous Silica Synthesis of MCM-41

Synthesis of MCM-41 required deionized water, ammonium hydroxide (NH_4OH), cetyl trimethylammonium bromide (CTAB), ethanol (absolute), hydrochloric acid (HCl), and tetraethyl orthosilicate (TEOS). First, 200 ml of deionized water was added to the reaction vessel with temperature control. Then, 6.6 ml of 29% NH_4OH was mixed in the reaction vessel with DI water for 15 minutes with continuous stirring and heating up to 50°C. Once the temperature had reached 50°C, 0.165g of CTAB was mixed with the solution and dissolved completely. After stirring for 30 minutes at 50°C, 0.75 ml of TEOS was stirred with the solution for 3 hours with the heat turned off. At the end of 3 hours, a solution of 40 ml of ethanol and 1 ml HCl was mixed with the solution to stop

the reaction. After 24 hours, the samples underwent centrifugation at 10,000 rpm at 20 minutes, decantation, and re-suspension in water for two times. In the end, samples were dried overnight in air before analysis.

2.1.7 Crystalline Quartz Synthesis

Naturally occurring silica is crystalline quartz [93]. There was an attempt to synthesize nano-sized quartz using hydrothermal synthesis of the 50 nm non-crystalline silica from the Stöber synthesis. The crystalline silica particles would be a better representation of natural road dust compared to non-crystalline colloidal silica. To make crystalline quartz, the modified procedure by Jiang et al. [94] was used. A 300 ml PARR reaction vessel was used for synthesis of crystalline quartz. For the synthesis, 71.5 g of silica colloidal solution (~ 2 g of silica by weight) was mixed with 1.65 g of NaOH and 4.3 g of NaCl in a Teflon coated autoclave and maintained at ~200°C and ~15 MPa with spinning at 1000 rpm for three days. TEM and XRD results verified the resulting product.

2.2 Scanning Electron Microscopy Characterization

Scanning Electron Microscopy (SEM) determined the size distribution and morphology of the samples with imaging. Energy Dispersive X-Ray Spectroscopy (EDX) with the SEM determined the elemental composition of the samples.

2.2.1 Imaging

An FEI Quanta 200 Scanning Electron Microscope equipped with a tungsten filament (4 nm spatial resolution) was used to analyze the PM and proxy PM particles. The typical acceleration voltage was between 20 to 30 kV. The SEM creates images based on the signals from secondary electrons and backscattered electrons (Figure 2.1). Secondary electrons are low energy electrons (>50 eV) formed from inelastic scattering. Secondary Electron Imaging (SEI), using an Everhart-Thornley Detector, identified surface topography, particle morphology, and size distribution of the samples. The electron beam was rastered across the sample, generating secondary electrons at each point of the sample. The intensity of each point was dependent on the amount of secondary electrons collected by the detector as the electron beam interacted with each point. This provided a virtual image of the sample via an intensity map of the sample. The SEM was used to image various magnifications for an overall view of the sample and at least 10 different random regions to determine size distribution for the particles.

Backscattered electrons formed from elastic scattering when the beam electrons interacted with the sample. Backscattered Electron Imaging (BEI) was used to determine the atomic number contrast in the sample using a solid-state backscatter detector. The BSI image formed similarly to SEI but with backscatter elections, instead of secondary electrons. Heavier elements appeared brighter and light elements appeared less bright with respect to the signal intensity [95]. Atomic number contrast helped identify the heavier elements in air pollution samples, such as transitions metals [95], and helped distinguish them from carbon and silicon (from soot or dust), which were lower atomic number elements. In samples with heavier elements, BEI was used to identify regions within the sample for EDX scans. Knowledge of the physical morphology and chemical

composition would help identify the source of the PM and verify if the proxy particles have the properties that are of interest to test for biological tests.

2.2.2 Energy Dispersive X-Ray Spectroscopy

An SEM equipped with an EDAX Energy-Dispersive X-ray Spectroscopy detector with ultrathin window (132 eV energy resolution) and pre-cooled with liquid nitrogen was used to determine the elemental composition of the sample. As shown in Figure 2.2, the electron beam/sample interaction also produced X-rays. Beam electrons ionize the sample atoms by ejecting an inner shell electron and leaving an unoccupied electron energy state in the inner shell. An outer shell electron can fill the unoccupied state by transitioning from the outer shell to the inner shell, which produces an X-ray characteristic of the difference in energy between the outer shell and the inner shell states. The X-rays produced are therefore characteristic of each element [95]. Full scans showed representative spectra of each sample. Spot scans were done on areas where specific elements were identified.

2.2.3 SEM Sample Preparation

For the samples on air filters, sample scraping did not remove the particles off the filter. Therefore, the samples were prepared by directly viewing the filter in the SEM (double-sided carbon tape on aluminum stub). Alternatively, carbon tape directly applied to the filter removed the particles off the filter via peeling. The SEM micrographs verified successful removal of sample off the filter and on to the carbon tape. Sample preparation for the automobile shredder plant samples collected by the DRUM impactors involved cutting out of the plastic film and taping them on the aluminum stub for SEM observations with EDX. Preparation for the other powdered samples of proxy PM involved suspending the power in deionized water, and adding a drop of the suspension on carbon tape, and then allowing the solution to dry in vacuum before analysis. Mesoporous silica and solid, nonporous silica (2 μm diameter) were prepared similarly.

2.3 Transmission Electron Microscopy

Transmission electron microscopy (TEM) was used to image particles on the nanoscale. As shown in Figure 2.1, the electron beam/sample interaction produced signals for Electron Diffraction, EDX, and Electron Energy Loss Spectroscopy (EELS). Electron Diffraction helped identify the crystal structure present. EDX analysis determined chemical composition, similarly to SEM. Scanning Transmission Electron Microscopy (STEM) was used to image the sample and form a fine probe for EELS acquisition. EELS analysis determined chemical composition, bonding, and oxidation state.

2.3.1 Imaging

Similar to SEM, size distribution was determined for the PM and proxy PM particles by random sampling of different areas on the TEM sample. A JEOL JEM2010, 200 kV with a LaB_6 electron source (2.4 Å point-to-point image and 1.4 Å lattice fringe resolutions) was used to image the samples for TEM. TEM imaging was done for all the

PM particles (including the automobile shredder plant), proxy PM particles (silica and Printex 90), and mesoporous silica samples.

STEM was essentially operating in SEI mode, like in the SEM, but on a TEM sample. The probe size needed to be much smaller in STEM to raster across the sample and to provide enough surface information on the nanoscale. A Philips CM200 transmission electron microscope, operating at 200 kV and equipped with a field emission gun, operated in STEM mode for imaging and EELS analysis at National Center for Electron Microscopy (NCEM) at Lawrence Berkeley National Laboratory (LBNL). STEM, with a probe size of 1.4 nm and the probe current of 1 nA, was used to image the proxy PM particles to verify the presence of either the iron oxide or quinone coatings.

2.3.2 Energy Dispersive X-Ray Spectroscopy

An EDAX Energy-Dispersive X-ray Spectroscopy detector with ultrathin window (132 eV energy resolution), pre-cooled with liquid nitrogen, was undertaken using the JEOL2010 TEM. The signals obtained in TEM were similar to SEM. However, TEM provided more energy to produce X-rays from a greater range of elements in the sample. Also, since the samples in TEM are thin (>100 nm), EDX in TEM provides improved spatial resolution compared to SEM. EDX in the TEM verified the chemical composition and determined if other chemicals were present compared to EDX with the SEM.

2.3.3 Electron Diffraction

Diffraction was used to determine the crystal structure of the sample. A distinct diffraction pattern indicated the presence of specific crystal structures in the sample. The R or the distance between the transmitted beam (center of diffraction pattern) and diffraction spots provided information related to d, the d-spacings of the planes in the crystal structure from the equation, "$Rd = \lambda L$" (Figure 2.3). L is the camera length, and λ is the wavelength of the beam electrons. Together, "λL" is the camera constant and used to determine the d-spacings of unknown crystal structures. To calibrate the diffraction patterns, all diffractions patterns had the same eucentric height, camera length, and objective focus as a reference point. Using the equation, the measured R-values from a gold standard sample, and the known d-spacings of gold, a camera constant of 23.33 nm·pixel was determined. When an unknown diffraction pattern was analyzed, the d-spacings were determined by using the camera constant and measured R-values on the unknown diffraction pattern. Diffraction databases were used to help identify the unknown samples. Electron Diffraction characterization was performed using a JEOL JEM2010 operated at 200 kV with a LaB_6 electron source.

2.3.4 Electron Energy Loss Spectroscopy

EELS measured the energy loss of the beam electrons as they passed through the sample. Theoretically, all beam electrons are of the same energy. As they pass through the sample, inelastic scattering will cause the electrons to lose energy which is related to the element composition, bonding, thickness, and oxidation state of the sample [96]. An example of an EELS spectrum is shown Figure 2.4. The "zero loss peak" is from the transmitted beam. Plasmons are collective oscillations of free electrons in the sample from electron beam interactions. Other signals are characteristic of the sample. EELS

data were collected (energy dispersion of 0.3 eV per channel, with an energy offset of 500 eV to observe oxygen and iron) to determine the oxidation state of proxy PM. Full width at half maximum (FWHM) of the zero-loss peak measured under vacuum was approximately 0.9 eV. The FWHM determines the resolution of the EELS spectra.

Pearson's method was used to determine the L_3/L_2 Intensity ratio of the iron oxide present on proxy PM following a method by Jasinski et al. [97]. In EELS, the area under the L_3 and L_2 peaks correlate with the oxidation state of iron oxide. Using Pearson's method, first, background subtraction removed the background signal from the L_3 and L_2 peaks (Figure 2.5). Then, two Gaussian peaks modeled the L_3 peak, and another two Gaussian peaks modeled the L_2 peak. The areas under the respective Gaussian peaks for L_3 represented the intensity for L_3 and similarly for the intensity for L_2. The L_3/L_2 intensity ratio compared to known ratios identified the iron oxide present. In addition, the iron and oxygen energy loss peak features helped to verify the unknown samples with the known iron samples as shown in Figure 2.6.

2.3.5 TEM Sample Preparation

For the Merced and Fresno samples from air filters, the TEM sample preparation involved a drop of either ethanol or water on the air particle filter with a copper holey carbon TEM grid placed on top. After drying in vacuum, the TEM grid was used to peel the particles off the filter for imaging. For the proxy samples in suspension, TEM analysis was done after a drop of the suspension was dried on a TEM grid overnight in vacuum. For the automobile shredder plant, hexane solution was used to remove the particles from the collection film. Using centrifugation (15,000 rpm for 10 minutes), the hexane separated the grease from the particles for placement on a copper holey carbon TEM grid. Removing the grease off the particles was important to prevent hydrocarbon and outgassing from the grease interacting with the electron beam. TEM was also used to preview samples for STXM on a Si_3N_4 membrane window grid.

2.4 Scanning Transmission X-ray Microscopy

Scanning Transmission X-Ray Microscopy (STXM) is a combination of microscopy and X-ray Absorption Spectra (XAS). STXM is used for elemental mapping (imaging) with a 20 nm resolution, while XAS can be used to determine the electronic state of matter, such as the oxidation state [98]. STXM is similar to STEM, while XAS is similar to EELS in TEM. The major difference is that STXM/XAS uses X-rays, while STEM/EELS uses electrons. An X-ray hits the sample and the intensity of X-rays as it scans the sample is recorded (Figure 2.7). However, another advantage of XAS is that there is less beam damage compared to EELS, and it can easily analyze water and carbon samples.

Beamline 5.3.2 (Polymer STXM) at Lawrence Berkeley National Laboratory (LBNL) was used to collect STXM data. The sample was deposited onto a 100 nm thick Si_3N_4 window and air-dried for STXM measurements. STXM measurements had a spatial resolution of 31 nm and an energy resolution of ~0.15 eV at the iron L-III edge. Particle aggregates were imaged in transmission at energies below and at the relevant absorption edge. Energies were converted into optical density images (OD) calculated by OD (E) = -log [I (E)/I_0 (E)], where I(E) and I_0(E) are the average transmitted X-ray

intensity of the sample and background, respectively, at a given energy E. Energy calibrations for C and O used CO_2 gas. Line and area (stack) scans were collected at the iron L-III edge (680-750 eV) with 0.1 eV steps over the edge region with a 10 ms dwell time. Stacked image alignment used a spatial cross-correlation analysis and spectra extracted from groups of pixels from regions of interest using the aXis2000 software package. A blank Si_3N_4 window normalized the transmission signal obtained from the areas of interest. Optical microscopy determined particle dispersion and thickness before analysis in the beamline.

Beamline 4-1 and 4-3 at the Stanford Synchrotron Radiation Light Source (SSRL) was used to collect X-ray absorption spectra (XAS) at the Fe K-edge on bulk samples of Fe-treated silica. Tape was used to seal the packed wet and dry samples in their sample holders. A photoelectric Passivated Implanted Planar Silicon (PIPS) detector (Canberra) and a 4-element SiLi Vortex ME-4 detector (Hitachi) was used to collect fluorescence spectra at room temperature. For comparison, a 32-element Ge solid-stat detector (Canberra) was used to collect one sample at a low temperature in a liquid N_2 cryostat. Energy calibration was based on a metallic Fe foil (first inflection on the absorption edge set to 711.2 eV). Multiple averaged scans showed no changes in spectra observed during data collection. Reference compound ferrihydrite was synthesized following the method of Cornell and Schwertmann [99] by titrating a 0.06 M $FeCl_3 \cdot 6\ H_2O$ solution (made with CO_2-free ultrapure water) with 1 M NaOH until a pH between 6.0 and 6.5 was reached while vigorously stirring; NaOH was then slowly added until the final pH of 7.0 ± 0.2. The formed precipitate was centrifuged for 15-20 minutes, washed with 500 mL DI water until the EC in the supernatant was $\leq 10\ \mu S/cm$, and dried at room temperature. Reference goethite was synthesized by the procedure given in O'Day et al. [100]. Ferrihydrite and goethite solids diluted with sugar had EXAFS spectra collected in either fluorescence or transmission. A spectrum of Fe (III) chloride aqueous solution (50 μM) was collected in fluorescence as a standard reference. ATHENA software was used to analyze the XAS data [101]. Background subtraction from the spectra was accomplished through linear fits in the pre-edge and a cubic spline above the absorption edge to normalize to the post-edge step height.

2.5 X-Ray Diffraction

X-Ray Diffraction (XRD) was used to determine the bulk crystal structure of the samples. An incident X-ray hits the sample and the intensities of diffracted X-ray angles, Θ, are measured. Bragg's law defines the relationship between the measured angles, Θ, and the d-spacings by the equation: $n\lambda = 2d\sin\Theta$, where n is the diffraction order (n = 1 for simplicity), λ is the wavelength of the X-rays, and d is the d-spacing (Figure 2.8). The XRD database identified the unknown crystals from the generated XRD spectra of the samples.

A PANalytical X'Pert PRO Theta/Theta Powder X-Ray Diffraction System with X'Celerator Detector and a 15-position sample changer for high speed, high-resolution phase analysis, and XML-based software for data collection and data evaluation was used to analyze samples. The X-Ray Diffractometer had a solid-state X-ray generator (max. 60 kV, 50 mA); sealed Co X-ray tube (long-fine focal spot); theta-theta goniometer (accuracy +/- 0.0025°, step resolution 0.0001°, 2-theta measuring range 0-167°, scan

speed 0.001-1.3° per second); solar slits; incident and detector anti-scatter slits. XRD data was collected in Θ-Θ mode with a Co X-ray source (K_α 0.1790 nm) to minimize X-ray absorption (56.25 cm^2/g mass absorption coefficient for Co $K\alpha$ X-Rays in iron compared to 304.4 cm^2/g mass absorption coefficient for Cu K_α X-rays in iron) [102]. Powdered samples were prepared on a zero background holder for analysis.

2.6 Inductively Coupled Plasma Mass Spectrometry

Inductively Couple Plasma Mass Spectrometer (ICP-MS) provided information on the chemical composition of metal and non-metals at low concentrations. Mass spectroscopy was used to quantify the samples after inductively couple plasma was used to ionize the samples. An Agilent 7500 ICP-MS (detection limit for iron: 2 µg/L or ppb) was used to quantify the amount of total iron associated with silica particles. All samples were dried completely in an oven at 70ºC before ICP-MS analysis. Depending on the sample amount, 0.01-0.05 g of dry sample was transferred on the Teflon holders, and then 9 ml concentrated hydrochloric acid with 3 ml of concentrated nitric acid was mixed with it. The samples underwent microwave digestion at 160ºC and 18 atm for 40 minutes. Ultrapure DI water was used to dilute two separate aliquots (0.1 and 1 ml) of digested material up to 5 ml total volume to 2% HNO_3 v/v concentration for ICP-MS analysis (weights were recorded). Six standard iron solutions (0.3 – 45 µM) were freshly prepared. ICP-MS in H_2 gas mode was used to determine the iron concentrations. The iron coated proxy PM samples were tested for iron.

2.7 Dynamic Light Scattering

Dynamic light scattering (DLS), also known as Photon Correlation Spectroscopy, was used to determine the hydrodynamic diameter of particles within a fluid by passing monochromatic light into a solution with the target particles. The particles in Brownian motion cause a Doppler Shift when the light hits the moving particle, changing the wavelength of the incoming light. This change correlated to the size of the particle. DLS was used to analyze the particle diameter of the mesoporous silica and solid silica for size distribution in solution.

2.8 Brunauer-Emmett-Teller Analysis

Brunauer-Emmett-Teller (BET) analysis or nitrogen adsorption was used to determine the surface area of the particles with a monolayer of nitrogen gas deposited on the surface of the particles. The pressure correlated with the amount of nitrogen molecules present. Using the diameter of the nitrogen molecule with the amount of known nitrogen molecules, the surface area was calculated. BET analysis was used on the proxy PM particles and mesoporous silica particles to determine their surface area. Samples were weighed and heated near 100°C to remove any residual water for one hour. After cooling, the measured weight determined the dry weight of the samples without water. Afterwards, the BET instrument was used to calibrate the surface area using standards, such as carbon black and silica pellets, while analyzing the sample. In addition, the Harkins-Jura equation ($t = (13.99/(0.034 - \log p/p_s))^{1/2}$) was used to determine t, the thickness of nitrogen gas (N_2) layers in angstroms, based on the relative

pressure (p/p_s); then, the resulting thickness was plotted against the adsorbed gas layer as described in Leofanti et al. [103]. The internal surface area, external surface area, and pore volume were determined from the slope and y-intercept of the lines in the t-plot.

2.9 Surface Charge

Surface charge of particles was determined with titrations of an electrolyte solution of 10^{-3} M NaCl in a closed apparatus with nitrogen flow. The procedure was done following the methods by Michael and Salis [104, 105] and was slightly modified to account for the surface area of nanoparticles. Three solutions were prepared: one with electrolyte and two with electrolyte with different masses of silica. First, 1 M HCl was used to acidify the solutions below pH 3 and then, 1 M NaOH was used to titrate the solution to determine the amount of OH needed to change pH 4 to 9. The point of zero charge is where the electrolyte solution and silica/electrolyte solution pH value is constant (typically near pH 2 for silica). The surface charge at a specific pH, σ_{pH}, is defined by: $\sigma_{pH} = (F \Delta n_{pH})/ (S_{BET} m)$, where F is Faraday's constant, Δn_{pH} is the change of moles of NaOH between the silica/electrolyte solutions versus electrolyte alone at the same pH, S_{BET} is the BET surface area, and m is the mass [104].

2.10 PM$_{2.5}$ Chemical Analysis

PM$_{2.5}$ samples were collected at various sites in the SJV for chemical analysis. As shown in Figure 2.9, chemical analysis was used to measure multiple parameters for the PM$_{2.5}$ samples based on the filters (Teflon, Nylon, or Quartz) collected. On the Teflon-membrane filter, X-Ray Fluorescence (XRF) was used to analyze the elements present, specifically metals. The glass denuder prevented acid gasses from adhering to the filter, in cases where these gasses would interfere with the analysis. On the denuded Teflon-membrane filters, a gravimeter was used to measure particulate mass, and ion chromatography measured water-soluble ions (sulfate, nitrate, ammonium, potassium) [106]. Ion chromatography was used to separate the ions present and determine their concentration [107]. On the quartz filters, organic carbon (OC) and elemental carbon (EC) were measured by thermal/optical reflectance [108]. Operational blanks (unexposed filters) were used to determine background contamination of each sample. SJVAPCD analyzed this data.

2.11 Bioassays
2.11.1 Cell Culture

THP-1 cells, a human monocytic cell line derived from an acute monocytic leukemia patient, were cultured in RPMI 1640 (ATCC, CA) supplemented with 10% fetal bovine serum (FBS) (Omega Sci., CA), β-mercaptoethanol, 100 µg/ml penicillin, and 100 µg/ml streptomycin in 5% CO_2 at 37°C. They were then differentiated using a standard method [109-111] into adherent macrophages by treatment with 50 ng/ml phorbol 12-myristate-13-acetate (PMA) for 3 days. The THP-1 cell line can be differentiated to macrophages following stimulation with PMA or 1,25-dihydroxyvitamin D3 (VD3) [112]. In recent years, THP-1 cells have been widely established as an in vitro model for native monocyte-derived macrophages in studies of macrophage involvement in

inflammatory disease.

2.11.2 MTT Assay

The MTT (3-(4, 5-Dimethylthiazol-2-yl)-2, 5-diphenyltetrazolium bromide) assay was used to evaluate the toxicity of the different particles using concentrations of 1 to 100 μg/ml treated on THP-1 human monocyte-derived macrophages for 24 hours at 37 °C. After 24 hours treatment, MTT dissolved in serum free media was incubated with the cells for 2 hours at 37 °C to allow the MTT crystals to enter the cells. Then, MTT solubilization solution (10% Triton X-100 plus 0.1 N HCl in anhydrous isopropanol) was used to solubilized the cells. After dissolving the formazan crystals, the cell viability was determined based on the absorbance at 570 nm, with background absorbance at 690 nm subtracted. The control sample with no particle treatment had 100% cell viability. Silica nanoparticles may interfere with the MTT absorbance reading according to the literature [113, 114], so this experiment tested the individual effects of silica, MTT, and dead cells for interference. A 50% control verified that the test could show 50% viability for a sample with half the number of cells as the control with 100% cell viability. The silica interference was determined to be minimal and did not have a significant effect on the absorbance readings.

2.11.3 Gene Expression mRNA Assay

Tumor Necrosis Factor-alpha (TNF-α) and Interleukin-1 beta (IL-1β) are two important cytokines involved in inflammation [115]. Real-time Polymerase Chain Reaction (RT-PCR) was used to measure the mRNA expression for TNF-α and IL-1β. THP-1 differentiated macrophages (2 x 10^6 cells/well) were differentiated in a 6-well flat bottomed tissue culture plate, treated with particles at various (3, 6, 18) hours, and washed with PBS. Trizol reagent was used to extract total RNA, and the DNA-free reagent was used to treat the total RNA according to the manufacturer's protocols. TaqMan reverse transcription system (Applied Biosystems) protocol was used to prepare the DNA-free RNA samples for RT-PCR, and a Cepheid 1.2 RT-PCR machine ran RT-PCR. Reverse transcription reaction product (5 μl), 12.5 μl SYBR Green PCR Master Mix, a primer pair specific for cytokine mRNA, and diluted deionized water for a total PCR solution of 25 μl was mixed for PCR. Glyceraldehyde-3-Phosphate Dehydrogenase (GAPDH) was used as an internal control and the primers used were: TNF-α sense 5'-GCCTCTGTGCCTTCTTTTGA-3' and antisense 5'-GCAACCTTTATTTCTCGCCA-3'; IL-1β sense 5'-CGACACATGGGATAACGAGGCTT-3' and antisense 5'-TCTTTCAACACGCAGGACAGGTA-3' and GAPDH sense 5'-ACCCCCAATGTATCCGTTGT-3' and antisense 5'-TACTCCTTGGAGGCCATGT-3'. The relative mRNA quantification used the comparative $\Delta\Delta C_t$ method on threshold cycles (C_t) in logarithmic phase for all samples. This method determined the mean threshold cycle values (C_t) for the control and cells treated with proxy PM to check for IL-1β, TNF-α and GAPDH. The differences between the mean C_t for control/treated cells and the reference gene, ΔC_t, defined ΔC_t (treated cells) and ΔC_t (control). $\Delta\Delta C_t$ was the difference between ΔC_t (treated cells) and ΔC_t (control). The relative mRNA quantification was $2^{-\Delta\Delta Ct}$. The mRNA gene expression for GCLC (glutamate-cysteine ligase catalytic subunit) and HO-1 (Heme oxygenase 1) used the following possible

primers: GCLC sense, 5'-GGATTTGGAAATGGGCAATTG-3', GCLC antisense, 5'-CT CAGATATACTGCAGGCTTGGAA-3'; and HO-1 sense, 5'-ATG GCCTCCCTGTACCACATC-3', HO-1 antisense, 5'-TGTTGCGCTCA ATCTCCTCCT-3'.

2.11.4 Diphenyl-1-pyrenylphosphine Assay

In addition, fluorescent probe Diphenyl-1-pyrenylphosphine (DPPP) Assay was used to estimate the amount of lipid peroxidation caused by 24 hours of silica treatment. Lipid peroxidation indicates that the cell membrane oxidized from resulting interactions with silica. The cells (THP-1 human monocyte-derived macrophages) were mixed with 50 µM DPPP dissolved in 0.05% dimethyl sulfoxide for 10 minutes in the dark, and then treated with 100 µg/ml silica particles for one hour. Afterward, 1 X phosphate buffered saline (PBS) was used to wash the cells several times (2-3 times) to remove any DPPP not present inside the cells. A Nikon C1 confocal microscope was used to image the fluorescence intensity of DPPP oxide (DPPP=O) at an excitation of 351 nm and an emission of 380 nm.

2.11.5 Statistical Analysis

The mean ± standard deviation for each sample represented averages of three experiments, each using three experimental points, with control values subtracted from that of the sample, when compared to silica. One-way ANOVA and one-tailed unpaired student's t-test used $*p < 0.05$ for significance testing. For multiple data comparisons, one way ANOVA used post-hoc analysis. BCA protein assay normalized all data values for all the experiments.

2.12 Figures and Figure Legends
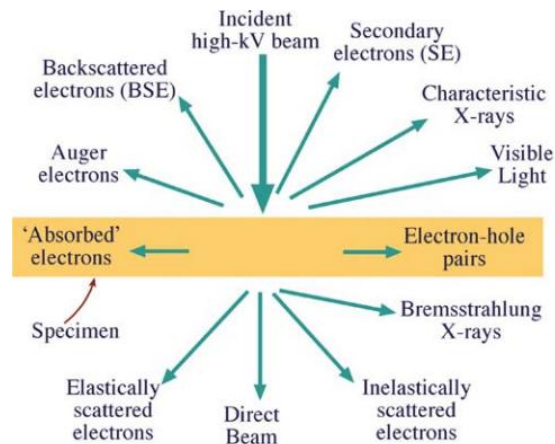
Figure 2.1: Signals for Electron Microscopy detection. The SEM detects most of the signals above the samples and Bremsstrahlung X-rays. The TEM detects nearly all of the other signals depending on its operation mode. (Figure 1.3 from Williams and Carter [96])
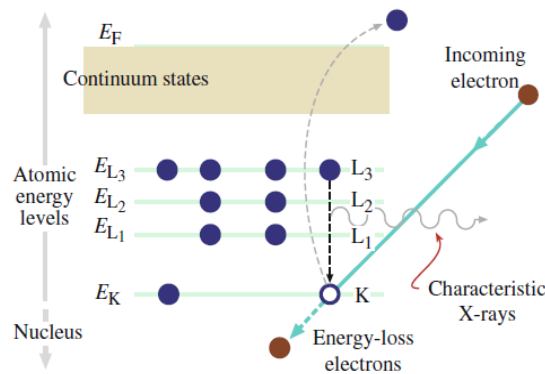
Figure 2.2: Characteristic X-Ray production in EDX. The incident beam electrons ionize an atom in the sample by ejecting an electron from the inner shell electrons and forming a vacancy. Then, an outer shell electron can go down in energy to fill the vacancy in the inner shell. This loss in energy produces an X-Ray that is characteristic for the element. (Figure 4.2 from Williams and Carter [96])
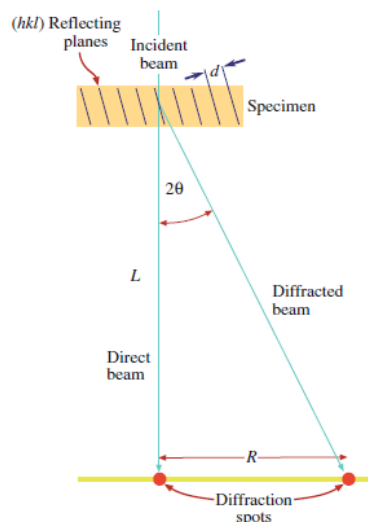
Figure 2.3: Relationship between R, L, and d in the diffraction pattern. (Figure 9.23 from Williams and Carter [96])
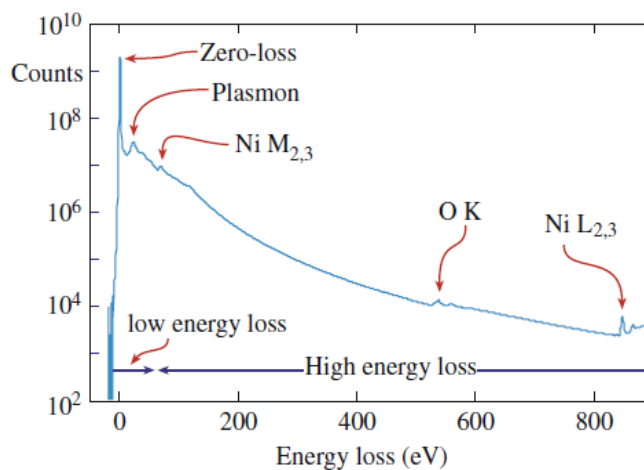
Figure 2.4: Example of EELS. Zero loss peak comes from transmitted electron beam. Plasmons arise from oscillations from the free electrons in the sample. Other signals are characteristic of the bonding, oxidation, and elements present. (From Figure 37.1 in Williams and Carter [96])
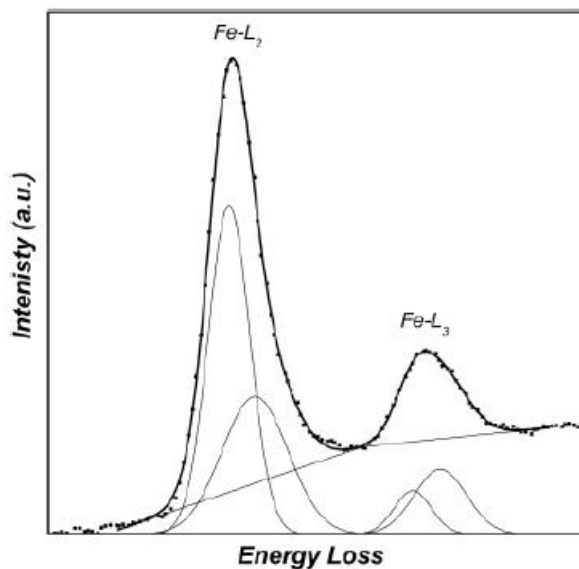
Figure 2.5: Pearson's Methods for L_3/L_2 intensity ratios. The method removes the background signal and two Gaussian functions model the two peaks. The sums of the areas of two Gaussian peaks under the iron peaks determine the intensity of the respective iron peak. The ratio of both peak intensities determines the L_3/L_2 intensity ratio. (Figure 5 from Jacsinki [43])
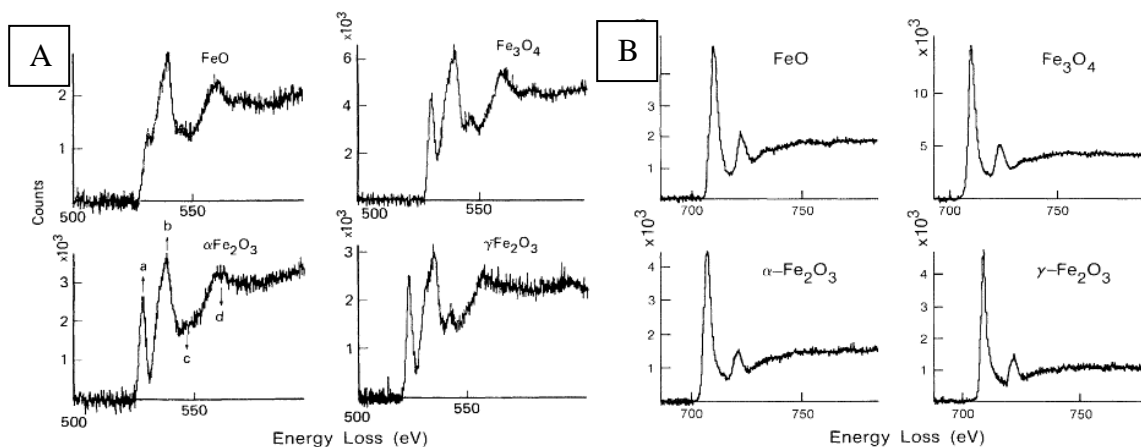
Figure 2.6: EELS Comparison of (A) oxygen K spectra and (B) iron L3, L2 spectra for different iron oxides. (Figures 3 and 4 from Colliex [116])
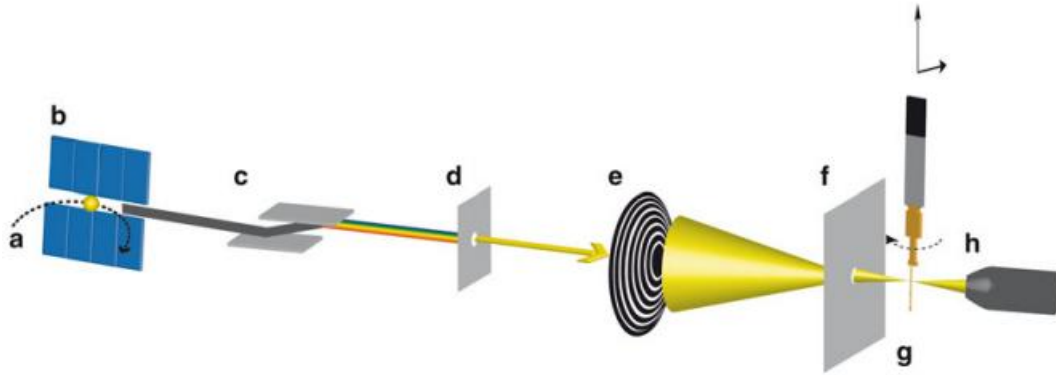
Figure 2.7: STXM setup of a synchrotron undulator-based STXM beamline in standard configuration (not to scale). An evacuated storage ring (a) stores electrons and an undulator (b) generates synchrotron radiation. A monochromator (c) allows for controlling the energy of the incident soft X-ray beam. Exit slits (d) select the energy range and control the intensity of the beam. A Fresnel zone plate (e) focuses soft X-rays on the sample. An order-sorting aperture (f) blocks non-focused zeroth-order light. The sample is raster scanned in x- and y-direction and for tomography measurements additionally rotated in the beam path by a stepper motor mounted on a STXM sample plate (g). A phosphor scintillator in front of a photomultiplier tube (h) detects the transmitted photon signal (Figure 1 from Obst [117])
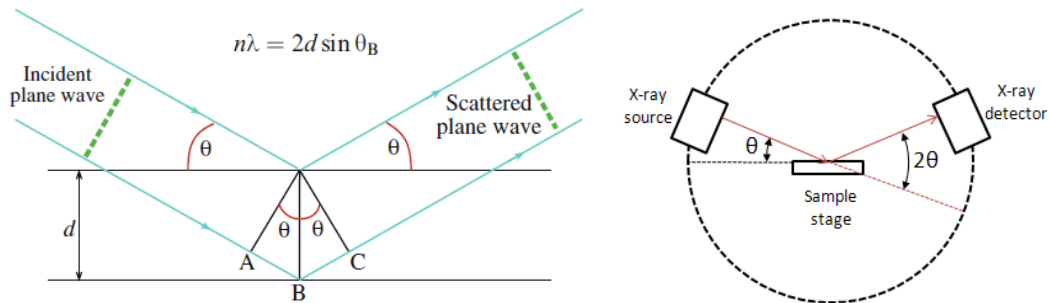
Figure 2.8: X-Ray Diffraction Diagram. An X-Ray source sent X-rays at a sample and all scattered X-rays were collected at all possible diffraction angles, 2Θ, with their respective intensity values. (From Figure 3.9 in Williams and Carter [96] and [118])
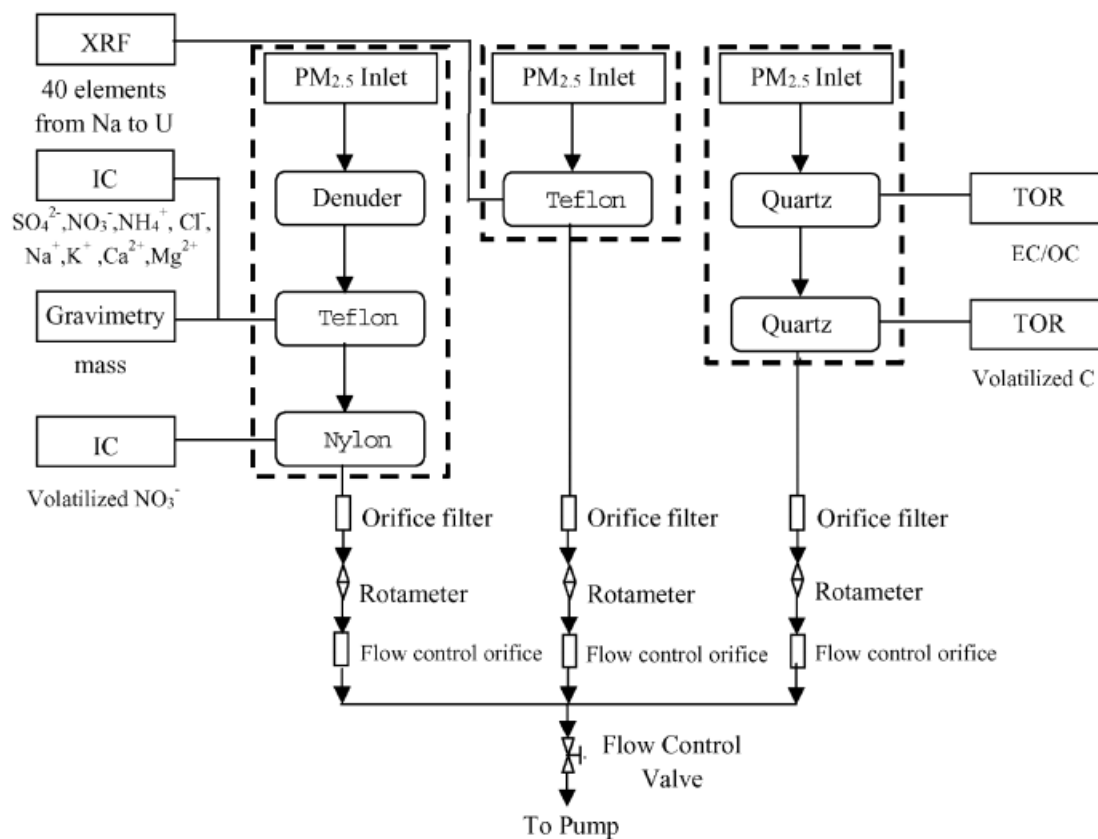
Figure 2.9: Flow Diagram of chemical analysis used for different filters collected for PM$_{2.5}$. (From Figure 2 in [106])

CHAPTER 3: Ambient Particulate Matter

3.1 Background

The San Joaquin Valley (SJV) is a region with air related health risks due to exposure to particulate matter pollution, such as the exacerbation of asthma, lung disease, and cardiovascular disease [3, 24-26]. Winter is when particulate matter (PM) concentrations are highest and when conditions are most suitable for the formation of organic carbon aerosols [119]. In order to determine which constituents of air pollution are most important for mitigation and reduction of air pollution related health risks, two winter samples from two urban cities in the SJV, Merced and Fresno, were analyzed to determine their size, morphology, and chemical composition. Scanning electron microscopy (SEM) and transmission electron microscopy (TEM) was used to analyze the particles extracted off the air pollution filters. SEM and TEM with Energy Dispersive X-Ray (EDX) Spectroscopy was used to determine particle size, shape, and elemental composition. Furthermore, X-Ray Absorption Spectroscopy (XAS) was used to identify the constituents present. This information along with information in the literature was useful for modeling proxy PM, synthesis of proxy PM particles, testing their biological effects, and then learning which parameters were important to mitigate to reduce air pollution related health risks.

In 2008 and 2009, an investigation of particulate matter collected in Wilmington, CA, downwind of an automobile shredding plant, near a harbor, characterized the chemical composition of the emissions with XAS. Although the specific plant studied was not in the SJV, it is typical of similar plants in the SJV and was therefore of interest as a potential source of particulate matter in the industrial sector. An 8 stage Davis Rotating Universal-size-cut Monitoring (DRUM) impactor [120] was used to collect a time series of size-separated particulate samples that were subsequently analyzed by Synchrotron-Induced X-ray Fluorescence (S-XRF) for elemental composition [121]. Here, we report the results from a separate investigation of the different aerodynamic size fractions using Scanning Electron Microscopy (SEM) and Transmission Electron Microscopy (TEM) imaging, and Energy Dispersive X-Ray Spectroscopy (EDXS) for elemental composition; and discuss the implications of these results for the environment and human health.

3.2 Merced and Fresno Ambient Air Particulate Matter

Electron microscopy was used to analyze the Merced and Fresno samples for size distribution, morphology, and chemical composition to determine the parameters for the ideal Proxy PM. When analyzing the air particle filters directly on a carbon tape/aluminum stub, characteristic x-rays of carbon, oxygen, and fluorine were found (Appendix A). Unfortunately, the fluorine signal was high relative to the other signals (about 5x more). Most likely, the filter generated the fluorine signals with the beam electron interaction with Teflon, since in the US, Teflon filters are the most commonly used filters (also the US standard) in mineral dust and heavy metal detection for determination of mass, ions, and elemental composition [122]. In addition, due to particle impaction during sample collection, it was difficult to determine the size distribution of the samples with this sample preparation method.

For Figure 3.1 and 3.2, the sample was prepared by attaching double-sided carbon tape on the filter, and then mechanically peeled to remove the particulates off the filter and onto the carbon tape. In Figures 3.1-3.2, EDX spectra revealed the presence of carbon, oxygen, magnesium, aluminum, silicon, potassium, calcium, titanium, and iron. The carbon signal was from the carbon tape and some of the aluminum signal was from the aluminum stub used to mount the sample (a background check on the carbon tape showed carbon signal and some aluminum signal). The presence of aluminum, silicon, and oxygen indicated the presence of aluminosilicates. Although, most of the carbon signal was from the carbon tape, additional sources of carbon could have been from tire dust (styrene and butadiene) and auto exhaust, while the magnesium, potassium, calcium, titanium, and iron most likely came from soil dusts. Iron and chloride could originate from auto exhaust as well [123]. From this information, silicate dust particles with iron would be a good candidate for a proxy PM particle.

Table 3.1 shows the size distribution for Fresno and Merced particles. The size distributions for the Merced and Fresno samples were 1.56 ± 0.60 µm and 1.65 ± 0.72 µm, respectively. The particles sizes were similar to each other. However, the size range for Merced and Fresno samples were 0.43 to 4.14 µm and 0.32 to 7.39 µm, respectively. The wide range of sizes could have been due to aggregation during sample collection, since the air particles can be impacted as they are collected on the filter [124]. On the other hand, the SEM also limited the detection for smaller particles. Therefore, the samples were also prepared for TEM analysis to observe particles less than 100 nm.

For Figure 3.3 (A-F), sample preparation involved using an ethanol drop on the air filter, placing a TEM grid on top of the drop, air drying the ethanol, and then peeling the particles off the filter with the TEM grid. Based on these TEM images, particles seen in the SEM were aggregates of nanoparticles, mostly ranging from 40 to 100 nm. For the samples shown in Figure 3.3 (G-L), sample preparation involved water instead of ethanol. The elemental composition for the samples in TEM matched the results for EDX from SEM. All samples contained carbon, silicon, oxygen, aluminum, and iron. The size distribution using the water extraction method made it difficult to determine the size of the nanoparticles, since these particles appeared to be sheets of aggregated nanoparticles. Furthermore, the water drop method may have removed the salts and organic carbon from the particles, giving the appearance shown in Figure 3.3 (G-L). As for the ethanol extraction method, the size distribution for the Merced samples was 43.0 ± 15.6 nm with a range of 12.6 to 124.2 nm. Similarly, the Fresno sample size distribution was 40.0 ± 12.9 nm with a range of 16.1 to 93.6 nm. These sizes support the use of ~50 nm particles for making the proxy PM for testing biological effects.

Chemical analysis determined the average percent compositions for the chemical constituents in $PM_{2.5}$ in the SJV (Figure 3.4A) and the variability of chemical composition over time in 2011 (Figure 3.4B). $PM_{2.5}$ contained organic carbon, nitrates, sulfates, ammonium, potassium, sea salts, elemental carbon, organic carbon, metals, and geological mass. The main constituents were organic carbon, nitrates, sulfates, and ammonium as measured by chemical analytical techniques (See Figure 2.9 in Chapter 2). The water drop method was used to wash off some of these constituents during TEM preparation, since EDX spectra only show silicon and oxygen signals (Appendix A) compared to the EDX spectra with the ethanol drop method (Figure 3.3 A-F).

Furthermore, this suggested that different organics and salts coated the surfaces of PM. Also in Figure 3.4B, there are geological and metal constituents on the $PM_{2.5}$ particles, which support the present of aluminosilicates and iron as detected by EDX (Figure 3.1 and 3.2). Elemental carbon may be sourced from soot, and organic carbon could be sourced from biomass burning, wood burning, and vehicular emissions [73]. Polycyclic aromatic hydrocarbons (PAHs), known carcinogens, may also be part of the organic carbon fraction, since it can be produced from diesel exhaust and biomass burning as well [73]. From this information, organic carbon can also be used on the proxy PM particles to mimic PAHs on natural PM.

The Merced and Fresno samples were very similar to each other. EDX for the TEM (Figure 3.5A) showed a similar chemical composition from SEM. The copper and some carbon signals were background signal from the holey carbon – copper TEM grid. Similar to SEM, the nanoparticles observed in TEM contained aluminum, silicon, oxygen, and iron. This implied the presence of aluminosilicates with trace iron, commonly found in road dusts and produced from agricultural processes [68-70]. Morphologically, they appeared aggregated and similarly spherical [125]. In addition, the TEM images did not show any signs of diffraction. This indicated that either crystalline silica was not present, or its concentration was too low to detect.

In Figure 3.5B, bulk iron X-ray Absorption Spectrum (XAS) at the Fe K-edge of a SJV particulate sample (< 2 μm) (blue line) fitted with a combination of two reference spectra, 2-line ferrihydrite (Fe^{3+} (OH)$_3$) and a smectite clay, an aluminosilicate, (SAz-1) with 1.42% Fe (III) and 0.08% Fe (II). Ferrihydrite synthesized in the lab and the SAz-1 sample from Clay Minerals Society Source Clays Repository acted as standard references for this experiment. This shows the main components as aluminosilicate dust and ferrihydrite. Iron coated on silica can mimic the ferrihydrite coated aluminosilicate dust as proxy PM model of natural PM in an urban setting.

3.3 Automobile Shredding Plant - Terminal Island

Electron microscopy was also used to analyze samples from an automobile shredding plant for size distribution and elemental composition. Table 3.2 presents the nominal aerodynamic and actual particle sizes as determined by SEM for each of the eight stages collected by the DRUM impactor. Note that aerodynamic particle size was a function of the true size of the particle, shape factor, and density, while smaller particles may be difficult to be resolved in the SEM. Therefore, differences between the two numbers were expected.

In general, the mean size of the particles as observed in the SEM falls within or close to the expected aerodynamic particle size range for Stages 1-4. For Stages 5 and 6, average particle size as observed in the SEM was much larger than the expected aerodynamic particle size and this may have been due to the shape factor of particles in those samples. For Stages 7 and 8, the average particle size as observed in the SEM was somewhat larger than the expected aerodynamic particle size, which may be due to the inability to resolve smaller particles due to limitations in resolution for the tungsten-equipped SEM used.

Nearly all of the particles collected by the DRUM impactor were less than 10 microns in size (except for Stage 5), and much of it was less than 2.5 microns in size, as

measured by SEM. Particulate matter (PM) larger than 10 microns was usually not of concern because the cilia and mucus in the lungs prevent it from penetrating deep into the lungs [126]. However, PM_{10} (PM less than 10 microns in diameter) can enter and deposit deep inside the lungs, as far as the bronchioles and alveoli. $PM_{2.5}$ (PM less than 2.5 microns in diameter) could travel even further, into the gas exchange region in the alveoli. Therefore, most all of the particles collected here have the potential to enter the lungs and cause lung damage. Aggregation of particles in the lungs may cause lung obstruction and other related diseases, and any transition metals that are present can cause oxidative stress, leading to inflammation and respiratory disease.

Figure 3.6 shows SE SEM Images for Stages 1-8, representative of the particle size data shown in Table 3.2. The earlier stages were the most heavily loaded with particles. SEM imaging showed that the largest sized sample, Stage 1, contained large faceted particles of soil particulates and salts, as well as diatoms, consistent with the ocean side location of the tire shredding plant. Beginning in Stage 2, spherical particles, indicative that they had their origins at elevated temperature, ~ 2 µm in diameter, started to become visible. These particles were also readily visible in Stages 3-7 of the collected particulate matter. In Stages 2-4, needle-shaped particles were visible. Stage 5 had rosetta shaped particles, and Stages 6 and 7 showed highly faceted particles. Particulate matter of indistinct shape was seen Stage 8. A view of all the stages at different magnifications are shown in Appendix B.

In Figures 3.7 and 3.8, the EDX spectra show the chemical compositions for Stages 1-4 and 5-8 respectively. Stages 1-4 showed C, O, Fe, Na, Mg, Al, Si, S, Cl, K, Ca, and Fe. Elemental mapping (Appendix C) appeared to correlate carbon mainly to the support film for the particles, as it mapped to locations where visible particle loading was low or nonexistent. Oxygen, iron, magnesium, aluminum, silicon, potassium, calcium and silicon were all typical elements in soil particulate matter and were found throughout the sample [41]. Iron was also present in the form of spherical particles ~ 2 µm in diameter. The shape suggested they had their origins at elevated temperatures and the appearance of this fine particulate matter correlated with when the plant was operating, and when wind directions were favorable for transport of particles from the plant to the sampling location. Thus, they were a "tracer" particle for plant emissions. Sulfur maps with oxygen, suggested the presence of sulfate, and this composition was correlated to the needle, rosetta, and faceted particles that form a large fraction of the samples. Sulfur was likely highly represented throughout due to emissions from passing ships that use high sulfur bunker oil as a fuel source [127]. Seawater contains sodium, chlorine, potassium, and calcium as salt crystals. For Stages 5-8, samples contained C, O, Al, and S. Carbon and aluminum were likely from the sample support film and SEM stub. This indicated the primary phase detectable for small particles by EDXS was sulfate.

Spot EDXS analysis in the SEM also revealed the presence of barium, cerium, and lead (Figure 3.9). In catalytic converters and diesel particulate filters, cerium is used in the catalysis support material, and barium oxide is used in particle traps and absorbers [128]. In Figure 3.9A, the EDXS spectrum primarily contained barium, oxygen, and sulfur, indicating a high probability for the presence of barium sulfate. In catalytic converters, the catalyst could degrade when interacting with sulfur dioxide, forming barium, cerium, and potassium sulfates [129]. In Figure 3.9B, cerium and oxygen were

the main components indicating parts of the catalyst that did not deactivate to cerium sulfate. Their presence in the end of life cycle for cars is expected. In Figure 3.9C, iron and oxygen were the main components in the EDXS spectrum indicating the presence of iron oxide. The spherical shape is indicative of a high temperature process. In Figure 3.9D, EDX detected lead, possibly from lead batteries. Before shredding, batteries, oil, fuel and other recyclable components are usually, but not always, removed from the vehicles [130]. Detection of lead correlated with operations of the plant and a separate XAS study revealed deposition of lead on surfaces near the sampling site exceeded acceptable standards.

TEM EDXS analysis is shown in Figure 3.10 and reveals the presence of zinc, nickel, chromimum, and vanadium. The non-ferrous metal in cars contain zinc, and the automobile shredding plants generally separated these metals during operation [131, 132]. Soil and steel alloys contain chromium. The nearby shipping traffic produced nickel and vanadium from combustion of bunker oil [127, 133].

3.4 Parameters for Proxy Particulate Matter Particles

The chemical composition of the natural PM contained aluminum, silicon, oxygen, and iron, and the XAS confirmed the presence of aluminosilicates and ferrihydrite in the SJV samples. Using these parameters for the proxy PM particle, the proxy PM should be composed of an aluminosilicate and ferrihydrite. However, in the literature, there are limited syntheses for aluminosilicate nanoparticles [134] with size control. Alternative materials for aluminosilicates are silica (silicon dioxide) and alumina (aluminum oxide). Alumina is a low hazard material and may not induce any biological effects [135], while silica has been studied previously [82]. In addition, silica is water soluble [136], while alumina is not. Therefore, in relation to air pollution, even if inhaled, alumina will be less likely to enter the blood stream compared to silica nanoparticles. Therefore, silica is a better choice to use as a proxy PM particle. However, when synthesis protocols for aluminosilicates are more developed, then the proxy PM particles can be made of these nanoparticles for future studies.

Other important parameters are size, surface area, and total iron concentration. Based on the analyzed data and images, the nanoparticles formed micrometer-sized aggregates for the Merced, Fresno, and automobile shredder plant samples. Studies indicate that the nanoparticle fraction may play a big role in PM toxicity [10, 54, 55]. Here, the focus will be on the nanoparticle fraction of PM, so the proxy PM particles will also be 40-50 nm. Unfortunately, there was not enough mass of natural PM samples on the collected air pollution filters for surface area measurements with BET and total iron with ICP-MS. This would require more air filters, which is not feasible. If the created proxy PM size is the same as the natural PM, then their external surface areas can be comparable. When using water for TEM preparation, the natural PM looked more porous compared to the ethanol extraction method (Figure 3.3). If the natural PM is actually porous, then mesoporous silica can be a porous proxy PM. In addition, since the exact amount of ferrihydrite is unknown, different concentrations of ferrihydrite would need to be tested for the proxy PM particles and confirmed for the presence of ferrihydrite instead. In future experiments, other metals, such as lead, zinc, and chromium, found in the automobile shredding plant study, can substitute for iron.

Based on the analysis of PM$_{2.5}$ in the SJV, elemental carbon and organic carbon are also a major component of PM (Figure 3.4). To represent the carbon portion of PM, a carbon-based nanoparticle can represent soot. The core can be elemental carbon and coated with organic carbon. PAHs are formed in the combustion of soot and are of concern for health risks because of their known carcinogenic and mutagenic effects with soot [137]. Specifically, 1, 4-Naphthoquinone, a representative of quinones derived from diesel combustion [88], can be used to coat the carbon-based proxy PM. Both iron and PAHs can produce reactive oxygen species [138], so both silica and carbon proxy PM particles can be coated with an iron oxide as ferrihydrite and with quinone as PAHs. The proxy PM particles can used in biological tests for health effects and compared to the natural PM. This can be an initial proxy model and modified in the future. In addition, the natural PM can also be analyzed for its concentration of PAHs with gas chromatography [137] and then the major PAHs can be added to the proxy PM instead.

3.5 Sample Collection for Representative samples

Unfortunately, there was not a sufficient amount available from the air filters for bulk characterization tests or biological tests. If sample collection via the filters continues, more filters need to be collected to get the minimum mass required for surface area, total iron concentration, and biological tests. In addition, as shown by the TEM images for the Merced and Fresno samples in Figure 3.3, different extraction methods also provided different morphologies of the natural PM. It is important to retain the properties of the PM for biological testing. A water collection system can collect PM to keep the properties of PM intact. This would allow enough samples for characterization and speciation, and make them readily available for biological experiments that are generally water based (cell media). This may work as long as the PM does not undergo other reactions in the water, such as hydrolysis, although this may already occur with current filters. For instance, ferrihydrite can convert into goethite or hematite depending on the temperature and pH of the solution it's in over time [139]. Therefore, biological tests need to be done quickly and efficiently, before the samples lose their natural PM properties.

In the future, more samples from different regions of the SJV can improve the proxy PM model by determining new parameters to test in biological experiments. Since the composition of PM can also vary (as shown in Figure 3.4B) over time, samples from different times of the year can also be analyzed. This may allow different time and regional mitigation strategies to best reduce health risks of air pollution and improve human health. As shown in the automobile shredding plant study, the location information for the plant helped in identification of potential air pollution sources, such as the diatoms due to the nearby harbor [121]. The samples from Merced and Fresno were from an urban setting. To improve on source identification, representative sampling locations of near sources of mitigation may be of interest. For instance, samples from collection sites near a major highway may provide a sample for a better proxy PM for vehicular pollution with PAHs. The SJV has descriptions of their monitoring locations and these can be used for monitoring specific locations [140]. Additional monitoring stations or DRUM collectors can test new locations for specific sources.

3.6 Conclusions

Based on the analysis of the Merced and Fresno samples, the proxy PM particles should be silica-based and iron and roughly 40 nm in diameter. Iron hydroxide and quinones (to represent PAHs or organic carbon) can represent the surface coated constituent on the surface of the Merced and Fresno particulate matter samples analyzed. Furthermore, since the TEM did not detect crystalline silica for the Merced and Fresno samples, then synthesis protocols for non-crystalline silica dioxide nanoparticles can represent the silica particulate matter. Based on the speciation data from SJVAPCD, the main constituents in $PM_{2.5}$ are organic carbon, nitrates, and ammonium. Since water removed these constituents, the proxy PM should contain the constituents that persist, such as the aluminosilicate (geological), iron (metal) and soot (elemental carbon). A model of carbon may also work as a proxy PM particle. Organic carbon and metals (i.e. iron) coated on the silica and carbon models can mimic the natural particles as well.

For the automobile Shredder study, results for larger particles (aerodynamic particle size of 2.5 to 10.0 μm) showed aluminosilicates, consistent with dust particles from geological sources. This was consistent with the SJV studies. In addition, detected iron in the form of spherical particles was ~ 2 μm in diameter, indicating origins from a high temperature process attributable to shredding operations. The shredding plant also produced small amounts of lead, cerium, barium, chromium, and zinc. The respirable particle sizes and presence of transition metals attributable to shredding operations was a concern for inflammatory lung disease while the presence of lead was a concern due to its overall toxicity. From both studies, a proxy PM of silica and carbon with iron and quinones would be a simple model to study to determine potential health effects. In future work, other components can be added, that were not examined in this current work, and samples from other representative sampling locations can be analyzed to modify the proxy PM particles.

3.7 Figures and Figure Legends

	SEM		TEM	
	Merced	Fresno	Merced	Fresno
Count	800	800	400	400
Mean	1.56 μm	1.65 μm	43.0 nm	40.0 nm
Minimum	0.43 μm	0.32 μm	12.6 nm	16.1 nm
Max	4.14 μm	7.39 μm	124.2 nm	93.6 nm
Std. Deviation	0.60 μm	0.72 μm	15.6 nm	12.9 nm

Table 3.1: Size distributions of Fresno and Merced Samples using SEM and TEM.
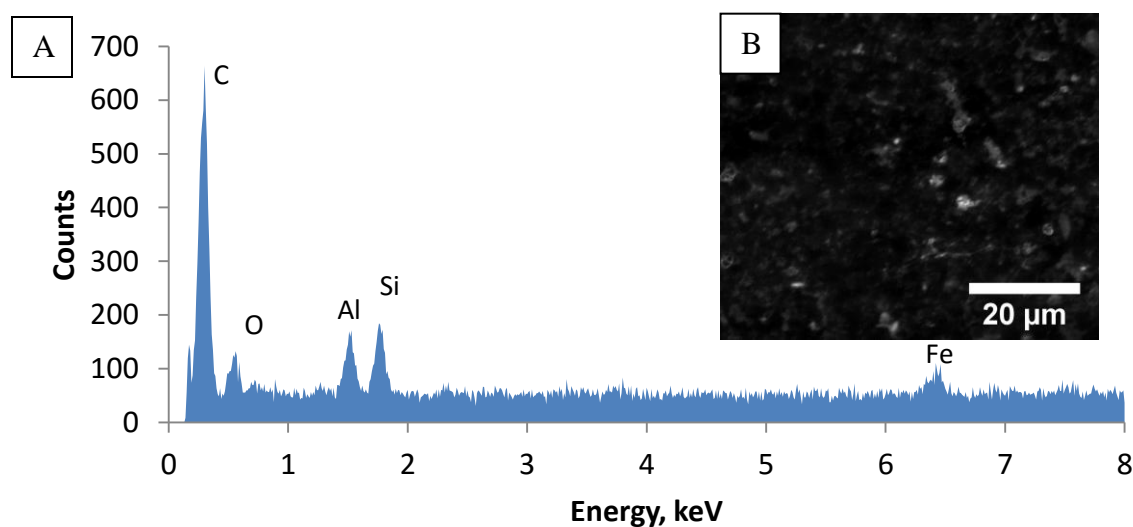
Figure 3.1: Elemental Composition of Merced Air Particle in SEM using EDX. (A) EDX spectrum (B) Inset SEM image.
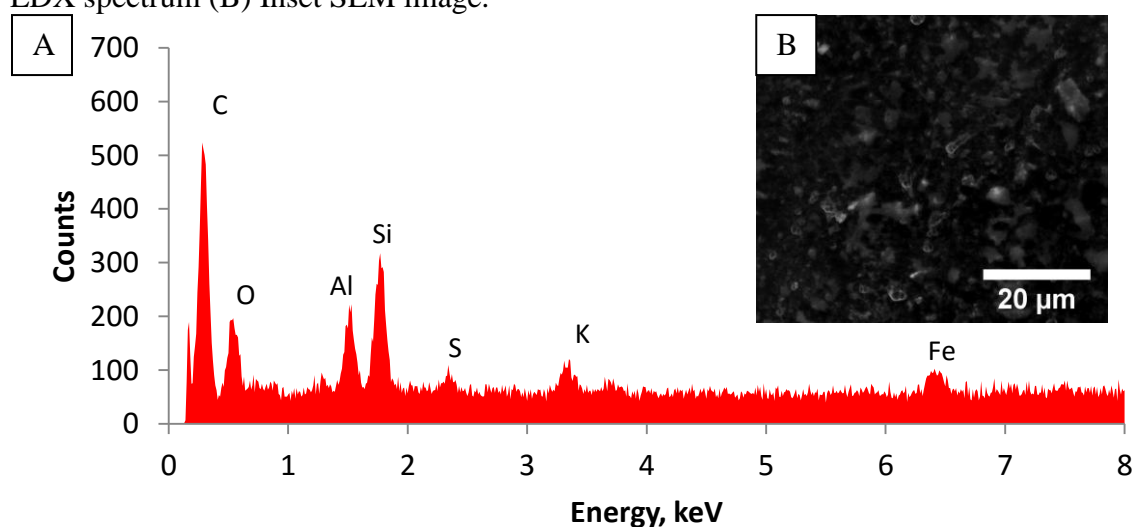
Figure 3.2: Elemental Composition of Fresno Air particles in SEM using EDX. (A) EDX spectrum (B) Inset SEM image.
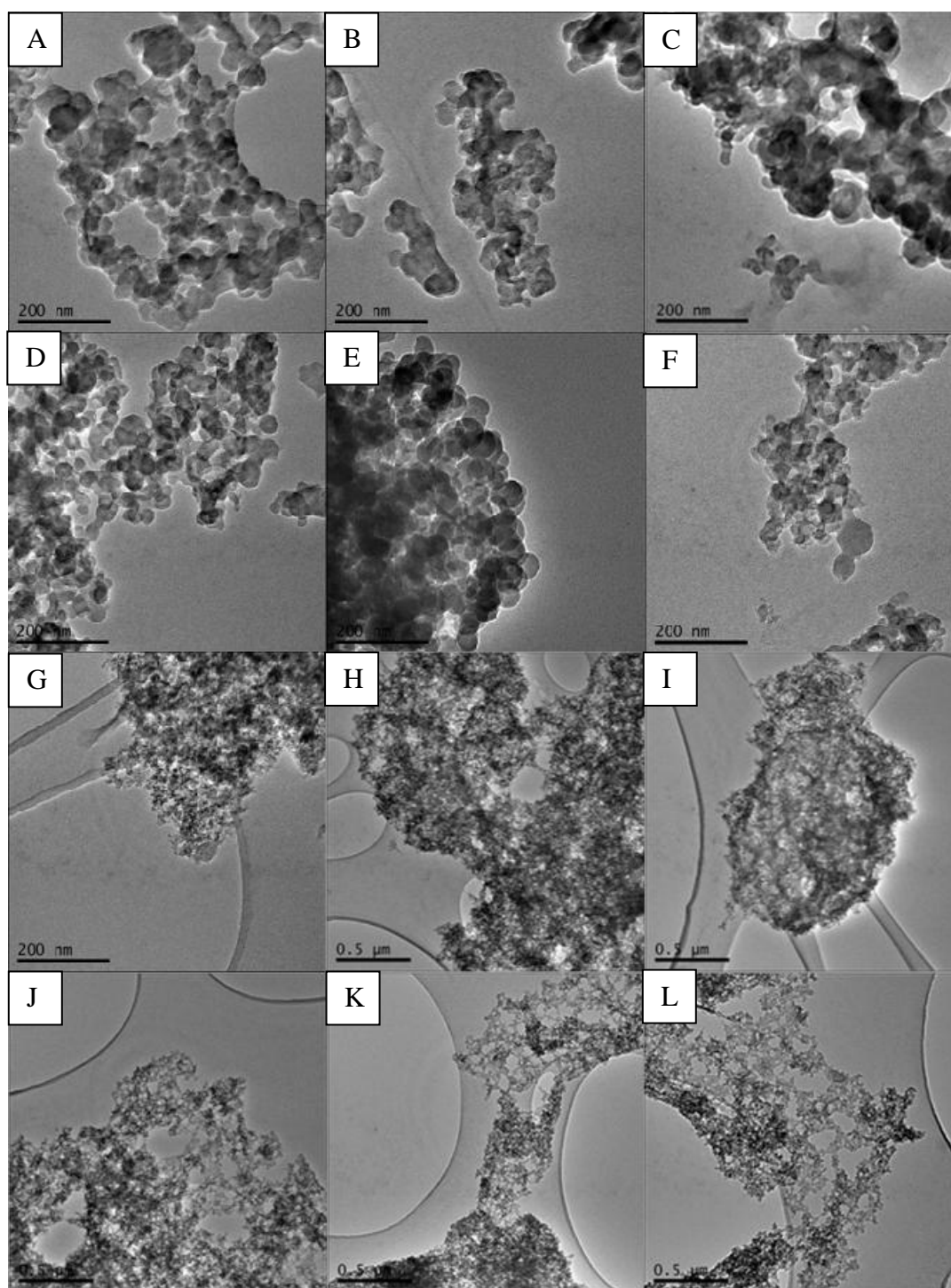
Figure 3.3: TEM micrographs for ethanol drop preparation for Merced (A-C) and Fresno (D-F) samples and water drop for Merced (G-I) and Fresno (J-K) samples.
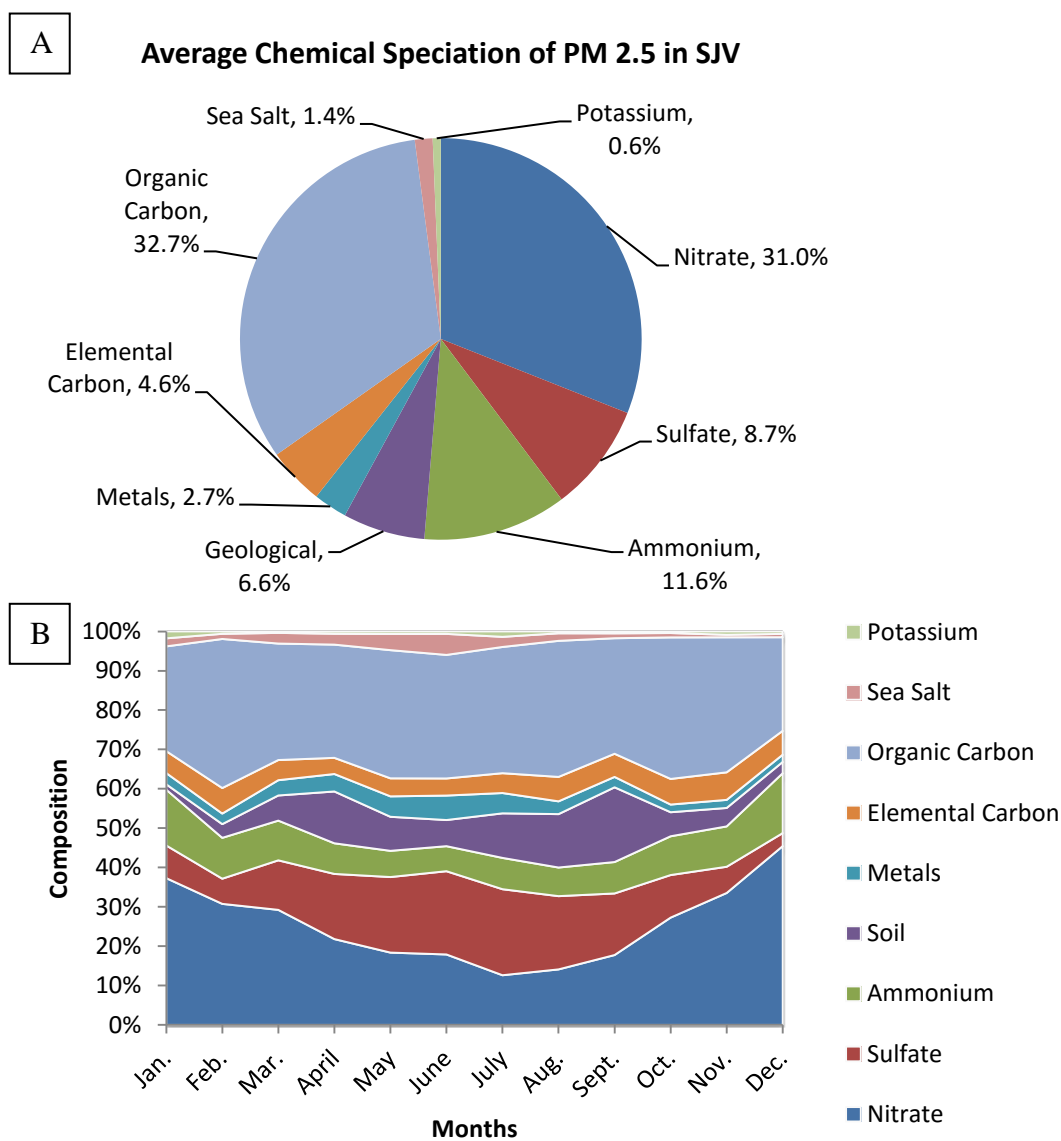
Figure 3.4: Chemical speciation of PM$_{2.5}$ in SJV particulates (A) Average Percent Composition (Averaged 2000 to 2013 SJV data) and (B) Variation of Percent Composition over time (Data from Fresno 2011). Data from SJVAPCD.
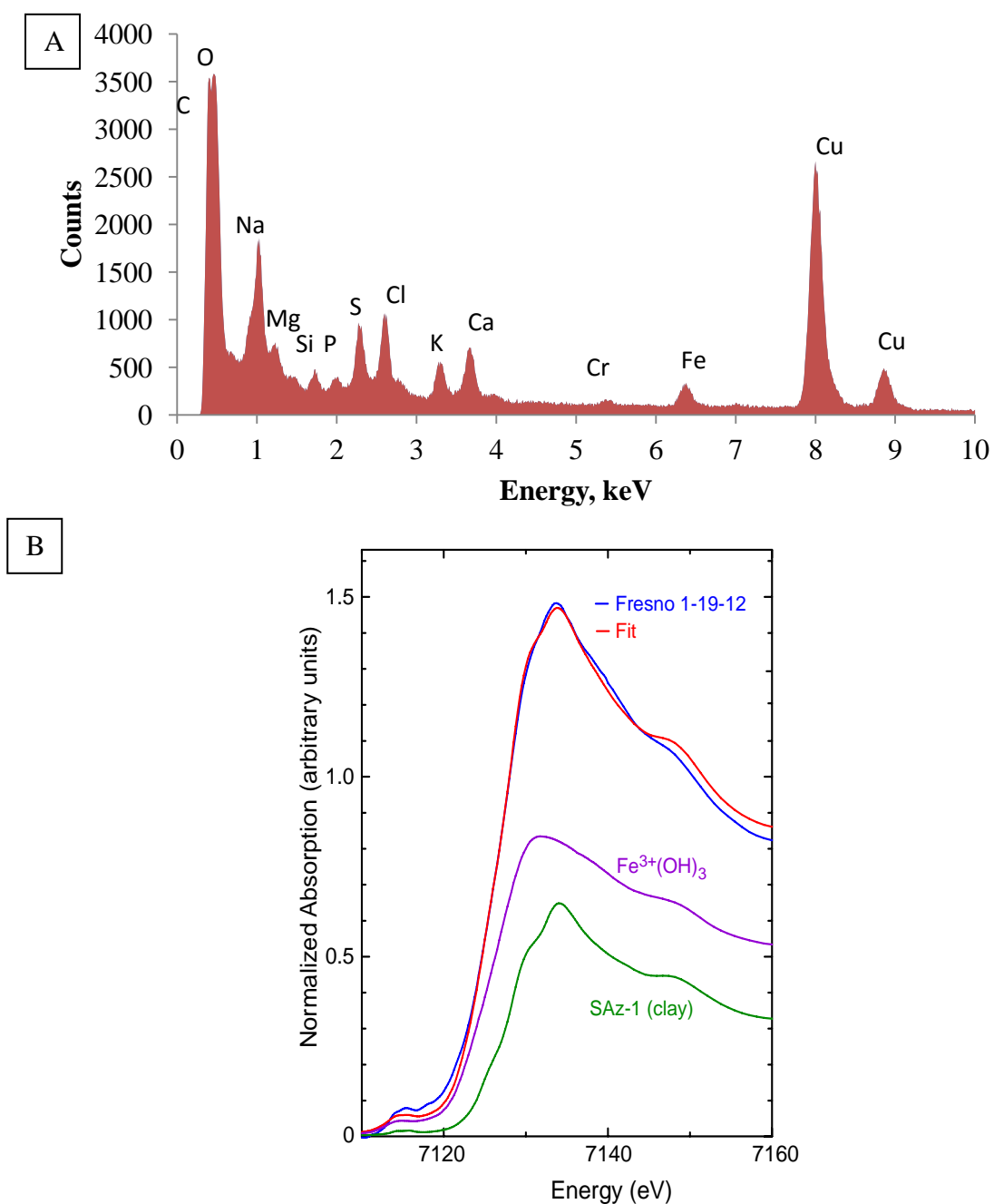
Figure 3.5: Representative (A) EDX and (B) Bulk X-Ray Absorption Spectra of Merced and Fresno samples. (XAS data analyzed by Peggy O'Day lab at UC Merced).

	Size Fraction (µm)	Average (µm)	Max (µm)	Min (µm)
Stage 1	10.0 - 5.0	5.02 ± 4.21	60.64	1.04
Stage 2	5.0 - 2.5	3.72 ± 3.16	25.13	0.79
Stage 3	2.5 - 1.15	2.8 ± 2.33	31.88	0.96
Stage 4	1.15 - 0.75	2.34 ± 1.98	20.36	0.27
Stage 5	0.75 - 0.56	30.57 ± 14.8	80.7	9.27
Stage 6	0.56 - 0.34	11.46 ± 5.7	42.85	2.67
Stage 7	0.34 - 0.26	2.34 ± 0.71	5.74	0.84
Stage 8	0.26 - 0.09	0.48 ± 0.13	1.68	0.19

Table 3.2: Size distribution of Particles based on SEM imaging (N=500)
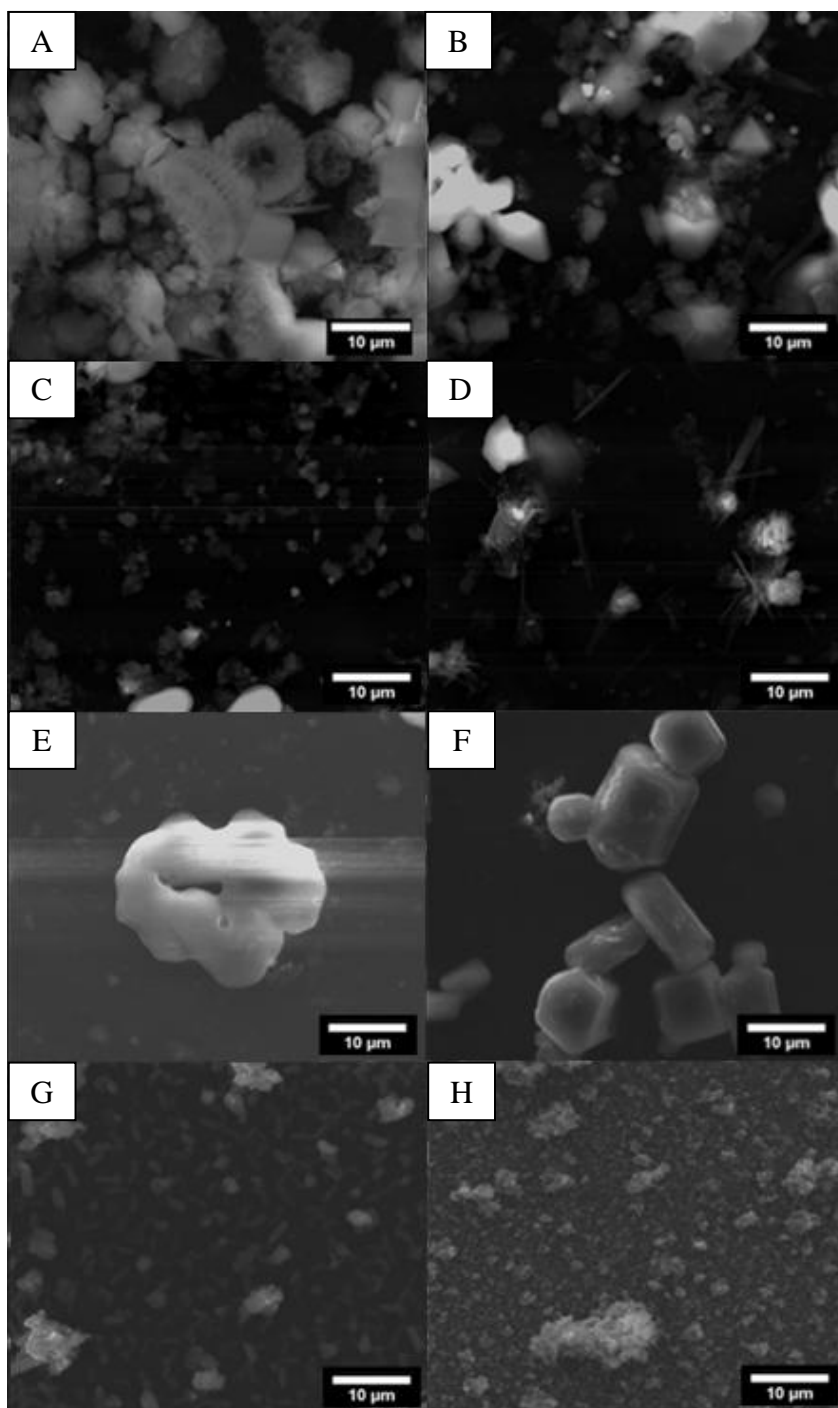
Figure 3.6: SEM Images of DRUM Impactor for (A) Stage 1, (B) Stage 2, (C) Stage 3, (D) Stage 4, (E) Stage 5, (F) Stage 6, (G) Stage 7, and (H) Stage 8.
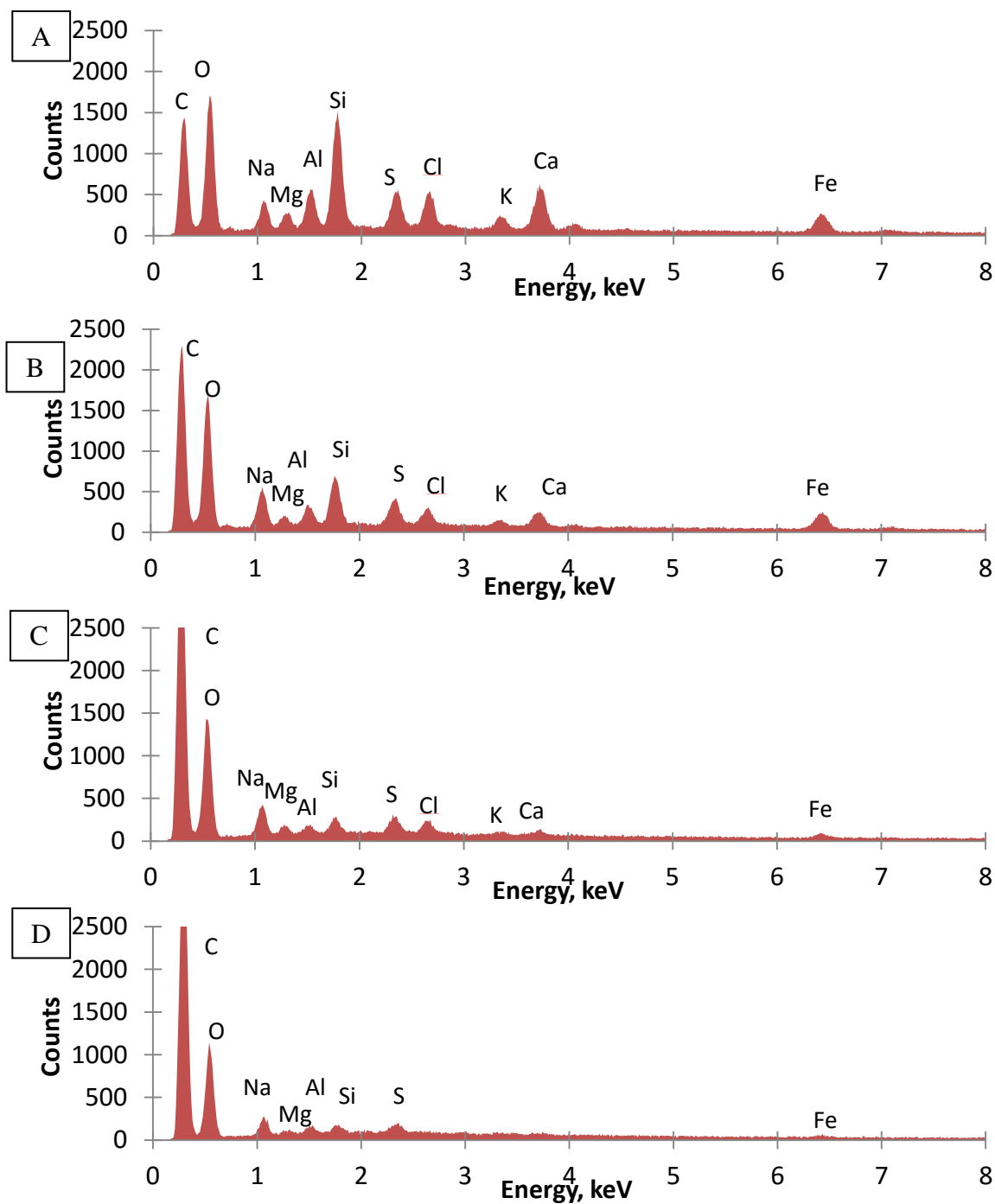
Figure 3.7: EDXS of: (A) Stage 1, (B) Stage 2, (C) Stage 3, and (D) Stage 4.
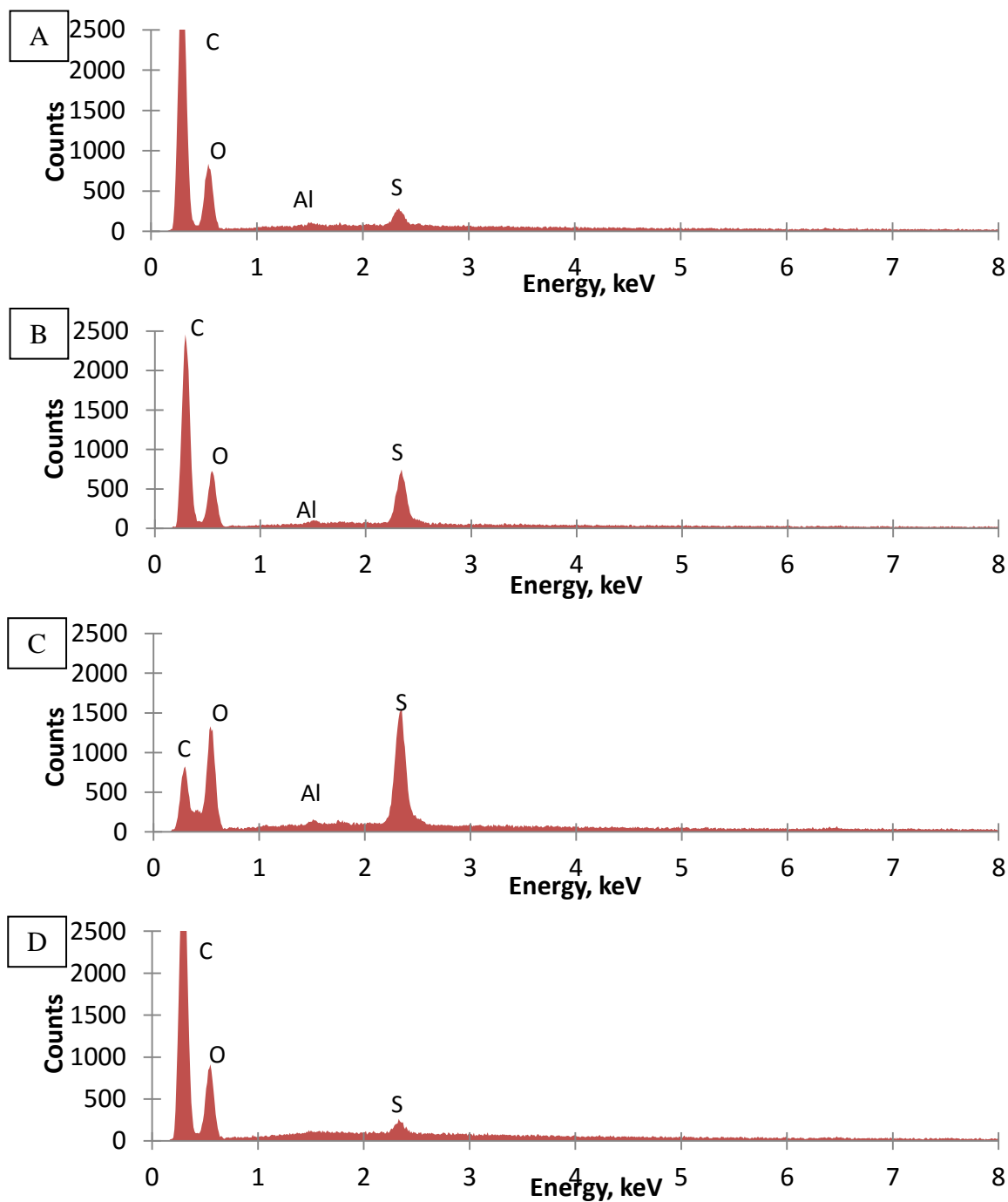
Figure 3.8: EDXS of: (A) Stage 5, (B) Stage 6, (C) Stage 7, and (D) Stage 8.
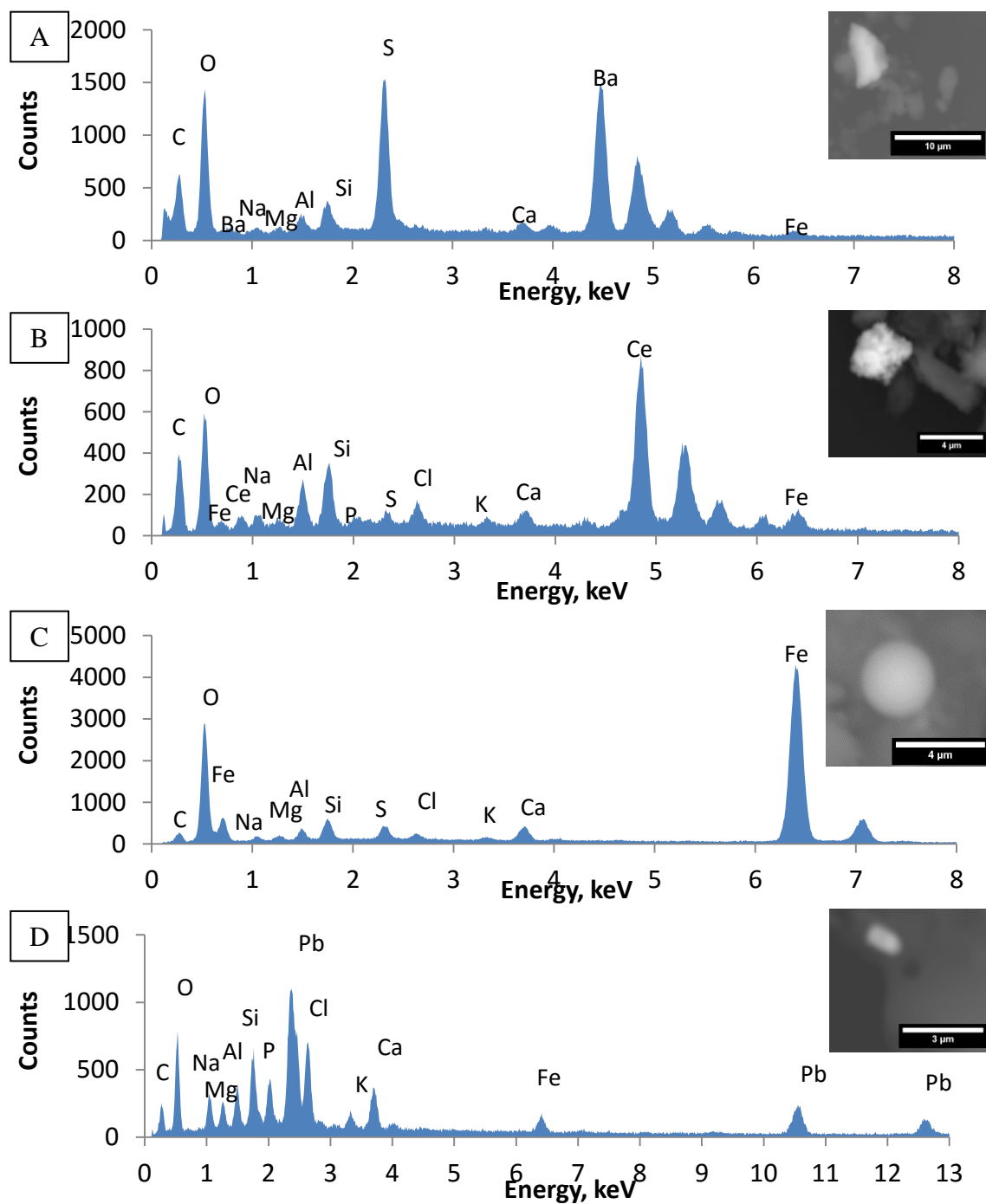
Figure 3.9: EDX spectra of various particles: (A) Barium, (B) cerium, (C) iron, and (D) lead found in samples. Inset is a Backscattered electron image.
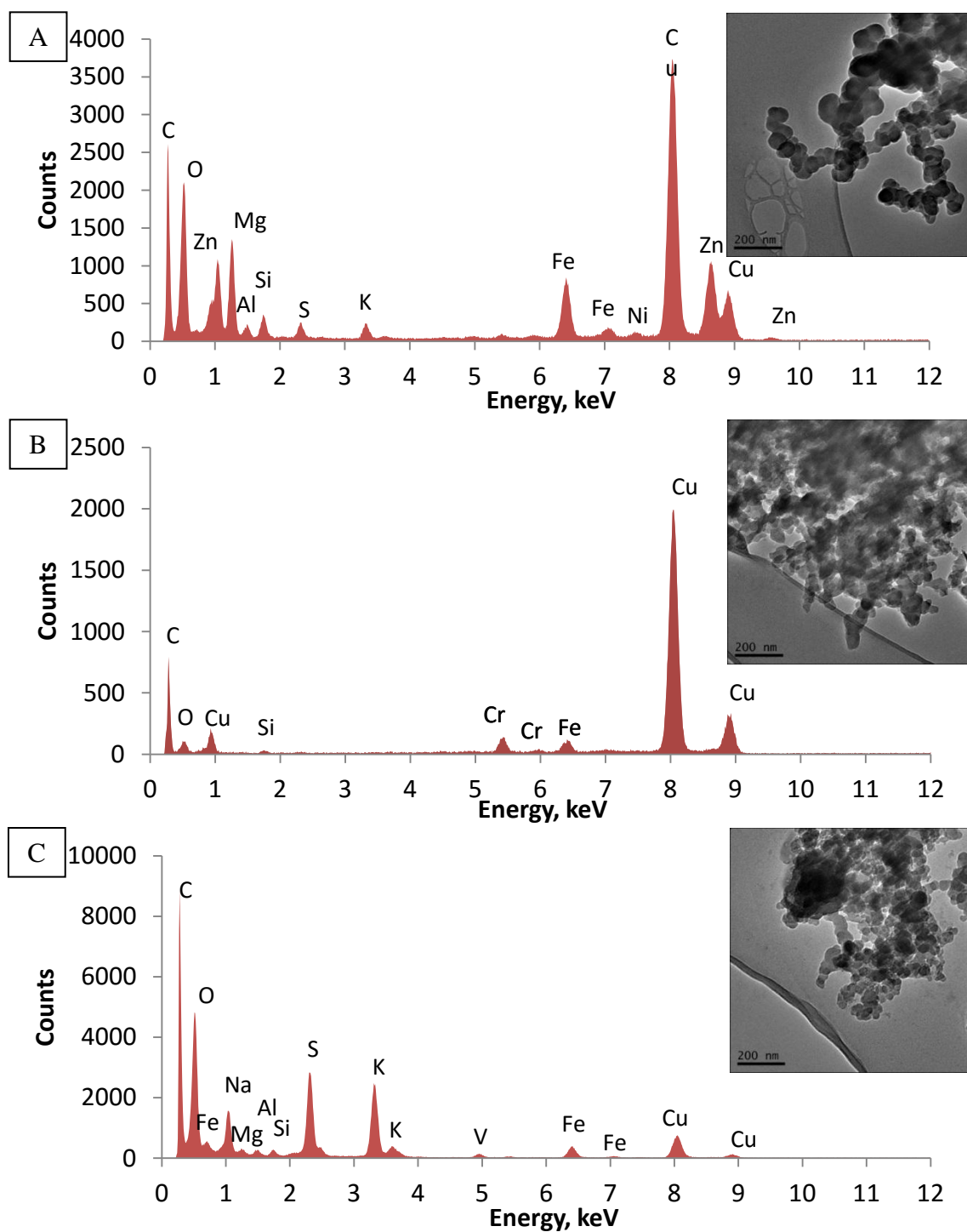
Figure 3.10: EDXS with images showing various elements found while using TEM. Inset is bright field TEM image. (A) Zinc and Nickel, (B) Chromimum, and (C) Vanadium containing particles.

CHAPTER 4: Silica as Proxy Particulate Matter
4.1 Background

Silica can be an ideal proxy particulate matter model for aluminosilicate dust that is common in air pollution. Silica particulate matter can originate from natural sources, industrial processing, and agriculture activities. Silica found in the environment is generally crystalline, with quartz being the most common form [93]. The silica composition of the particulate matter in an urban setting is between 1.6 - 10.4%, with 87% of the silica composition less than 2.5 μm in diameter [141]. Per volume, the concentrations range from 0.2 to 10 μg/m^3 under non-occupational settings [141, 142]. In the United States, occupational exposure to silica, such as from silica milling, mining, and sandblasting, is estimated to be over a million people annually [143]. Several different non-crystalline forms of silica are also manufactured, such as fumed silica, silica gel, and fused silica, for the production of paints, cosmetics, and fillers [144, 145]. In addition, porous silica particles, called mesoporous silica have potential applications in catalysis, separation, sensing, and wastewater treatment [146, 147]. Exposure to silica can promote free radicals production, resulting in oxidative stress and inflammation [148], which may result in diseases after long term exposure, such as silicosis, and has been linked to the development of scleroderma, rheumatoid arthritis, chronic renal disease, and lung cancer [149, 150].

Silica nanoparticles can be synthesized for model natural PM. Unfortunately, several studies in the literature do not provide the rationale for the size of the silica particles studied [151-153]. This is mainly due to the availability of these particles from vendors and limited size control for synthesis [154]. With the known size distribution of particulate matter (PM), synthesized silica can model these PM particles, using modified synthesis methods in the literature [91, 155, 156]. From our previous studies on natural particulate matter (PM) in the SJV, the average particle size ranges from 40 to 50 nm. The silica particles can undergo further modification to match natural PM to test the parameters that effect human health, such as crystallinity and presence of ferrihydrite.

In our previous work, we used crystalline silica particles as a model air particle pollutant to study a novel mechanism of iron-mediated silica-induced pro-inflammatory response at realistic doses for natural ambient crystalline micron-sized (2 μm) silica particles [82]. Our mechanism involved silica interaction with a macrophage receptor that activated NADPH oxidase on the cell membrane (Figure 1.3 in Chapter 1). Then, we worked with non-crystalline silica for size control (2 μm and 50nm). The results indicated that size, phase, and the presence of transition metals played a role in the inflammatory potential of the particles when it interacted with the cells. At a high dose, particle apoptosis may occur and subsequent particle uptake of the apoptotic cells can inhibit pro-inflammatory responses in macrophages [157, 158]. A low non-cytotoxic dose was needed to observe mainly pro-inflammation and these results matched closer to realistic exposure scenarios [159]. To expand on this work, we focused more on the chemical speciation of the silica particles and its iron coating to match natural particulate matter (PM). Chemical and physical characterization of iron coated silica particles determined the properties that effect health for silica exposure with iron. Iron is the most common active reduction-oxidation metal on PM [160]. Here, newly synthesized silica particles (S-Silica) with iron coatings and older silica samples (C-Silica) tested the effect

of sample preparation for biological effects. There was also an attempt to make crystalline silica particles from the lab-synthesized particles.

In addition, mesoporous silica particles from a commercial source and lab synthesized mesoporous silica MCM-41 were used to test for cell toxicity. Different material properties of mesoporous silica affected toxicity such as particle size and size distribution, shape, agglomeration, crystal structure, chemical composition, surface chemistry and charge, and porosity [92, 153, 161-165]. Here, we will also look at the toxicity of mesoporous silica compared to solid, non-porous silica of similar size. In addition, plain silica, iron coated silica, quinone coated silica, and iron and quinone coated silica were tested for cell viability on THP-1 monocyte-derived macrophages to determine the effect of different surface coatings on the proxy PM particles. Iron is a common metal contaminate and also present in soil [166], while quinones can act as an oxidized polycyclic aromatic hydrocarbon (PAHs), an organic carbon compound found in diesel exhaust [88, 167]. Both iron and quinones are representative reactive species on the surface of ultrafine PM [168-175] and should help the proxy PM mimic natural PM.

4.2 Silica Characterization
4.2.1 Commercial Silica (C-Silica) versus Lab Synthesized Silica (S-Silica)

This study characterized and compared the 50 nm commercial silica (C-Silica) from Microspheres and Nanospheres and lab synthesized silica (S-Silica) particles. The silica size distributions of silica were 41.7 ± 5.9 nm (C-Silica) and 42.7 ± 6.3 nm (S-Silica). The C-Silica has a BET surface area of 54.5 m^2/g; and S-Silica has a BET surface area of 53.1 m^2/g (Table 4.1). Both samples had nearly the same size distribution, morphology, and surface area. In Figure 4.1 and Figure 4.2, the uncoated C-Silica and S-Silica were relatively pure, and there was no detectable presence of iron (Iron EELS signal usually around 710 eV) based on their EELS spectrum. Visually, the surface of the particles also appeared clean and void of other material in both the STEM and TEM images. The surface iron concentration was relatively low on the uncoated silica particles as detected by ICP-MS: 0.06 ± 0.07 mmol/g and 0.13 ± 0.08 mmol/g. The C-Silica and S-Silica were essentially the identical particles.

4.2.2 Iron Coated C-Silica and S-Silica

Both C-Silica and S-Silica were also coated with iron by a method from Ghio [92]. From Table 4.1, the size distribution of Iron Coated C-Silica (Fe C-Silica) and Iron Coated S-Silica (Fe S-Silica) were 40.6 ± 6.2 and 43.8 ± 6.3 respectively. In Figure 4.3, images of different regions of the Fe C-Silica show its size distribution on the TEM grid. The nanoparticles had crystalline (based on the presence of an electron diffraction pattern) shards present. These may be spindles formed since an Fe(III) solution was used to coat the silica particles [176], however these could have also been formed from vacuum drying of the sample. The Iron Coated C-Silica was also an older sample, which may have aged. Electron diffraction of the crystalline shards revealed d-spacings of 0.431, 0.333, and 0.227 nm. These d-spacings matched well with iron oxide hydroxide (FeOOH) of 0.4446, 0.3301, and 0.2213 nm (JCPDF#: 00-026-0792, Appendix D). Although this was a polymorph of iron oxide hydroxide, it could have stabilized due to its dimensions on the micron-nano scale, where the surface energy may play a bigger role

[177]. As for Fe S-Silica particles (Figure 4.4), there were no crystal shards present or measureable diffraction spots or rings. However, a particle coating is present on the silica particles (possibly iron oxide, from Figure 4.5, discussed next).

Figure 4.5 and 4.6 showed that iron oxides were present on the surface of silica and were present off the silica particles. Although several papers [178-181] have cited the work done by Ghio [92], there have not been any studies specifically about the iron state obtained with this method. The assumption was that iron complexed on the surface of silica. The EELS spectrum shows evidence of iron oxides formed on the surface of the silica nanoparticles. The iron oxides located off the silica particles either formed on their own or disassociated with silica after their formation. The washing protocol after coating the silica with iron could have also removed the iron particles off the silica. Alternatively, the drying step for TEM preparation for the iron coated silica may form iron oxide from drying. The iron oxides or hydroxides were present; however, they do not show a crystal structure. These iron oxides on the surface of silica could be ferrihydrite, which is amorphous. The iron oxide hydroxide may be formed from the ferrihydrite on both Fe C-Silica and S-Silica nanoparticles due to the drying process.

The iron oxides located on the surface of the silica particles and located off the particles appear to be the same. However, the oxidation state of the iron oxide in the Fe C-Silica samples is different from the Fe S-Silica particles. The presence of a pre-edge peak in the oxygen profile shows that the iron oxide is more oxidized in the C-Silica compared to S-Silica sample [97, 116] (See Figure 2.6 in Chapter 2) . The ferrihydrite present is Fe^{3+}. However, this may be difficult to determine since beam damage could also oxidize the particles. Also, different oxidation states could be present on the iron oxide between its core and edge [43]. Figure 4.7 and 4.8 showed that the Fe S-Silica nanoparticles were sensitive to beam damage. When iron was present, interaction of the beam can precipitate iron oxide particles on the surface of the silica particles. This makes observation of the particles difficult for electron diffraction if the iron oxide formed is due to beam interaction. Regardless, an iron oxide coating on both the surface for both C-Silica and S-Silica were present after using the protocol by Ghio [92].

4.2.3 Oxidation State of Iron and Speciation of Iron Oxide on Silica

Using STXM, the comparison of different samples of Fe coated on SiO2 particles confirmed that all Fe present was Fe^{3+} with no evidence for reduction to Fe^{2+} (Figure 4.9). The XANES (X-Ray Absorption Near Edge Structures) spectra (Figure 4.9A) were generally similar to each other and to the ferrihydrite reference spectrum, with only minor differences evident in the first-derivative spectra. Features in the spectrum of sample Fe S-Silica suggested a minor component of aqueous Fe^{3+}, probably residual from the solution used in sample preparation. Comparison of the EXAFS (Extended X-Ray Absorption Fine Structure) spectra of the two Fe C-Silica samples with amorphous ferrihydrite and crystalline goethite reference spectra (Figure 4.9B) confirmed that Fe coated on SiO_2 nanoparticles has a local atomic structure nearly identical to that of ferrihydrite precipitated from solution and dried immediately without aging. The amplitude of the second-neighbor Fe-Fe peak in the Fourier transform (FT) was similar between the Fe C-Silica and ferrihydrite, indicating a similar local atomic ordering and particle size. The spectrum of goethite was distinctly different, with strong second-

neighbor Fe-Fe scattering and additional fine structure at high k (greater distance in the FT), and reflected a high degree of local ordering expected of crystalline material. Goethite is a common iron hydroxide mineral found in soils. The iron oxide present was ferrihydrite that was coating both silica samples. When the Fe S-Silica sample was completely dried, it showed the presence of ferrihydrite. When it was not completely dried, aqueous Fe^{3+} ions were present from the $FeCl_3$ used to coat the particles. Based on these results, the S-Silica particles, if not completely dried, did not coat with ferrihydrite, but contained soluble ferric chloride.

4.2.4 Mesoporous Silica: Tianjin Chemist Scientific

Testing mesoporous silica toxicity was used to determine the effect of surface area on air pollution. XRD (Figure 4.10) analysis showed that both types of silica particles were non-crystalline [182, 183]. The total BET surface area for solid silica was 1.72 ± 0.05 m^2/g and for mesoporous silica was 774.3 ± 1.04 m^2/g. Since total BET surface area measured pore and particle surface area for porous structures [15, 16], the mesoporous silica had 600 times more total surface area per unit mass than solid silica. The total surface area measurement for solid silica was consistent with calculations based on spherical particles as shown in the SEM images (Figure 4.11), and the high surface area of the mesoporous silica particles was consistent with the manufacturer's datasheet and results from previous studies [184, 185]. The characterization results indicated that both particle types had a similar size and were non-crystalline, with the primary difference being number of particles and surface area (Figure 4.11 and 4.12). The isotherms indicated that the external surface area of the mesoporous silica is 60.20 m^2/g compared to its total surface area of 746.95 m^2/g. Furthermore, calculated pore volume was 0.60 cm^3/g. The BET isotherms in Figure 4.13A were consistent with the literature for MCM-41 materials [186]. The external surface area for MCM-41 materials were between 60 to 150 m^2/g as reported by Wloch et al. [187], much less than the total surface area of 774.3 m^2/g.

4.2.4 Mesoporous Silica: Lab Synthesized MCM-41

Figure 4.14, images of the lab synthesized 50 nm mesoporous MCM-41 silica particles show that their size was similar to the particles made from Stöber synthesis. In contrast to the particles from Tianjin chemist, these particles aggregated less and dispersed more evenly. MTT assay was used to determine the toxicity and RT-PCR was used to determine the production of pro-inflammatory mediators of these silica particles.

4.2.5 Crystalline Silica: PARR Synthesis

Nanoscale quartz is an important material for its potential piezoelectric properties and its usefulness for assessing cellular toxicity. Synthesis of quartz nanoparticles would be useful for toxicity studies in the lungs since these particles are naturally airborne [188]. However, due to quartz's energetic similarity to amorphous silica, high growth rate at higher temperatures, and necessity for precisely basic conditions, a chemical synthesis was difficult [189]. Via a hydrothermal synthesis [94], it was possible to get the necessary conditions for quartz nucleation and growth by controlling the temperature in the pressure vessel and optimizing the reagents used: ethanol as a solvent, NaCl and

NaOH as mineralizers and preservers of basicity, and monodisperse Stöber amorphous silica as a precursor.

In Figure 4.15A, the average particle diameter was 59.4± 8.47 nm (n = 29), but they were aggregated. The aggregation seen was likely from uneven stirring and limitations of the PARR speed (600 rpm max) [94]. The observed small spheres were about 5.6 ± 1.93 nm in diameter. In Figure 1.15B, the average particle diameter was 7.9 ± 1.74 nm (n = 209). The small particles could be the quartz of uneven size distribution [189].   The larger particle (40.59 nm) in Figure 4.15B had size comparable to the non-crystalline silica pre-cursors. In Figure 4.15C and 4.15D, the lattice fringes indicated by the arrow were 0.34 and 0.77 nm, respectively. The d-spacings of quartz's (101) planes are 0.334 nm, comparable to the d-spacings measured in Figure 4.15C. In Figure 4.15D, the lattice fringes have a d-spacing too large to match any quartz or salt d-spacings. This could have been due to the presence of metal contaminants since some metallic compounds, like iron, have d-spacings 0.75-0.85 nm. It was difficult to remove the metal contamination because the stirring system of the PARR reactor used a metal stir to mix the sample.

The characterization data shows the product is mostly salts (NaCl) with quartz (JCPDF: 46-1045) nanoparticles of an uneven size distribution. In Figure 4.15E, the unknown peak at 42° (2θ) (d-spacing 0.248 nm) loosely matches stainless steel (JCPDF: 33-0397) or sodium iron silicate (JCPDF: 18-1222) near this diffraction angle, based on d-spacings; the unknown peak at 21° (2θ) (d-spacing 0.496 nm) does not match stainless steel diffraction peaks but could be NaOH. Autoclaves of metal alloys typically contaminate samples [94]. Based on these results, the synthesis produced a small yield of crystalline silica; however, it was too heavily loaded with salts and metal contaminants. Future work includes iterations of this experiment with a refined washing procedure to increase quartz yield, remove excess salt, and to decrease metal contamination. However, for the proxy PM particle, using crystalline silica to model it may not be important, since analysis of natural PM analysis showed it did not contain crystalline silica, contrary to expectations.

4.3 Silica Preliminary Biological Response
4.3.1 C-Silica vs. S-Silica

MTT Assay was used to test cell viability for S-Silica with and without iron coating on THP-1 human monocyte-derived macrophages (Figure 4.16). Previous work on C-Silica showed similar results. Silica toxicity was not significantly different from "no treatment" until the silica concentration reached 100 µg/ml. Natural silica particles, Min-u-sil 5, labeled as "Ambient", was tested as a positive control, since prior studies have seen its toxicity [82]. Figure 4.17 (A and B) show the mRNA fold change for TNF-α and IL-1β for C-Silica compared to S-Silica. Relative to the control (no particle treatment), the increase in concentration from 10 to 25 µg/ml of C-Silica did not show a difference in response. There was only a significant response for the C-Silica particles when iron was present. An increase in concentration of C-silica did not have an increased effect, but the presence of iron did for both TNF-α and IL-1β. On the other hand, the S-Silica particles with or without an iron coating showed no difference in mRNA fold change for TNF-α and IL-1β. There appeared to be a difference with

increased concentration but the values were not significant. Future experiments can confirm these effects. However, these preliminary results showed that the Fe C-Silica (Fe C-Si) had a great biological effect compared to the Fe S-Silica (Fe S-Si).

Although there was more iron content for the iron coated S-Silica detected ICP-MS, there was no biological response compared to the lower iron content of Fe C-Silica (Table 4.1). For C-Silica, there was an enhanced inflammatory response when iron was present as seen in previous results with iron and silica [57, 82]. The concentration of iron was higher for the S-Silica, but it did not have a biological effect, indicating that the type of iron oxide present for the Fe S-Silica sample was different from Fe C-Silica as shown by the XANES in Figure 4.9A. Most of the iron present was Fe $^{3+}$ ions for Fe S-Silica and did not cause a biological effect. In addition, the shards present with Fe C-Silica can pierce cells and cause cell death (Figure 4.3) similar to asbestos [178, 190].

Figure 4.18 show the Preliminary Biological data for S-Silica for GCLC, HO-1, and IL-1β at different hour treatments for mRNA fold change. GCLC codes for glutamate-cysteine ligase catalytic subunit for glutathione synthesis. Glutathione synthesis helps reduce oxidative stress [191].   In Figure 4.18A, there were preliminary results for GCLC mRNA expression decreased (relative to the control) at 3 hrs, comparable to the control at 6hrs, and slowly increased at 18 hrs. This indicated that regardless of the presence of iron, the concentration of silica effected the GCLC expression. The HO-1 (Heme oxygenase 1) catalyzed the reduction of heme to produce iron, carbon monoxide, and biliverdin. Biliverdin converted via biliverdin reductase to bilirubin, a powerful anti-oxidant to prevent inflammation. HO-1 could be induced by LPS, pro-inflammatory cytokines, and heavy metals [192]. As shown in Figure 4.18B, the LPS induced HO-1 mRNA expression. However, iron on Fe S-Silica did not affect HO-1 induction without IL-1β induction as expected.

4.3.2 Mesoporous Silica: Tianjin Chemist Scientific

This study characterized mesoporous silica particles from Tianjin Chemist Scientific. After characterizing the particles, the MTT assay assessed cytotoxicity on THP-1 human monocyte-derived macrophages (Figure 4.19). MTT assay was a common test for cell viability following particle exposure; however, other studies suggested that mesoporous particles may interfere with the assay [193, 194]. Therefore, this minimized the effects of particle interference with different controls for the MTT assay (See Chapter 2). There was a significant difference in cell viability between the solid and mesoporous silica compared to the control ($^{+}$P<0.05), and there was a significant difference between the solid and mesoporous silica (*P<0.05) (Figure 4.19). While the size of solid silica and mesoporous silica particles were similar, per unit mass there was a ~4X increase in the number of mesoporous particles delivered to cells relative to solid particles, due to their lower density and morphology. At the same time, there was a 600-fold increase in total surface area for mesoporous over solid silica, due to both the increased particle surface area and pore surface area. The relatively modest increase of toxicity of mesoporous silica suggested that particle surface area was important, and that the toxicity mechanism required particle surface to cell contact.

To determine if direct interaction of the particle with the cell surface occurred, this study tested the production of membrane lipid hydroperoxides upon treating cells

with silica particles using DPPP. DPPP incorporates into the cell membrane and reacted with lipid hydroperoxides selectively and stoichiometrically to give DPPP=O, which due to its high fluorescence intensity could be microscopically imaged [195, 196]. The fluorescence intensity of DPPP was greater in cells treated with engineered mesoporous silica (Figure 4.19 C) compared to cells treated with 100 µg/ml engineered solid silica particles (Figure 4.19 B), supporting the conclusion that the toxicity mechanism required particle surface/cell contact.

As expected from our previous results, there was a decrease in the cell viability as the concentration of mesoporous silica increased. However, the decrease was greater than our previous results with 100 µg/ml. Here, we used serum free media before adding the MTT assay, since serum bovine media interfered with the MTT Assay. Even at low doses, there was reduced cell viability and production of inflammatory mediator production at low doses (P>0.05). Furthermore, there was less external surface area for the mesoporous silica compared to its total surface area. Based on the surface charge, around pH 7.4, the mesoporous silica aggregated (Figure 4.13B). This reduced the effective external surface area and caused the reduction of inflammatory mediator production at low doses. There was a far less cell contact for exposure. MTT assay tested cell viability, and RT-PCR tested mRNA expression for mesoporous silica at different concentrations (Figure 4.20). A high concentration of mesoporous silica resulted in cell death. There were also decreases in mRNA fold change as the concentration of mesoporous silica concentrations increased. This decrease in mRNA was due to cell death upon interaction with mesoporous silica.

4.3.3 Mesoporous Silica: MCM-41

The 50 nm lab synthesized Mesoporous silica (MCM-41) was tested for cell viability in THP-1 human monocyte-derived macrophages using MTT assay and compared to the S-silica (referred as simply silica here) with different coatings of iron and quinone. The external controls showed the assay was working (Figure 4.21A). The 100 µg/mL of "Ambient" silica (Min-u-sil 5) showed less cell viability, which was conclusive since there was a stimulus added to the cells. The 50% viability check had half the volume of cells as the control. Since the cell viability was half of the control, the assay was assessing cell viability correctly. In Figure 4.21B, the toxic dosage started at 10 µg/mL for PBS, Iron, Solid Silica, and MCM-41. Toxicity for Iron/quinone coated silica started 50 µg/ml. Quinone doped silica toxicity began at 100 µg/ml. The silica seemed to show a linear progression in toxicity based on concentration added to the cells whereas the MCM-41 showed a quick drop off at 10µg/ml. This shows that solid silica by itself was toxic without manipulating the surface or nanostructure. Based on the results and data analysis, the mesoporous silica produced the greatest toxicity (lowest cell viability). Since mesoporous silica was less dense than the other particles, more particles interacted with the cells per mass dose. In addition, depending on the pore size, more surface area of the MCM-41 could interact with the cells compared to solid silica samples. As for the iron, quinone, and iron quinone coated samples, that quinones may be slightly protective to the cell. This would explain why the iron quinone samples have higher cell viability than the iron samples at a higher concentration. The quinones may

be attenuating the toxicity of the iron. It is suspected that the phase II genes are being activated, thus protecting the cells [197].

4.4 Evaluation of Proxy Silica-based Particulate Matter Particles

Silica nanoparticles served as a good model for aluminosilicates. There are readily available size control protocols for its synthesis, and its size is adjustable for future experiments. In addition, the ferrihydrite successfully coated the surface of the silica nanoparticles to mimic natural PM particles. Furthermore, the silica particles induced different biological responses based on their coating (iron, quinone, or both) or lack of coating. This was promising as it shows that the surface coating had a major effect on cell toxicity. In the future, different biological tests can explore the effects of the different surface coating concentrations. To control the amount of iron coated on silica, different concentrations of iron (III) chloride can coat the silica. Mesoporous silica particles were too toxic as a proxy PM particle, however, its effect on particle dose and surface area was useful to observe. In future experiments, mesoporous and non-porous silica delivery can be based on particle number dose (number of individual silica particles) instead of total mass dose. Techniques, such as nanoparticle tracking analysis, dynamic light scattering, and flow cytometry can be used to determine the particle count per volume of solution [198, 199].

Although, the above qualities make silica a good proxy PM particle, some qualities need improvement, such as the formation of the ferrihydrite. After mixing iron (III) chloride with silica, completely dried particles contained more ferrihydrite on its surface. However, the ferrihydrite aged to form the crystalline spindles (Figure 4.3). Depending on the water content and temperature over time, ferrihydrite aged to form goethite at either pH 4 or pH 12 via dissolution and re-precipitation; or it aged to form hematite (α-Fe_2O_3) at pH 7-8 via internal aggregation and rearrangement (i.e. direct dehydration) [139]. However, the presence of silicates impeded the conversion of ferrihydrite into either goethite or hematite. Silicates (H_4SiO_4, $H_3SiO_4^-$, and $H_2SiO_4^{2-}$) modify the surface area, solubility, and dehydroxylation of ferrihydrite and prevent the formation of hematite and goethite [200, 201]. As a result, a mixed crystalline phase formed with both properties of goethite and hematite. In Figure 4.3, an unknown iron hydroxide was a mixed crystalline phase of goethite and hematite. The surface of silica nanoparticles, C-Silica, acted as silicates and impeded the ferrihydrite conversion into goethite/hematite. The silica solution is generally alkaline and the addition of iron (III) chloride would have brought the pH to neutral, favoring hematite formation. The spindles seen in Figure 4.3 also look similar to hematite spindles with some differences attributed to goethite formation [200, 202, 203]. In addition, after coating the silica particles, the color can identify the iron oxide present: Goethite is yellow; hematite is red; and ferrihydrite is dark brown. If both goethite and hematite is formed, both colors may be seen [204].

Based on the results above, since ferrihydrite converts into goethite and hematite over time, characterization and biological tests need freshly prepared, reproducible samples to verify the state of ferrihydrite and its biological effects. On the other hand the sample can also be allowed to age to form the mixed crystalline phase of goethite and hematite and biologically tested. To improve on this model, more stable iron oxides

phases, such as goethite (FeO(OH)) [205-207], can also be coated on the surface of silica instead. In future work, an aluminosilicate proxy PM can replace silica. There are several methods to synthesize micrometer size aluminosilicates [208, 209]. In addition, there is a new method to synthesize nano-sized non-crystalline aluminosilicates [134]; although, size control methods need improvement for aluminosilicates for a representative sample of PM in the SJV.

4.5 Conclusions

Silica is a good proxy PM particle to use in biological tests of PM health risks. The drying process for the iron coated particles was important in the formation of ferrihydrite. Based on the TEM results, the major difference between the Fe C-Silica and Fe S-Silica samples were the presence of crystalline spindles in Fe C-Silica samples due to the formation of hematite and goethite mixed crystal in the presence of silicates. Iron precipitated in the form of ferrihydrite on all the samples with some residual Fe^{3+} ions when samples completely dried after iron coating. These results showed that using silica nanoparticles as a model nPM could be useful in determining the significance of the type of iron hydroxide present on silica and in linking the biological effects and outcomes. The total iron concentration was not important as the type of iron on the surface of the nanoparticles. The presence of ferrihydrite was important for initiating a biological response with silica particles.

Mesoporous silica was more toxic than solid silica. On a mass basis, mesoporous silica reduced cell viability from $82 \pm 8\%$ to $73 \pm 16\%$ compared to solid silica, likely due to decreased density and therefore increased particle and surface area interaction. This increased in toxicity, compared to the dramatic 600-fold increase in total surface area for mesoporous silica (attributable to both pore and particle surfaces), suggested that the toxicity mechanism depended on the surface area available to the cell and not the total surface area. DPPP results supported this conclusion and indicated that membrane lipid peroxidation was involved. The lab synthesized MCM-41 particles were more toxic than the solid silica particles due to increase dosage at the same mass. In addition, the silica particles coated with quinone were less toxic to the cells compared to the iron coated silica particles. Quinones can induce NAD(P)H:quinone oxidoreductase 1 (NQO1), which prevents the production of quinones and thereby the production of superoxide and hydrogen peroxide, providing protection to the cell [210]. These different particles coatings can represent different chemical species on the proxy silica PM particles. In terms of mitigation strategies, the effects of nano-size and surface area are important parameters for toxicity. Reductions of nanoparticles emissions and particles with increased surface area can be targets for mitigation and improvement of air quality health, such as fine PM compared to coarse PM.

4.6 Figures and Figure Legends

	Average Particle Size, nm	BET Surface Area, m^2/g	Iron Concentration, mmol/g silica	Surface Iron, mmoles/m^2 silica
C-Silica	41.7 $\pm$ 5.9	54.5	0.06 $\pm$ 0.07	0.0011
Fe C-Silica	40.6 $\pm$ 6.2	54.5	0.43 $\pm$ 0.22	0.0079
S-Silica	42.7 $\pm$ 6.3	53.1	0.13 $\pm$ 0.08	0.0024
Fe S-Silica	43.8 $\pm$ 6.3	53.1	7.62 $\pm$ 0.18	0.1435
Fe S-Silica (Dried)	-	53.1	1.85 $\pm$ 0.25	0.0348

Table 4.1: Size Distribution of Commerical and Synthesized Silica Nanoparticles
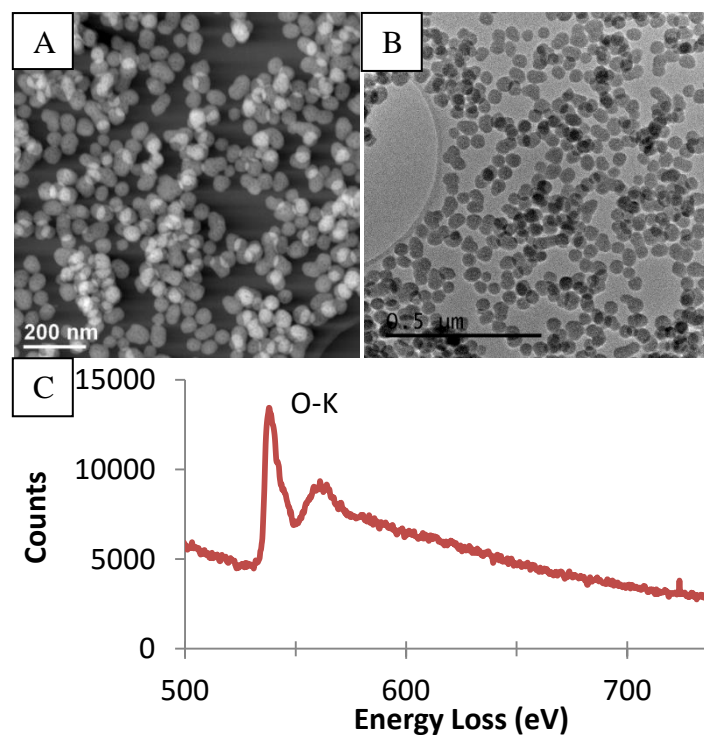
Figure 4.1: Commercial Silica. (A) STEM image and (B) Bright Field TEM image of silica nanoparticles purchased from Microspheres and Nanospheres Company. (C) EELS of Commercial Silica (C-Silica) between 500 and 750 eV.
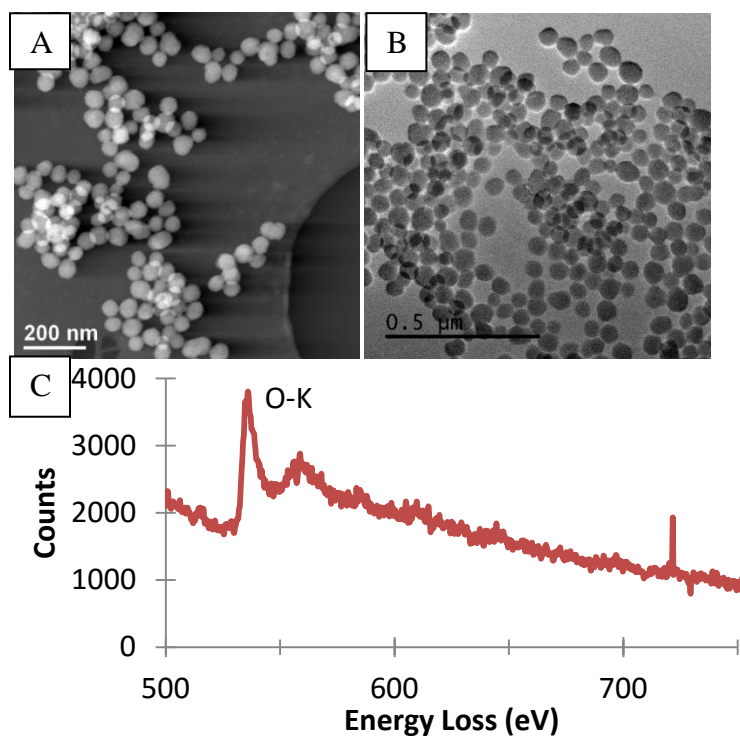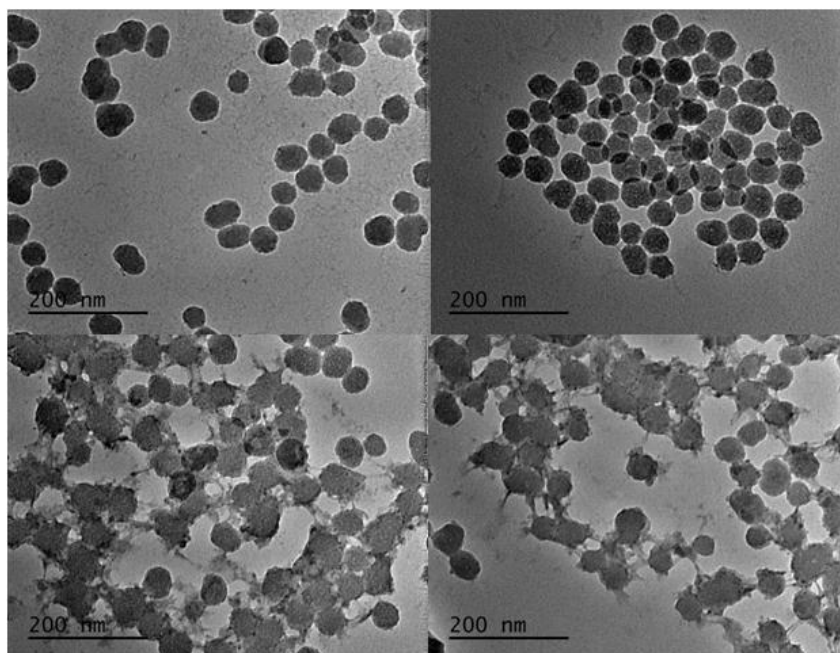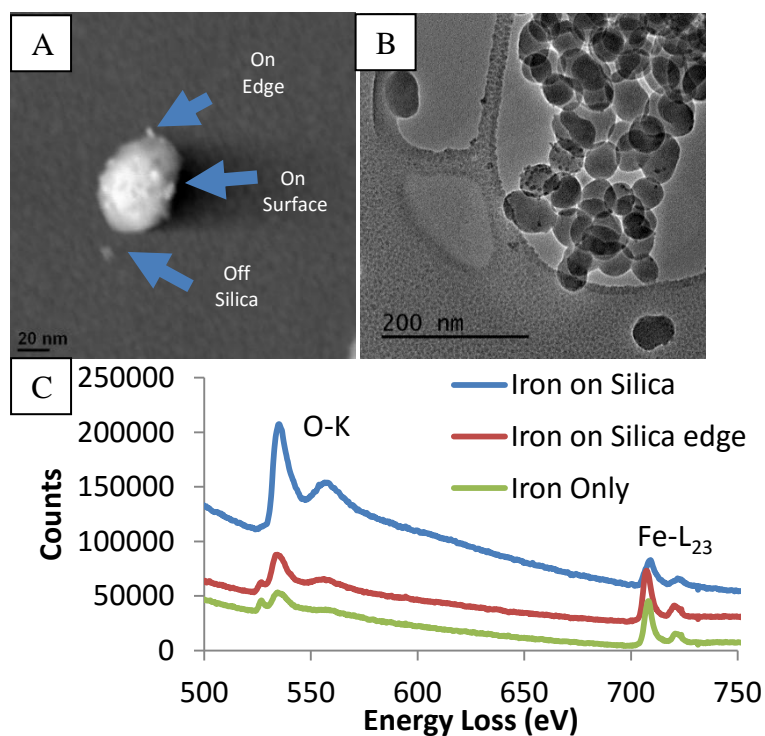
Figure 4.2: Synthesized Not-Dried Silica Nanoparticles (A) STEM image and (B) Bright Field TEM image of Synthesized Silica (S-Silica) nanoparticles and (C) EELS signal from Synthesized Silica sample.
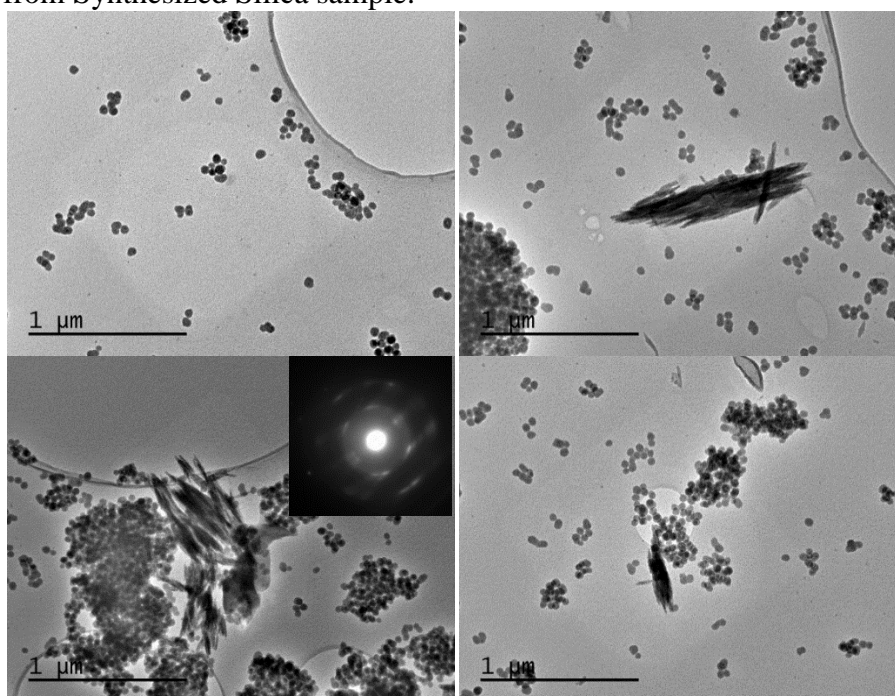

**Figure 4.3:** TEM images of Iron Coated Commercial Silica (Fe C-Silica).

Figure 4.4: TEM of Iron Coated Synthesized Silica (Fe S-Silica)


Figure 4.5: Iron Coated Commercial Silica (Fe C-Silica) (A) STEM image and (B) Bright Field Image of nanoparticles. (C) EELS spectra of Iron on silica (top spectrum), on the edge of silica (middle spectrum), and off silica (bottom spectrum), spectra offset to see individual spectra. Iron signal is similar for all summed spectra (n = 6). Pre-edge peak was present in Oxygen. Iron on and silica and on the edge are identical.
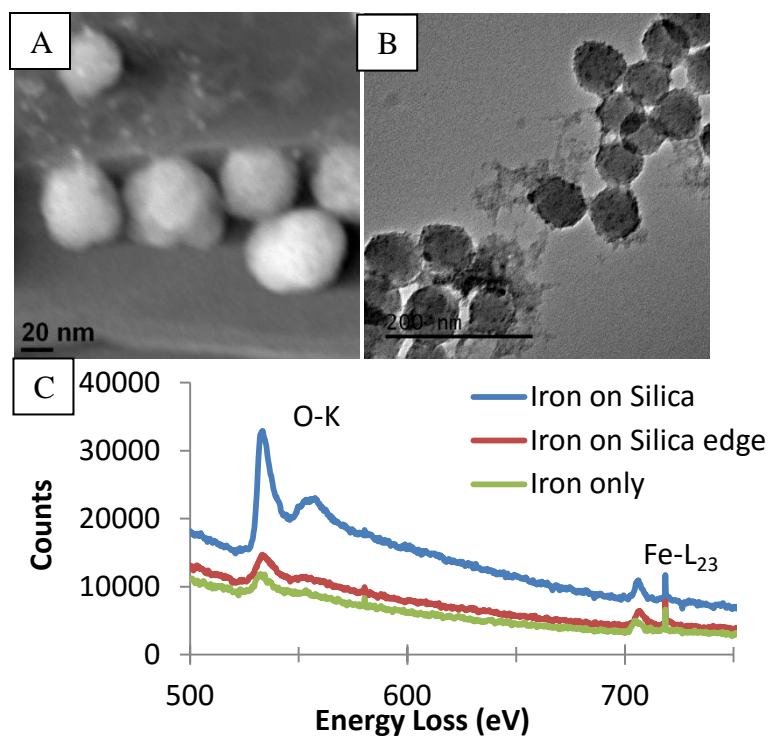
Figure 4.6: Iron Coated Synthesized Silica (Fe S-Silica) (A) STEM image (B) Bright Field TEM image and (C) Comparison of EELS of the iron on silica (top spectrum), on the edge of silica (middle spectrum), and off the silica particle (bottom spectrum). Iron $L_{2,3}$ signals looked similar to each other.
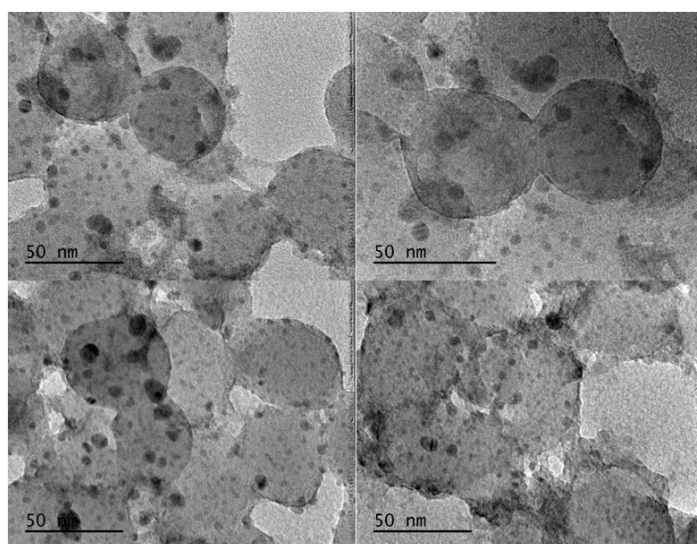
Figure 4.7: HRTEM of iron oxide particles on Iron Coated Synthesized Silica (Fe S-Silica) nanoparticles
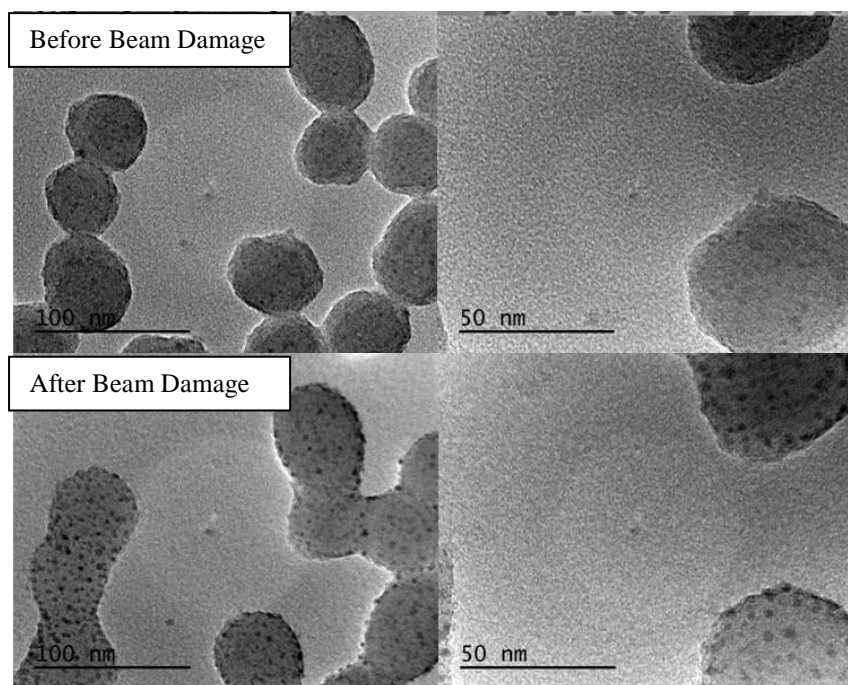
Figure 4.8: Beam damage with Iron Coated Synthesized Silica (Fe S-Silica). The electron beam was at crossover on the sample for at least 5 seconds at 200 keV.
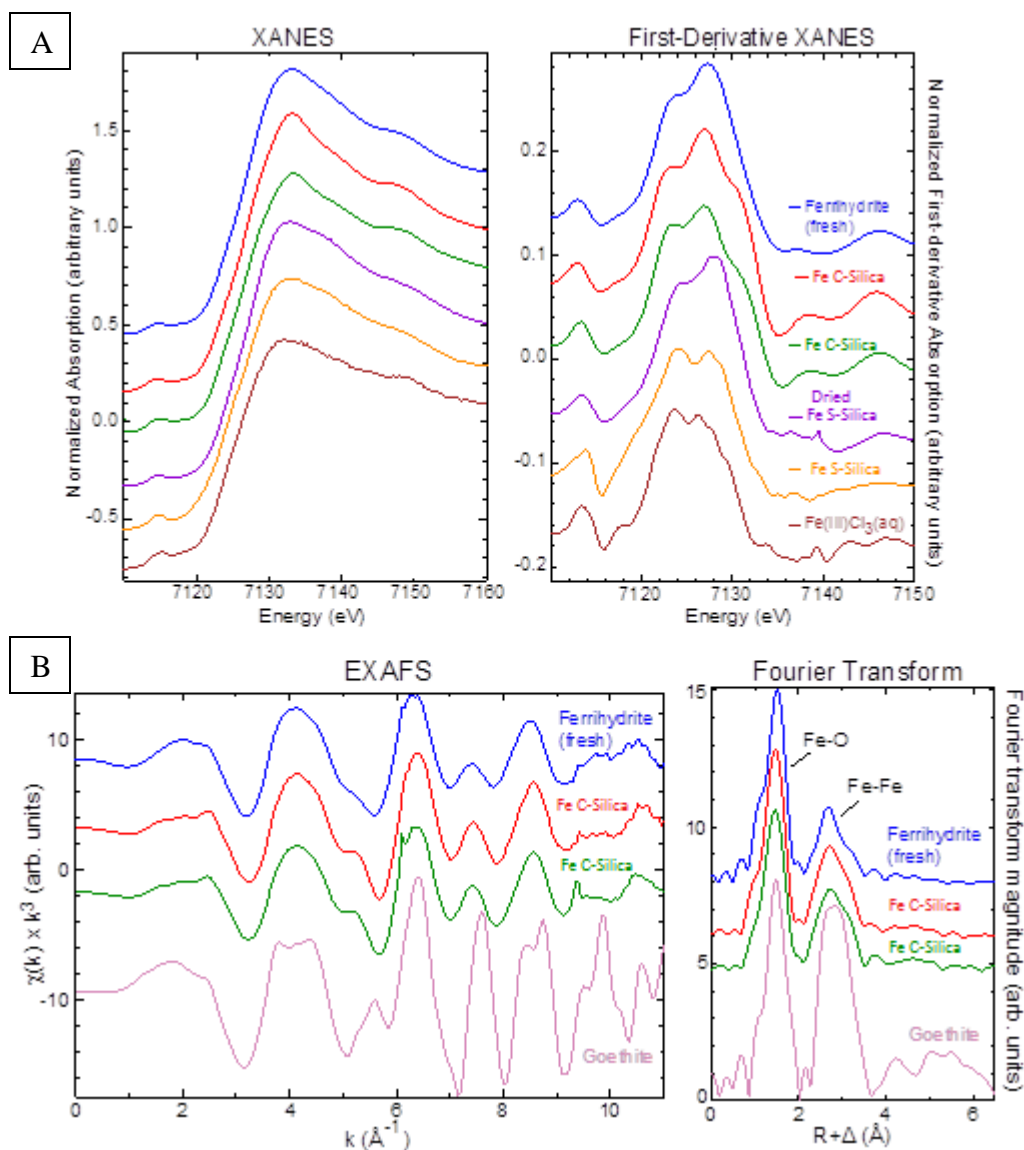
Figure 4.9: (A) Normalized XANES and corresponding first-derivative spectra of Fe coated on C-Silica nanoparticles compared to reference spectra of freshly precipitated and dried ferrihydrite ($Fe(OH)_3(s)$) and an aqueous solution of $Fe^{3+}Cl_3$ (50 μM). (B) EXAFS spectra of the Fe C-Silica samples from (A) compared with the EXAFS reference spectra of ferrihydrite (from (A)) and crystalline goethite (synthetic FeOOH).
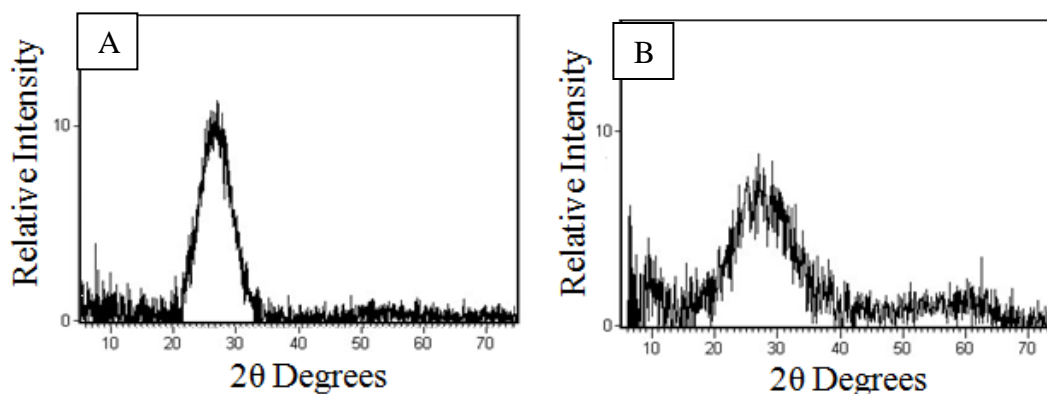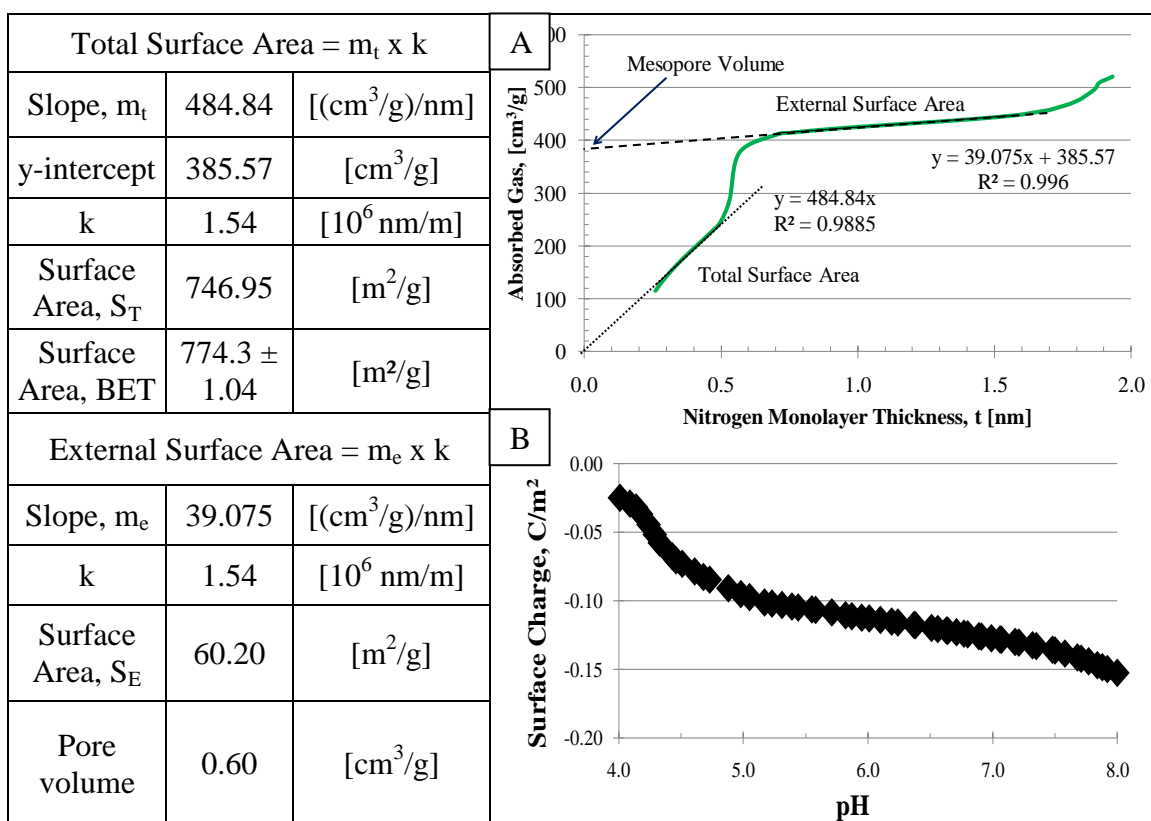
Figure 4.10: X-Ray Diffraction of solid silica (A) and mesoporous silica (B). There is a broad peak in both solid and mesoporous silica.
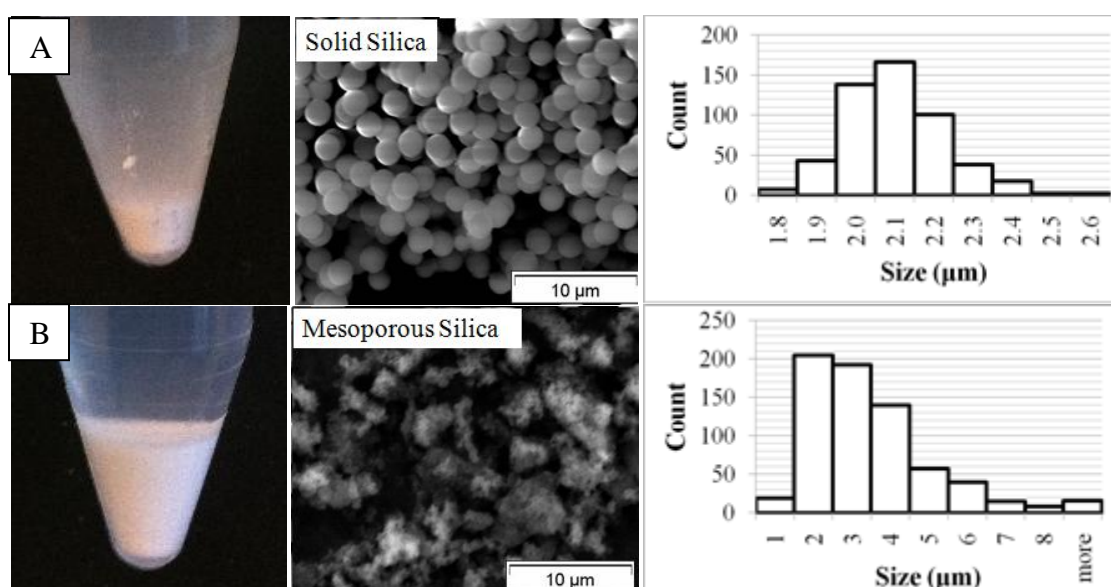
**Figure 4.11**: Particle Relative Density and Size distribution. (A) The solid silica has less volume (about 4 times less volume) than (B) mesoporous silica at the same mass (100 mg). The solid silica are uniform spheres with an average diameter of 2.05 ± 0.18 μm, while the mesoporous size separated engineered mesoporous silica particles are irregularly shaped and have an average particle diameter of 3.03 ± 1.78 μm.
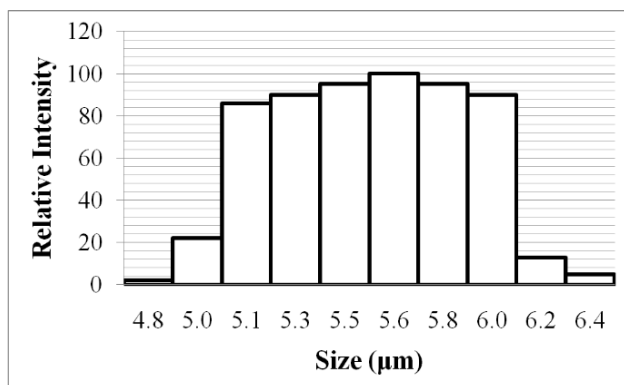
Figure 4.12: Size Distribution of mesoporous silica by Dynamic Light Scattering. The average hydrodynamic diameter was 5.57 ± 0.40 μm.

| Total Surface Area = m_t x k			A
Slope, m_t	484.84	$[(cm^3/g)/nm]$	
y-intercept	385.57	$[cm^3/g]$	
k	1.54	$[10^6\,nm/m]$	
Surface Area, S_T	746.95	$[m^2/g]$	
Surface Area, BET	774.3 $\pm$ 1.04	$[m^2/g]$	
External Surface Area = m_e x k			B
Slope, m_e	39.075	$[(cm^3/g)/nm]$	
k	1.54	$[10^6\,nm/m]$	
Surface Area, S_E	60.20	$[m^2/g]$	
Pore volume	0.60	$[cm^3/g]$	

Figure 4.13: BET isotherm data (A) results using the t-plots and (B) Relative surface charge of mesoporous silica for a 10^{-3} M NaCl solution as a function of pH. The point of zero charge is below near pH 3.5 and the charge is more negative as the pH increases.
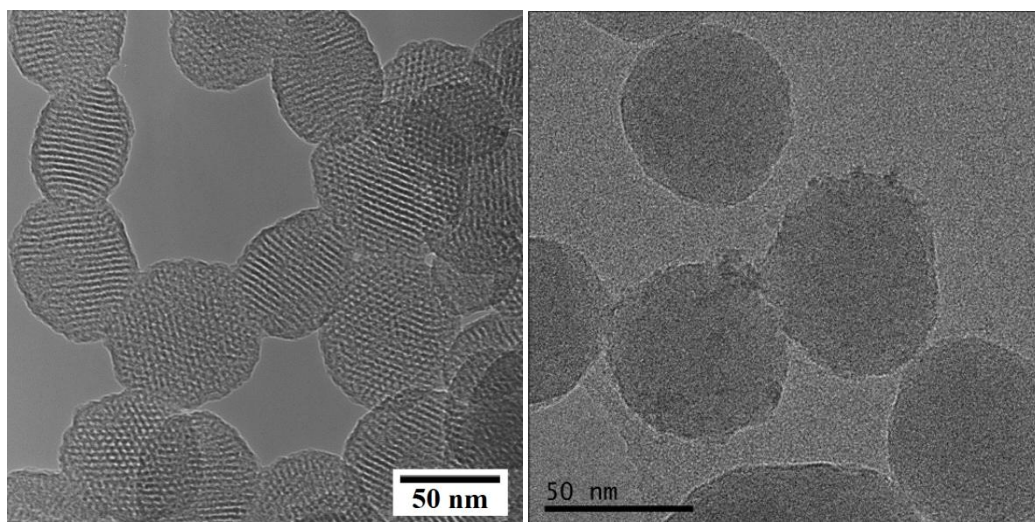
Figure 4.14: 50nm Mesoporous MCM 41 Silica particles vs. Coated Silica particles.
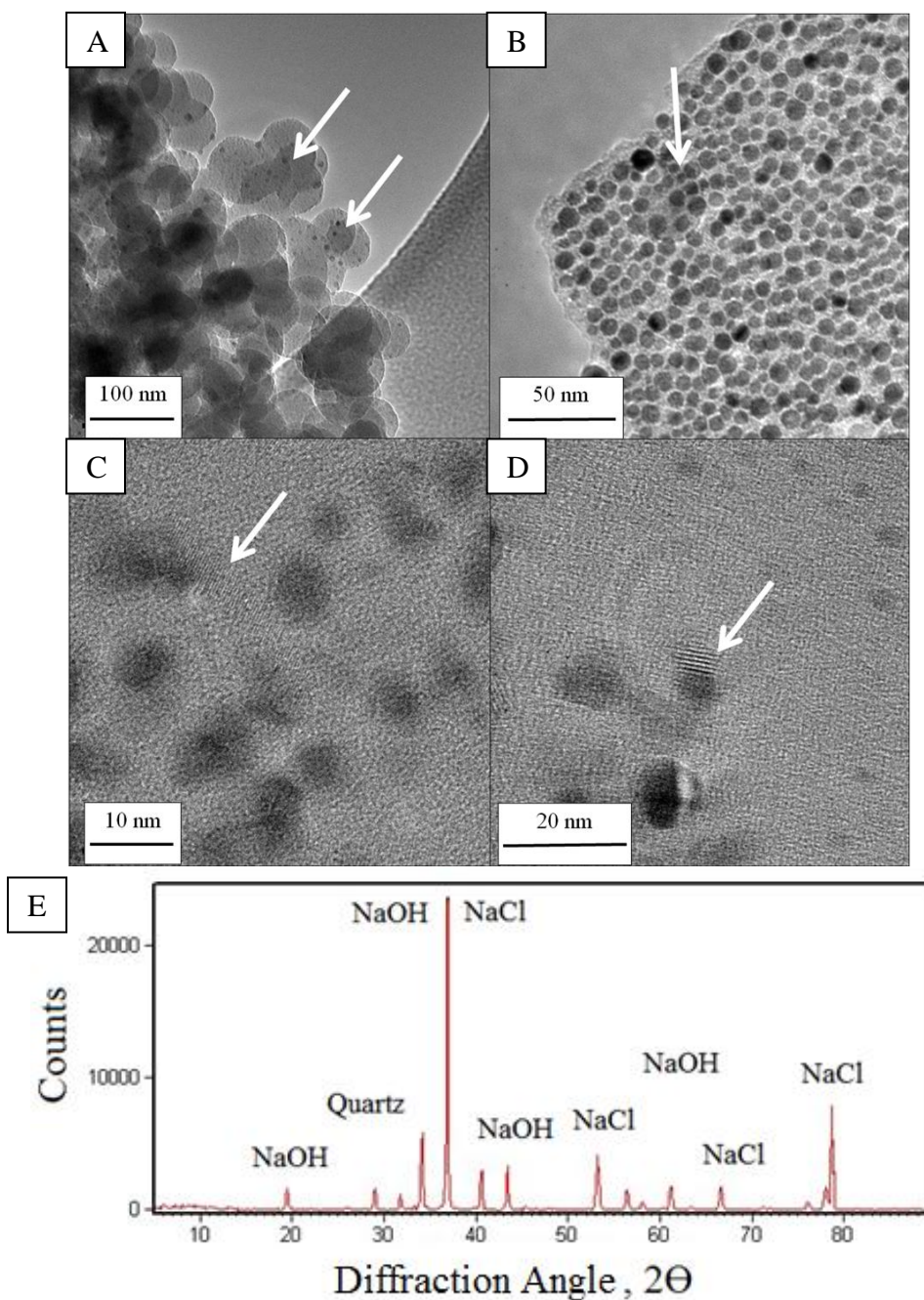
Figure 4.15: TEM micrographs of (A-D) Crystalline Silica Particles from PARR synthesis and (E) XRD of PARR reaction contents. A) Average particle diameter: 59.4 ± 8.47 nm out of 29 particles. Small black dots (5.6 ± 1.93 nm in diameter, on average) B) Average particle diameter: 7.9 ± 1.74 nm (n = 209). Large particle (40.59 nm) indicated by arrow (C) Lattice fringes indicated by arrow; calculated d-spacing is 0.34 nm. (D) Lattice fringes indicated by arrow; calculated d-spacing is 0.77 nm. (E) XRD mainly shows α-quartz (JCPDF: 46-1045), NaCl, and NaOH.
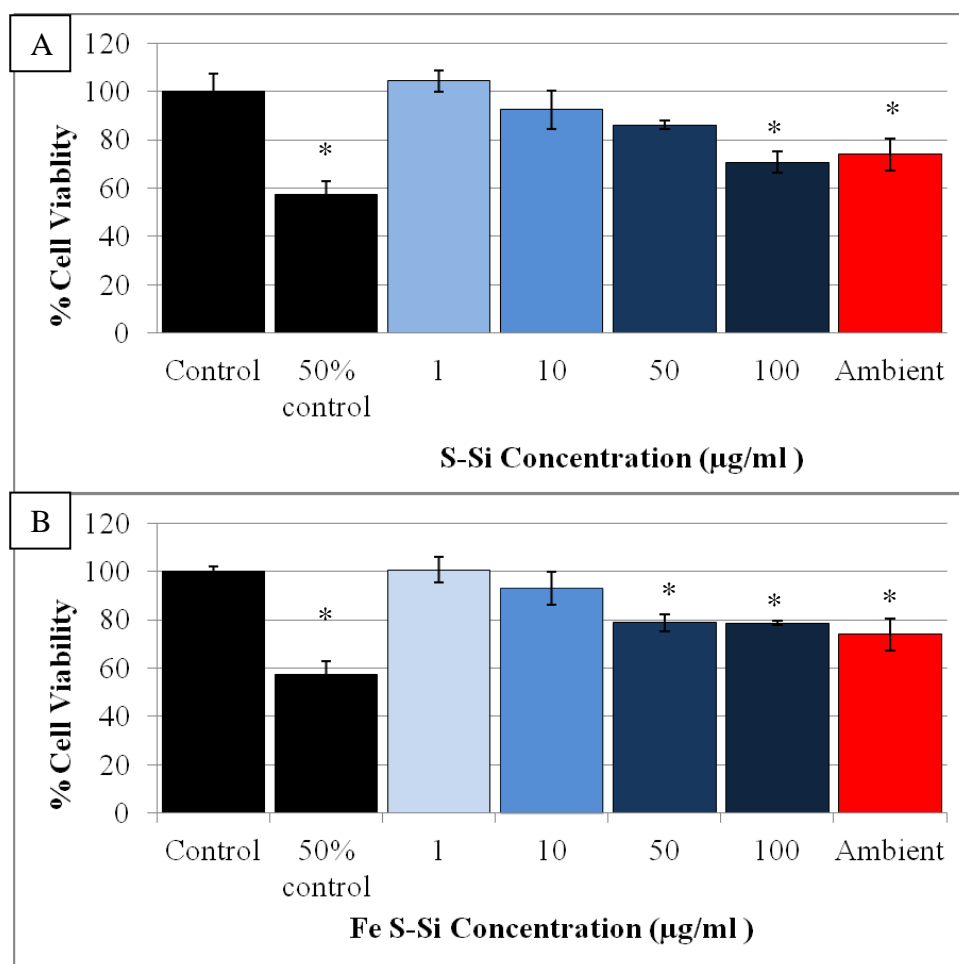
Figure 4.16: Cell viability of Silica vs. Iron Coated Silica. The control had no particle treatment. Ambient was micrometer sized crystalline silica (Min-u-sil 5), which was known to induce cell death a 100µg/ml concentration. *Significant by Anova relative to Control. 50% control was no particle treatment with half the number of cells seeded relative to control.
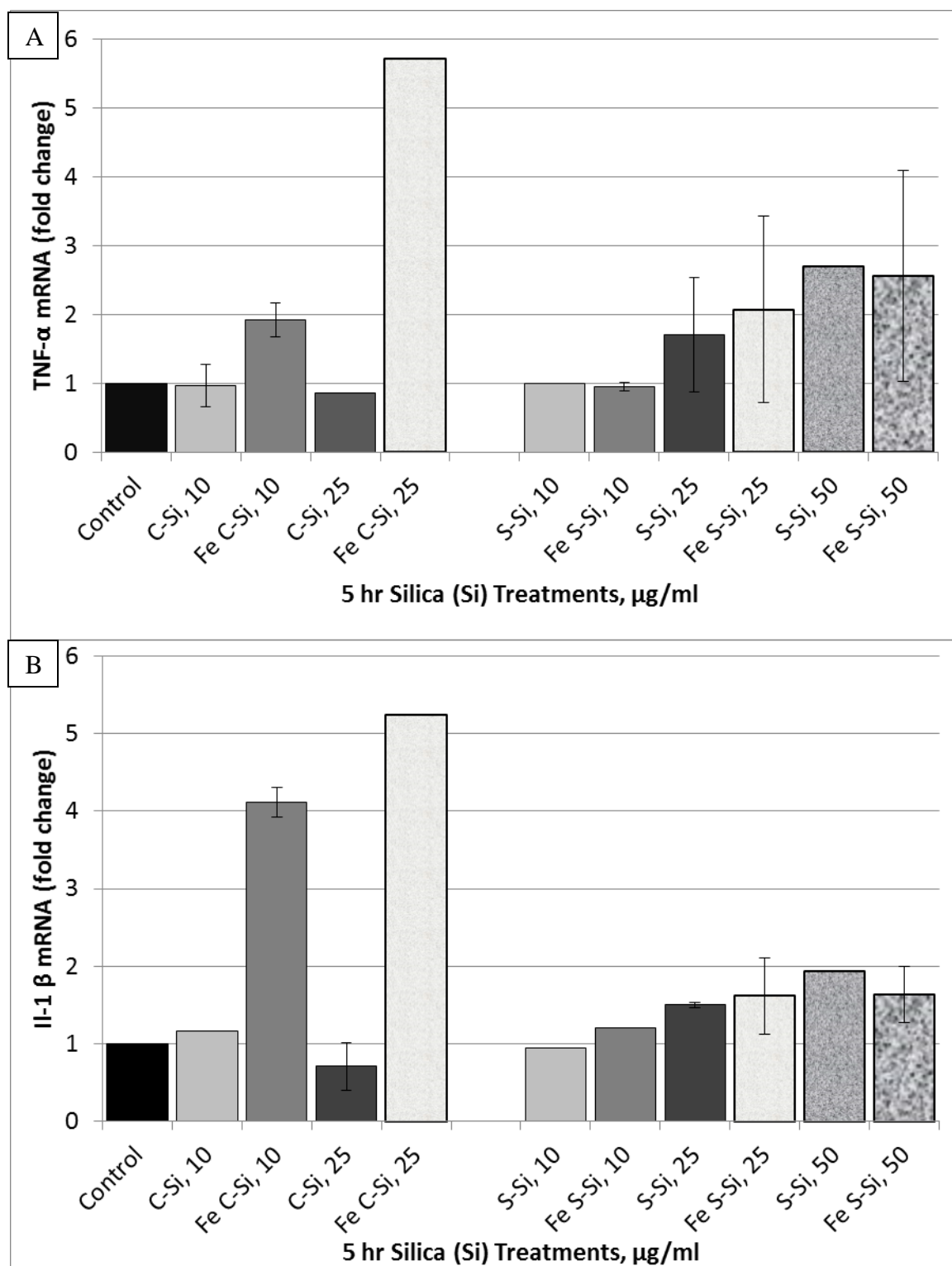
Figure 4.17: Preliminary Data for 5hr treatments for Cytokine mRNA (A) TNF-α and
(B) Il-1β for C-Silica and S-Silica with and without iron coating.
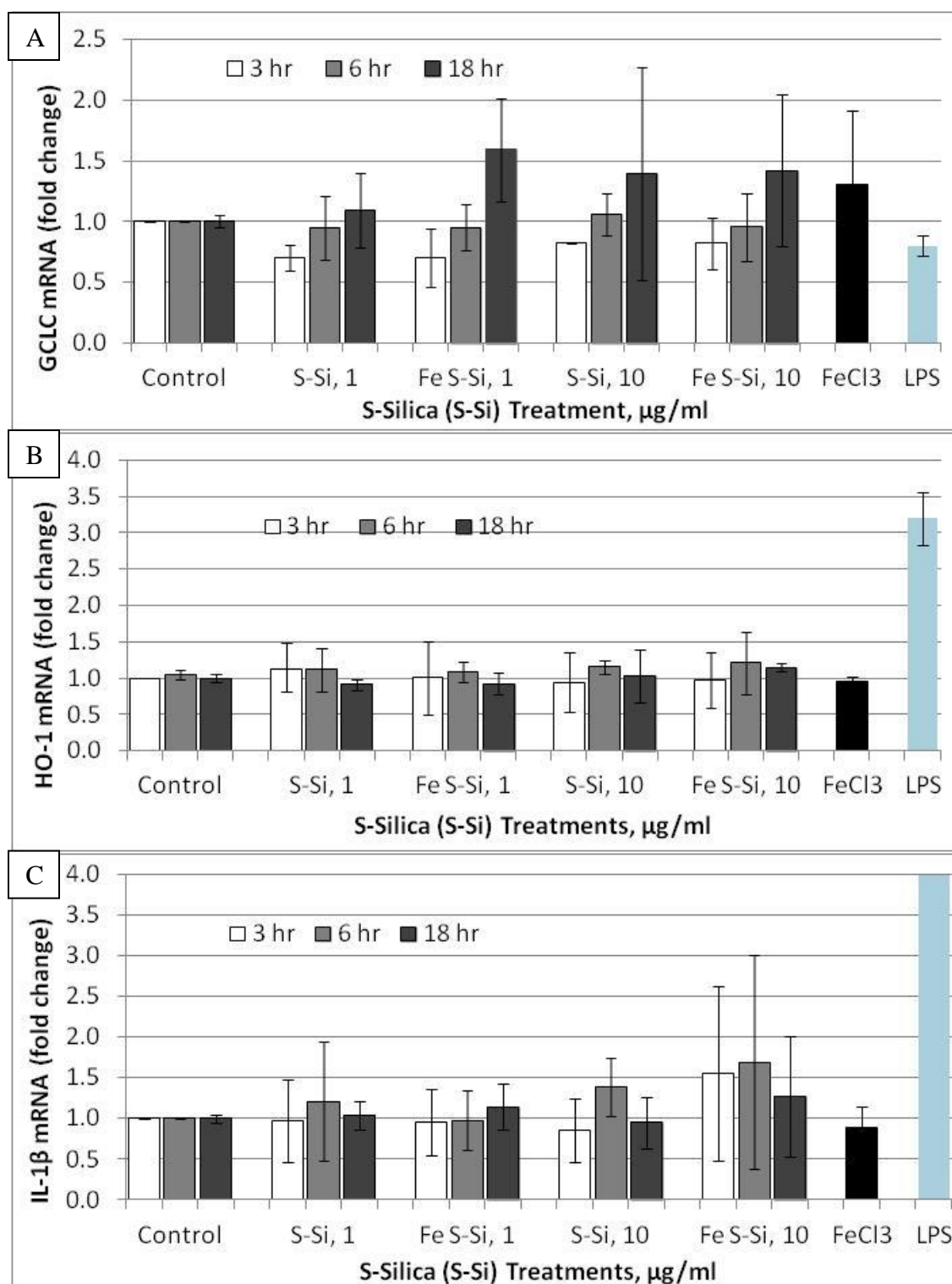
Figure 4.18: Preliminary results for Iron Coated S-Silica and S-Silica for (A) GCLC, (B) HO-1, and (C) IL-1β for 3hr, 6hr, and 18 hr treatments.
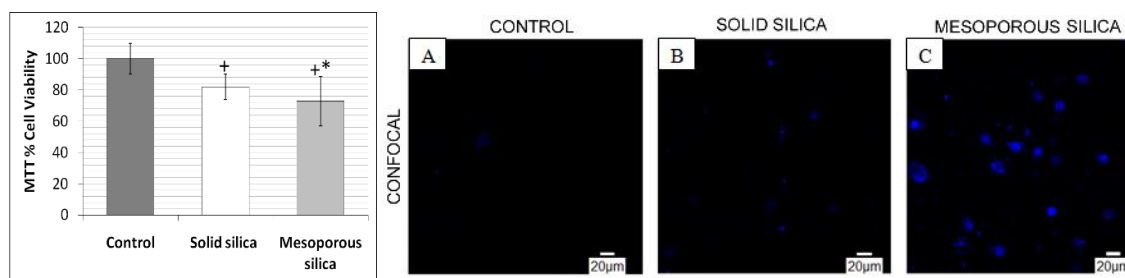
Figure 4.19: MTT Assay of Engineered Solid versus Mesoporous Silica (Left) and Visualization of lipid peroxidation in THP-1 derived macrophages using confocal microscopy (Right). For MTT, both types of silica show reduced viability with respect to the control. Mesoporous silica had a greater reduced viability for mesoporous silica treated cells (100 μg/ml) with respect to solid silica treated cells (82 $\pm$ 8% vs. 73 $\pm$ 16%). Silica particles had minimal interference (One Way Anova & post hoc, P<0.05) [+]*P<0.05 compared to the [+]control and *solid silica. For DPPP, increased fluorescence intensity of oxidized DPPP incorporated into cellular membranes indicates increased membrane lipid peroxidation for cells treated with mesoporous silica particles (C) as compared to the control of untreated cells (A) and cells with solid silica particles (B).
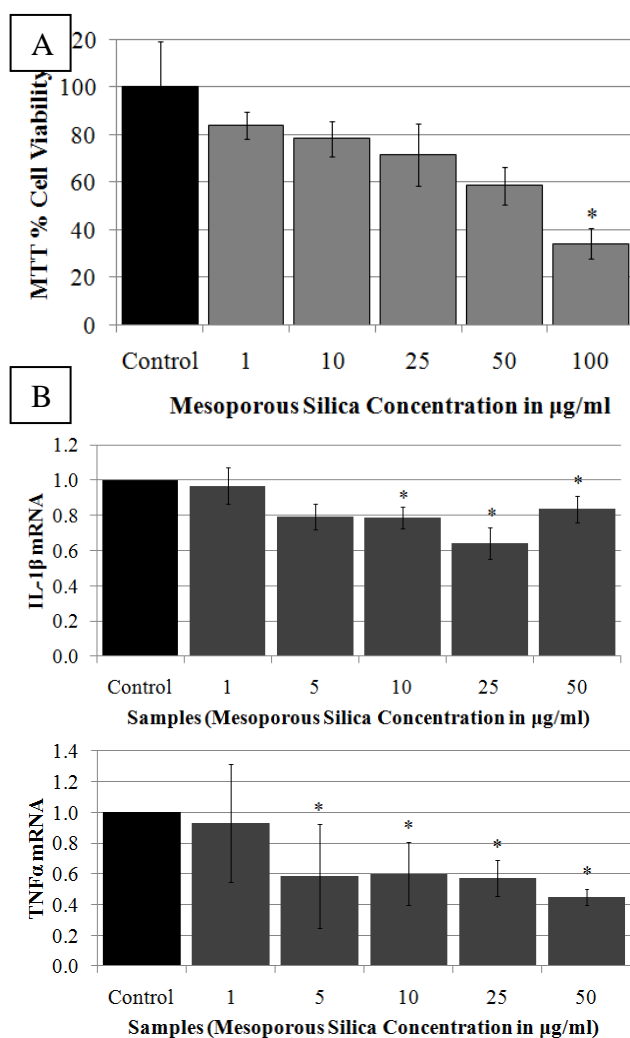
Figure 4.20: Cell viability and mRNA fold change for mesoporous silica (A) the cell viability of the mesoporous silica nanoparticles. At a low cytotoxic dose of 1 μg/ml, there was less cell death. (B) The mRNA concentrations at 1 μg/ml show an average toxicity close to the control, showing low inflammatory mediator production. *P<0.05 for t-test and ANOVA. For the P>0.5, there is no *, meaning these are low doses.
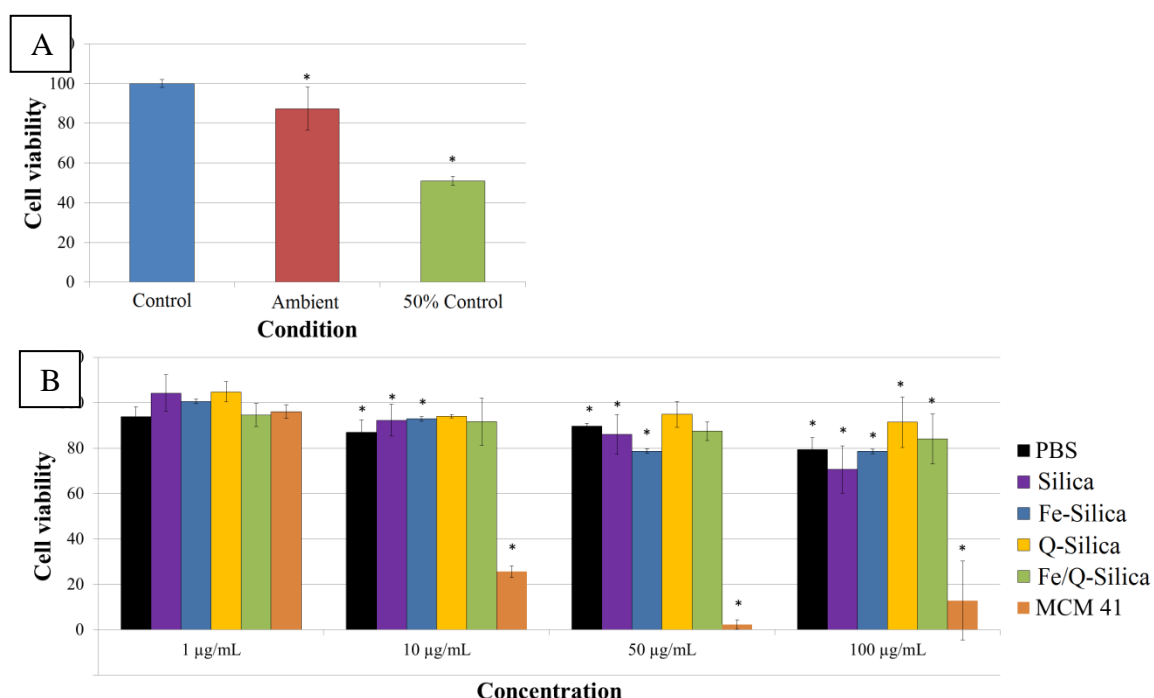
Figure 4.21: Comparison of Cell viability between Silica, Iron Coated Silica, Quinone Coated Silica, Iron-Quinone Coated Silica, and MCM-41 Mesoporous silica. (A) Control, 100 µg/mL of ambient silica, and 50% viability test. (B) Cell viability vs. Particle treatment graph for all conditions and dosages. An asterisk shows statistical difference from control (no particle treatment). 50% control was no particle treatment with half the number of cells seeded relative to control.

CHAPTER 5: Printex 90 as Proxy Carbon-Based Particulate Matter

5.1 Background

A major portion of particulate matter (PM) contains both elemental carbon (EC) and organic carbon (OC) [106]. To portray natural PM, proxy carbon-based PM particles can be used to biologically test the parameters needed to mitigate carbon-based PM, such as soot. Ultrafine black carbon particles can represent the EC content in PM, while quinones can represent the OC content found on its surface, specifically the polycyclic aromatic hydrocarbons (PAHs). Ultrafine particles are more likely to contain trace transition metals, such as iron, and organic carbon, such as PAHs, on their surface compared to coarse and fine PM [138]. Transition metals and PAHs can generate reactive oxygen species that can trigger different biological pathways that may be harmful to human health [138]. Together, black carbon with quinones and iron can mimic natural ultrafine PM.

Black carbon, a component of soot, is a carbonaceous substance identified by both thermal and optical methods. EC, graphitic carbon, soot, and light absorbing carbon are different known names of black carbon. The term black carbon originated from its ability to absorb light at all wavelengths, making it a visibly black substance. OC may also contain elements that absorb solar radiation, and are, therefore, included in the light absorbing carbon group [211]. Hamilton and Mansfield [211] defined black carbon as particulate elemental carbon or graphitic carbon. However, black carbon can mix with some aerosols suspended in the atmosphere [74] and can be coated by other aerosols [73]. Hitzenberger et al. [72] and Reisinger et al. [48] define black carbon as aerosols produced from the incomplete combustion of carbonaceous fuels (biomass, biofuels, and diesel). Other sources define it as the optically active light absorbing particles in soot or smoke [48, 212] or even as soot itself [74, 213]. There is no clear definition of black carbon in the literature, but, in general, it is defined by the atmospheric concern or problem addressed [214]. Since health effects are the priority of this study, black carbon is EC and characterized for its properties.

Black carbon emissions result from a variety of processes. Globally, the sources of black carbon around the world are from biomass burning (35.5%), transportation sources (19%), industrial sources (19.3%) and residential sources (25%) in 2000, according to Lamarque et al. [215]. According to US EPA [216], the black carbon sources in the US were 52% transportation, 35% biomass burning, and the rest were from residential, energy, industry, and others. The prevalent black carbon emission sources vary by location and time of emission, i.e., during the winter, its emissions from wood burning can contribute to ambient concentrations [48].

Printex 90 is an ultrafine black carbon produced by the incomplete combustion of oils [217]. Specifically, Printex 90 (Evonik, Degussa GmbH from Frankfurt, Germany) has been used in several studies either as a particle of interest or reference material comparison [218-221]; and most of these studies involved genotoxicity and inflammatory effects on cells and animals exposed to these particles compared to other nanoparticulate matter. Printex 90 (14 nm) nanoparticles, which are well characterized for their physiochemical properties and serve as a benchmark particle for studying respiratory

effects [222-225], were obtained from Evonik/Degussa. The manufacturer reported a 14 nm particle size with 99% wt. carbon content and 1% wt. other. The 1% has been found by previous researchers to be mainly nitrogen (0.82%) and the rest hydrogen [219]. Jacobsen et al. found that the surface area ranges between 295-338 m^2/g, and the mean particle size in cell media was 98 and 153 nm via dynamic light scattering [219]. A review of carbon blacks found the particle density to range between 1.7-1.9 g/cm^3 [226, 227]. Also, PAHs content was 74.2 ng/g, which is about 3,000 times less than the PAHs content found in diesel exhaust, and total endotoxin was 0.142 EU/mg [228]. The Scientific Committee for Consumer Safety [226] review of carbon blacks reported that the PAHs content of 39 ng/g was studied with Printex 90 in several studies [229-231]. These studies reported a carbon content of 99%.

Many bulk analyses characterize Printex 90 in the literature; therefore, this study focused on characterizing Printex 90 particles on the nano-scale as a model PM particle. As a model PM, biological tests can determine the link of air pollution parameters to health effects. In addition, the proxy PM can be modified, such as coated with iron hydroxide and quinone (a major component in diesel exhaust), to determine the effects of particle coatings on natural PM. This study strived to make a representative model for particulate diesel exhaust with common contaminants on its surface to link the biological effects to the important parameters that adversely affected air pollution. This will assist in making informed mitigation strategies for reducing air pollution and improving respiratory health.

5.2 Characterization

Printex 90 samples, with and without coatings of iron and quinone, were analyzed. The quinone used was 1,4-Naphthoquinone, which is representative of quinones derived from diesel combustion [88]. Iron (III) Chloride was used to coat the Printex 90 samples using a method by Ghio [92] to obtain ferrihydrite on the surface of Printex 90. There were no iron x-ray peaks present in the Printex 90 only and Q-Printex 90 sample (Figure 5.1A). There were characteristic iron X-ray peaks in the Fe-Printex 90 and Fe/Q-Printex 90 (Figure 5.1B-C), indicating that iron was present after coating the particles. When observing the Iron Coated Printex 90 samples in backscatter electron imaging (BSI), where the presence of heavier elements will lead to a brighter image, the image was not evenly bright, suggesting uneven distribution of iron on the surface. Furthermore, trace sulfur was detected via EDX in all of the Printex 90 samples,, which is unsurprising given it is a common contaminant in Printex 90, which is synthesized from the incomplete combustion of oil [227]. For the Iron Coated particles, x-ray peaks for carbon, aluminum, iron, chloride, and oxygen were present. The carbon signal was from Printex 90 and from the carbon tape. Aluminum and oxygen signals are from the aluminum stub used to hold the sample. Particles aggregated in SEM. In addition, for different spot scans of the sample, EDX revealed that iron and chloride ions in iron (III) chloride did not always co-localize, meaning that in addition to some ferrihydrite being formed, iron (III) chloride was also present on the surface of Printex 90.

In Figure 5.2, the TEM was used to test for beam damage by focusing the beam on the same section of the sample before and after beam damage. No visible damage or necking of the sample occurred with Printex 90 after beam damage. In Figure 5.3, iron

particles are present with the Fe-Printex 90 sample (Figure 5.3 B); however, these iron particles were not everywhere (Figure 5.3A). The iron particles coated unevenly due to the sheer volume of Printex 90 compared to iron. (Due to the lower density of Printex 90 compared to silica, equivalent mass doses of iron resulted in much lower surface doses of iron on the Printex 90 compared to silica.)

In Figure 5.4, the diffraction pattern of Fe-Printex 90 samples revealed the presence of a crystalline structure, and the Fe-Printex 90 and Fe/Q-Printex 90 samples were observed to have similar diffraction patterns. D-spacings measured from the diffraction patterns most closely matched iron oxide hydroxide (JCPDF: 00-026-0792). However, further study is needed to verify this due to the small number of diffraction rings that could be observed, measurement uncertainty and the similar d-spacing values of various iron-containing phases. In Figure 5.5A, it was difficult to determine the carbon signal relative to the background signal (holey carbon) based on the EELS spectra. Both signals appeared to be similar for carbon. EELS detected iron for Fe-Printex 90 (Figure 5.5B) based on the presence of the iron L_3 and L_2 peaks. The detection of oxygen suggested the presence of ferrihydrite, as was observed for iron coated silica (Chapter 4).

For Quinone Coated Printex 90, as shown in Figure 5.6, it was not possible to visually confirm the presence of quinone in precipitated form (Figure 5.7 shows aggregates of precipitated quinone for comparison). Smaller precipitates or unaggregated quinone would be difficult to detect visually. In Figure 5.8 the STXM carbon signal of Printex 90 and quinone are shown. The two signals are different from each other and are distinguishable by their X-Ray Absorption spectra, which should make detection of quinone on Printex 90 via STXM possible in future experiments.

In Figure 5.10 for Fe/Q-Printex 90, some regions show visible quinone precipitates and iron particles. The Iron/Quinone Coated Printex 90 (Fe/Q-Printex 90 in Figure 5.9) aggregated, making it sometimes difficult to distinguish between iron/quinone and Printex 90. Based on these results, it can be inferred that the quinone deposition discussed in the preceding paragraph was successful, although it could not be verified through TEM or STXM. The EELS peaks for Iron coated Fe/Q-Printex 90 were similar to the iron EELS peaks found in Fe-Printex 90 (Figure 5.11). This showed that the iron coating protocol for Iron and Iron/Quinone Coated Printex 90 produced similar results. Figure 5.12 showed the diffraction pattern for Fe/Q-Printex 90, indicating the likely presence of an iron oxide hydroxide. The STXM and EELS data confirmed the presence of iron on the Printex 90.

5.2 Preliminary Biological Response

In previous studies in the literature, carbon black (50nm and 500nm) particles were tested with THP-1 cells and showed differences in cytotoxicity, inflammatory mediator production, and phagocytosis activity [217]. In this study, Figure 5.13 showed the mRNA fold change for increased concentrations of Printex 90 for GCLC, HO-1, and IL-1β on THP-1 human monocyte-derived macrophages. There were no changes compared to the control (GAPDH) for GCLC at higher concentrations with or without a quinone coating, which could have been attributed to lower surface dose with quinones.

The HO-1 signal increased with increased IL-1β mRNA fold change, which was predicted since IL-1β could induce HO-1 expression [232].

5.3 Evaluation of Proxy Carbon-Based Particulate Matter Particles

The Printex 90 particles were not ideal proxy carbon based PM particles. Although the method by Ghio et al. [92] was able to coat some iron hydroxide on Printex 90, it was not uniformly coated as seen in the TEM images (Figure 5.3). In the quinone coating case, it was difficult to assess with TEM (Figure 5.6) if quinone was present.

Printex 90 are 14 nm particles, with a density of 1.8 g/cm^3 and surface area of about 300 m^2/g [227]. Compared to the previously studied ~50 nm silica (Chapter 4), the silica density is typically around 2.2 g/cm^3 [233-235] and surface area around 60 m^2/g. Based on density alone, the volume of Printex 90 was 20% more than silica at the same mass. Based on surface area, Printex 90 had 5 times more surface area than silica. Furthermore, since the particle size between silica and carbon are different, the number of particles per mass concentration is also different. Accounting for these parameters, the true volume of Printex 90 was much more than the volume of silica at the same mass (visually, the volume was at least more than double). This means that evenly coating the particles requires a greater concentration of iron and quinones compared to the case with silica. The concentration should also match natural PM concentrations. For example, concentrations of PAHs in urban settings can range up to 30-50 µg/g with some extreme cases up to 230 µg/g [236]. The concentration of quinone used in this experiment was 32 µg/g.

Alternatively, the size of the carbon-based proxy PM can be increased to reduce the amount of surface area to coat. In the literature, soot can range from 20 nm to 200 nm [237-239], so Printex 90 is on the lower end of part of the spectrum. Larger sized black carbon, such as Printex G, which is 50 nm, can be used instead of Printex 90 [227]. This will also make it comparable in size to the silica particles. Visually, it would also be easier to distinguish the iron and quinone coating on a larger particle. In addition, larger particles will be less likely to aggregate, since there is less surface area attraction.

In addition, other coating protocols with different types of iron hydroxides, such as goethite and schwertmannite, can be used to coat the surface of the proxy PM particles [205, 206]; and other quinone coating protocols can also be investigated [240, 241]. Other PAHs can coat Printex 90, as well. Printex 90 naturally has Naphthalene, a PAH which consists of two fused benzene rings, on its surface and can be washed off with organics or volatilized by heating up to 950°C [227]. Cleaning the surface of Printex 90 may also allow more quinone or iron to adhere to its pristine surface.

The carbon-based proxy PM can also be improved by removing the surface sulfur contamination, which is present on all black carbon synthesis [227]. The oily residue can also be removed. Onoda et al. [218] cleaned their Printex 90 before exposure to cells by sonication in water for 30 minutes and filtering in a 450 nm filter. Another issue was the hydrophobic nature of Printex 90, which made it difficult to disperse the particles for cell treatment. The low density and high surface area of Printex 90 prevented the particles from dispersing and settling down when added to cell media. Particles can alternatively be dispersed in bronchoalveolar lavage fluid (BALF) and PBS containing dipalmitoyl phosphatidylcholine (DPPC), a pulmonary surfactant, or mouse serum albumin before

being added to cells for better dispersion [242]. With a larger particle size, the carbon-based proxy PM particles may settle down on the surface of the cells for biological interactions to occur. Alternatively, carbon coated silica particles can be synthesized to represent carbon-based proxy PM [243-245]. The silica will provide more density for the particles to settle down while externally appearing to be carbon. Then, along with biological tests, the carbon-based proxy PM model can determine the important parameters for mitigation of air pollution and the reduction of health risks.

5.4 Conclusions

Printex 90 was not the ideal PM particle proxy. Unfortunately, the Printex 90 (14 nm) may have been too small and the surface area was too large for iron hydroxide and quinone to evenly coat. Furthermore, the quinone coating on Printex 90 was difficult to verify, since they were not uniformly coated on Printex 90. There was no difference in cytokine production with or without a Quinone coating, which means that either quinones did not have a response or not enough Quinone was present. The iron coatings (with and without Quinones) on the Printex 90 particles were not uniform or evenly dispersed due to the high surface area of Printex 90. However, this study was able to confirm that coating ferrihydrite on the surface of Printex 90 was successful and the presence of ferrihydrite on the surface produced an increase in IL-1β and HO-1 response. A higher concentration of iron can be used for future experiments for a more uniform coating. In addition, the presence of a surface oil residue prevent continuation of the Printex 90 biological experiments. In future studies, larger and cleaner carbon black particles can model as proxy PM particles.

5.5 Figures and Figure Legends

|	Fe (mmol/g) average	St.dev
Printex 90 (P90)	0.18	0.23
P90 dried + 5ml cell media	0.12	0.11
1 mg/ml P90 + 5x10^{-5} M Fe	2.31	0.68
1mg/ml P90 + 5x10^{-6} M Fe	0.14	0.04
1mg/ml P90 + 5x10^{-5} M Fe + 0.2 mM Q	0.48	0.08
1mg/ml P90 + 5x10^{-5} M Fe + 2 mM Q	1.21	0.02
1mg/ml P90 + 5x10^{-6} M Fe + 0.2 mM Q	0.28	0.04
1mg/ml P90 + 5x10^{-6} M Fe + 2 mM Q	0.12	0.03

Table 5.1: ICP-MS Data. Final concentrations of iron coating of samples with their iron concentration detected in ICP-MS. Q = Quinone. P90 = Printex 90.
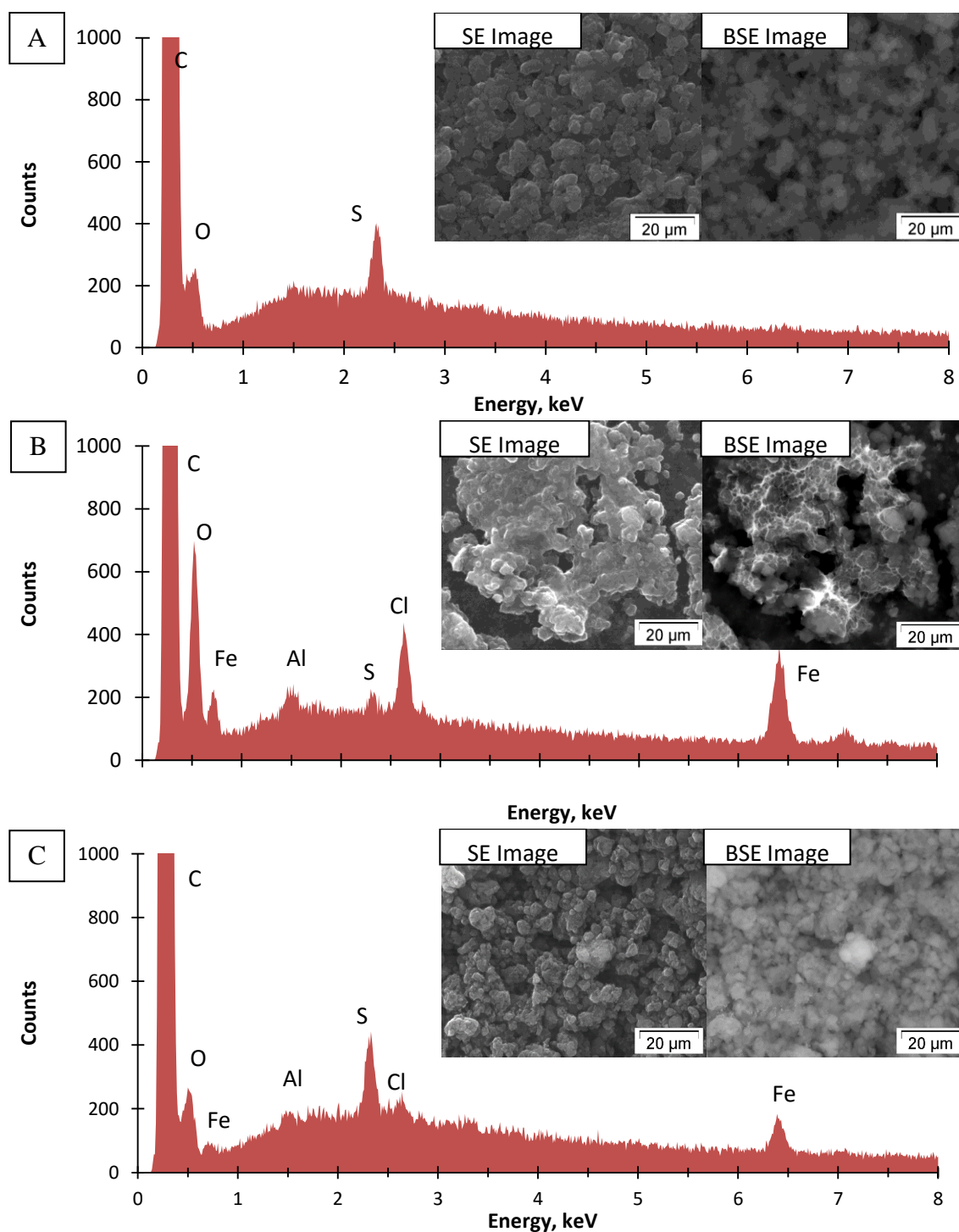
Figure 5.1: Representative EDX spectrum of (A) Printex 90 and Quinone Coated Printex 90 (B) Iron Coated Printex 90 (Fe-Printex 90) and (C) Iron/Quinone Coated Printex 90 (Fe/Q-Printex 90). Inset images show SE and BSE images of scanned area.
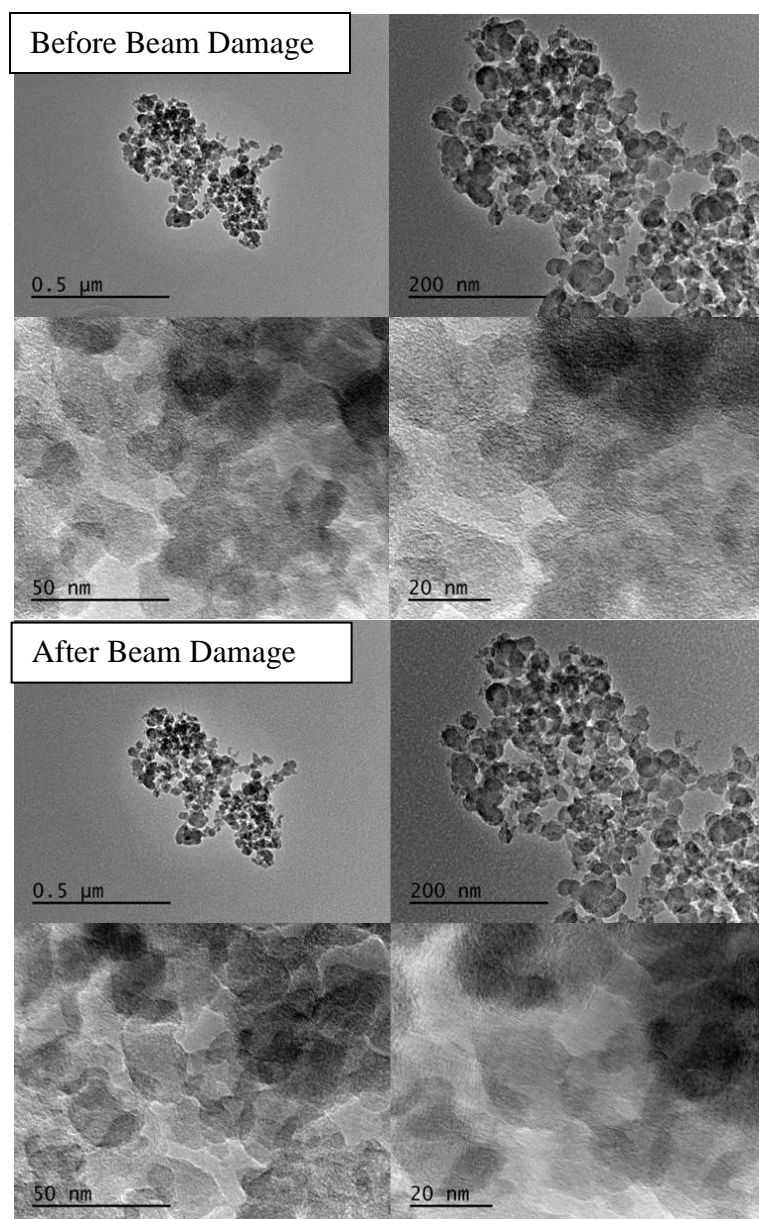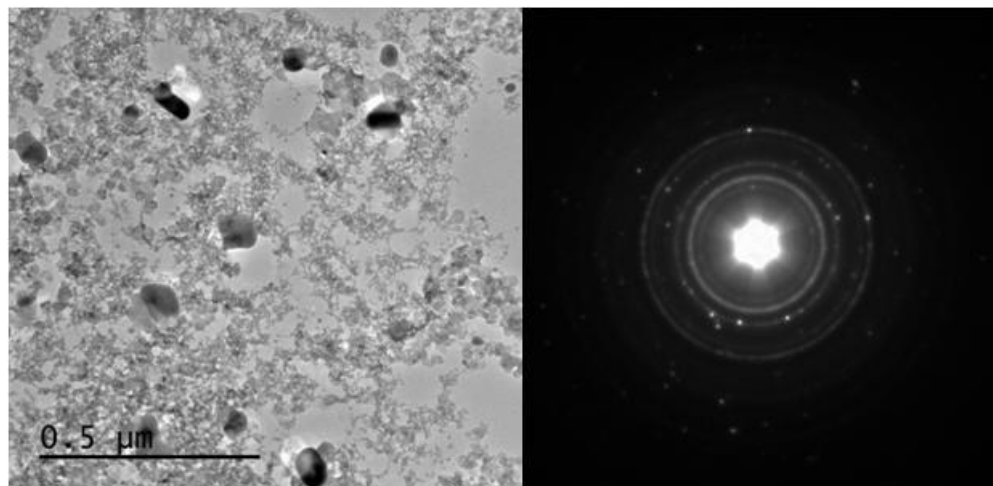
Figure 5.2: TEM images of Printex only at different magnifications with and without beam damage. No beam damage appears to occur with beam radiation.
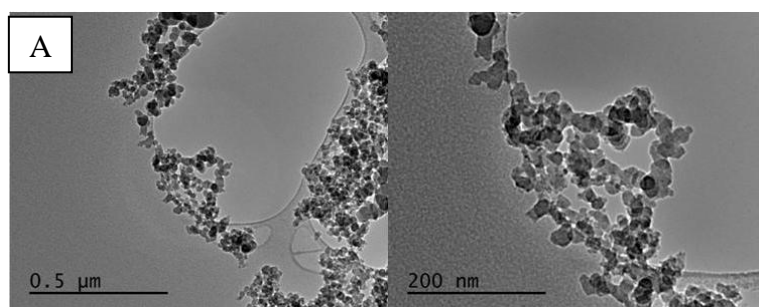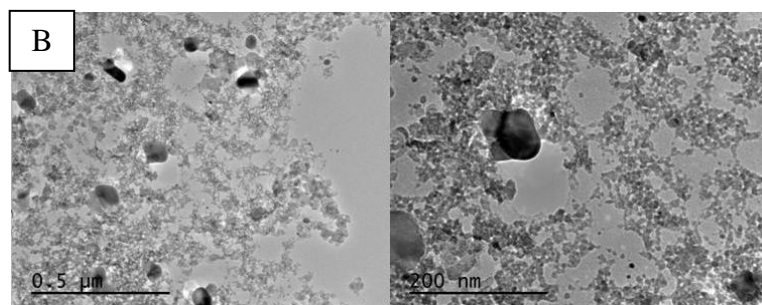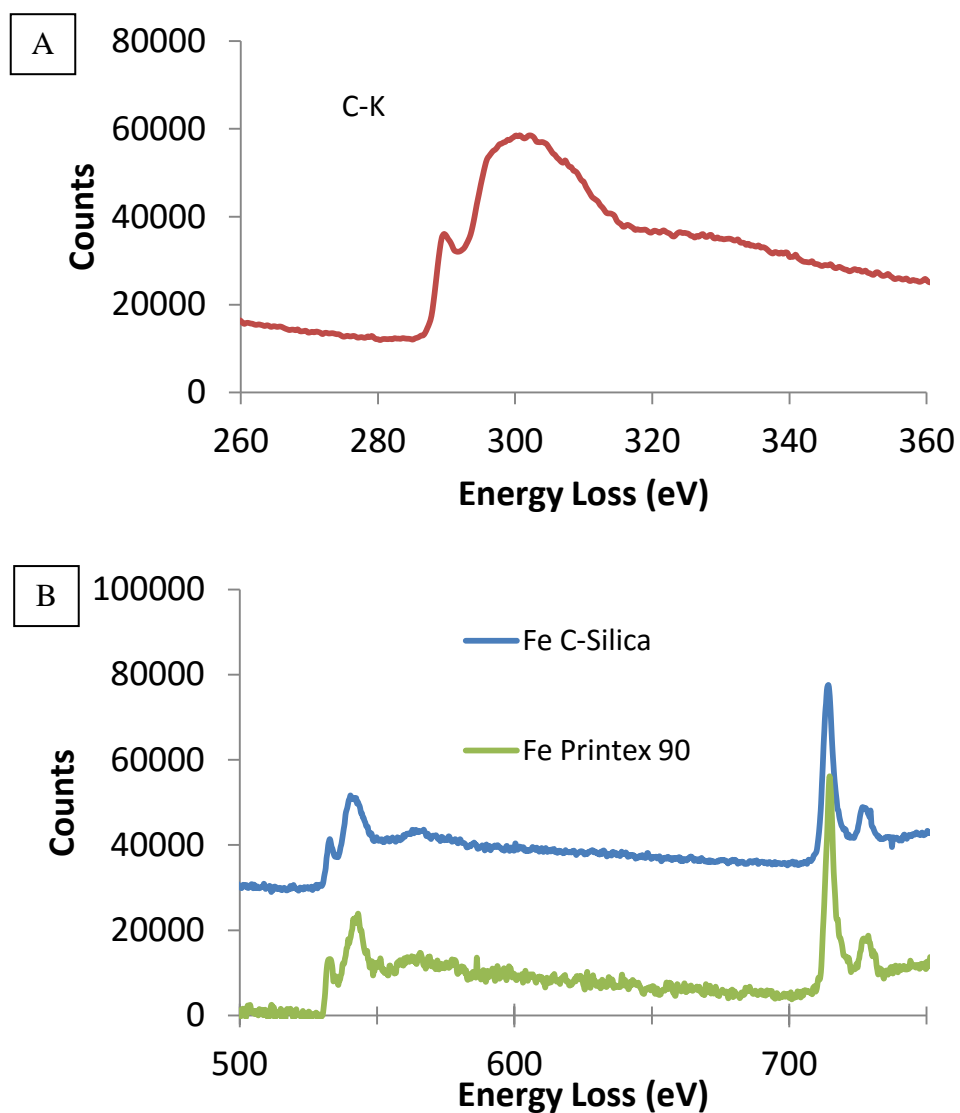
Figure 5.3: Fe-Printex 90 regions (A) without Iron and (B) regions with iron.

Figure 5.4: TEM image with Diffraction Pattern of Fe-Printex 90.

Figure 5.5: Fe-Printex 90. (A) Carbon and (B) Iron signal detected with EELS
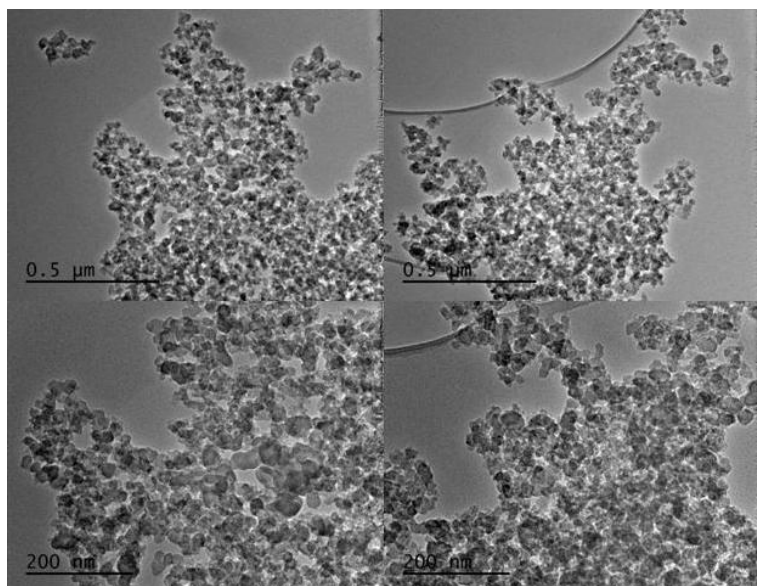
Figure 5.6: TEM Images of Q-Printex 90 at various magnifications.
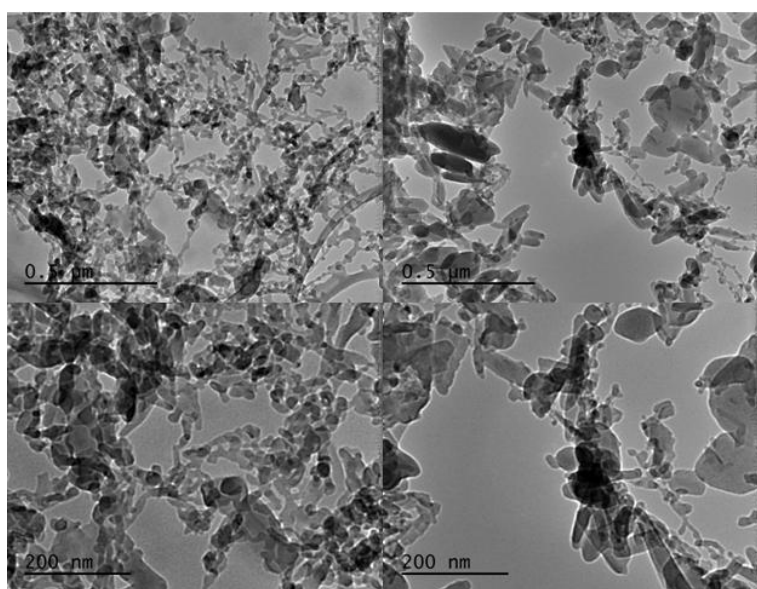
Figure 5.7: TEM images of Quinones only (1, 4 Naphthoquinone).
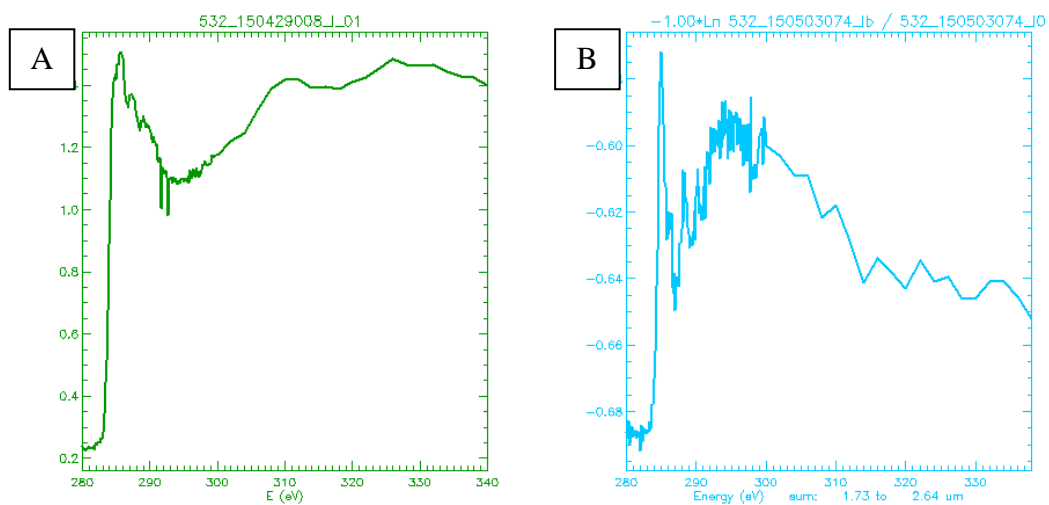
Figure 5.8: STXM of (A) Printex 90 only vs. (B) Quinone only signal
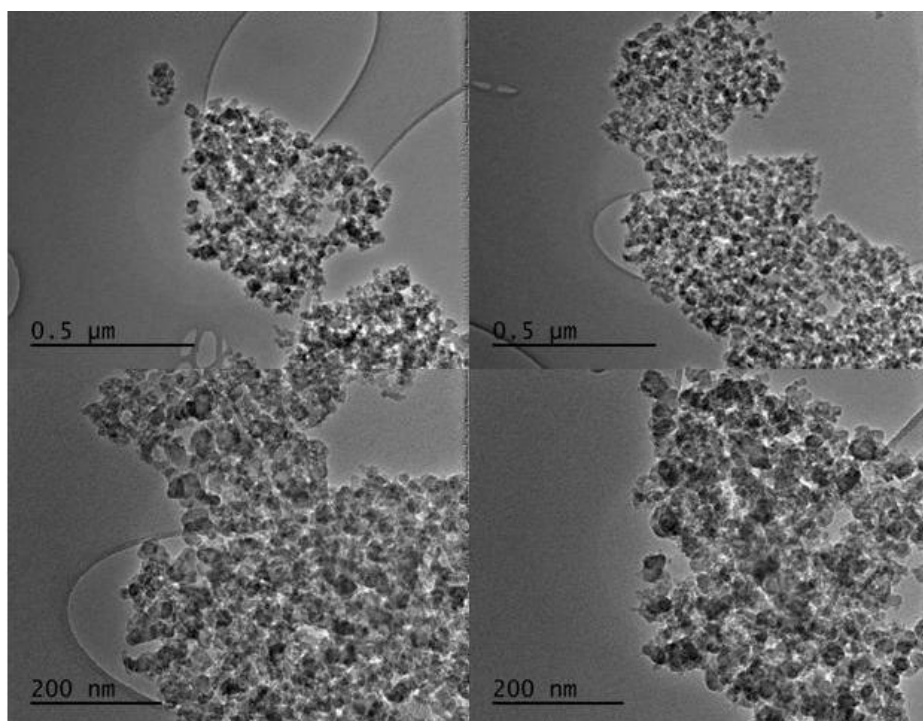
Figure 5.9: TEM images of Fe/Q-Printex 90 at various magnifications.
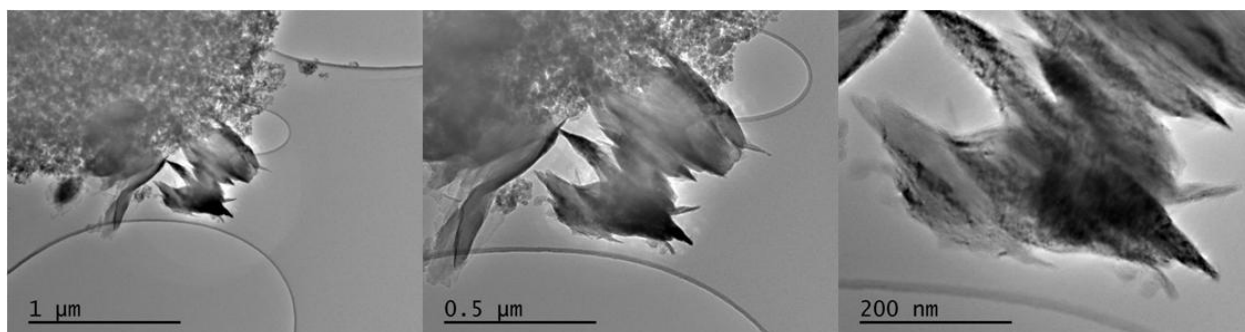
Figure 5.10: TEM images of Fe/Q-Printex 90 for a region where iron and quinone precipitates appear to both be present.
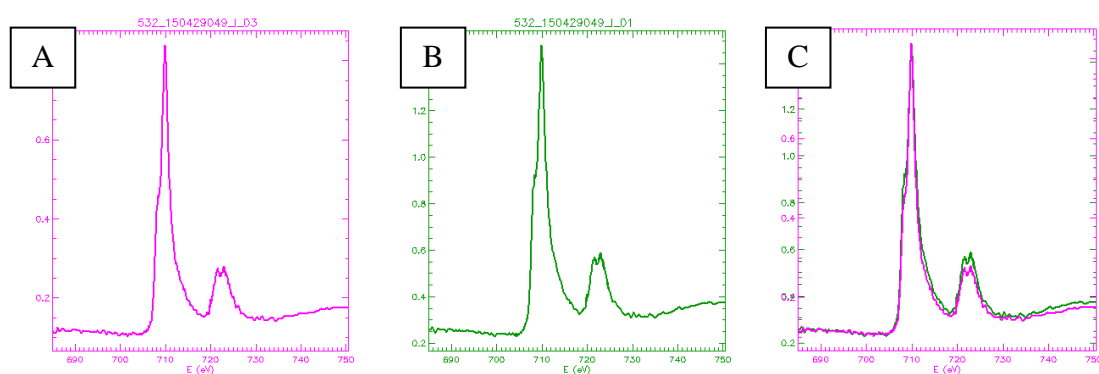
Figure 5.11: Comparison of the STXM iron signals between (A) Fe-Printex 90 and (B) Fe/Q-Printex 90. (C) Overlay of spectrums A and B.
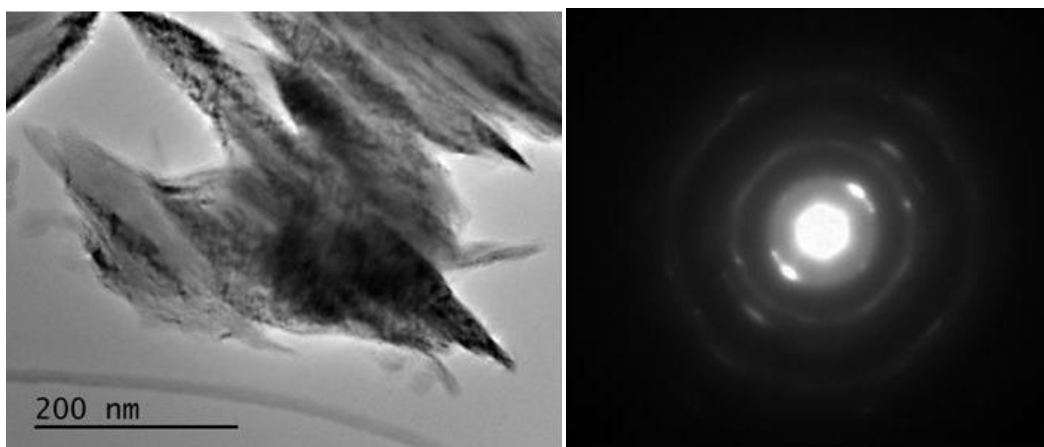
Figure 5.12: TEM image and Selected Area Diffraction for Fe/Q-Printex 90.
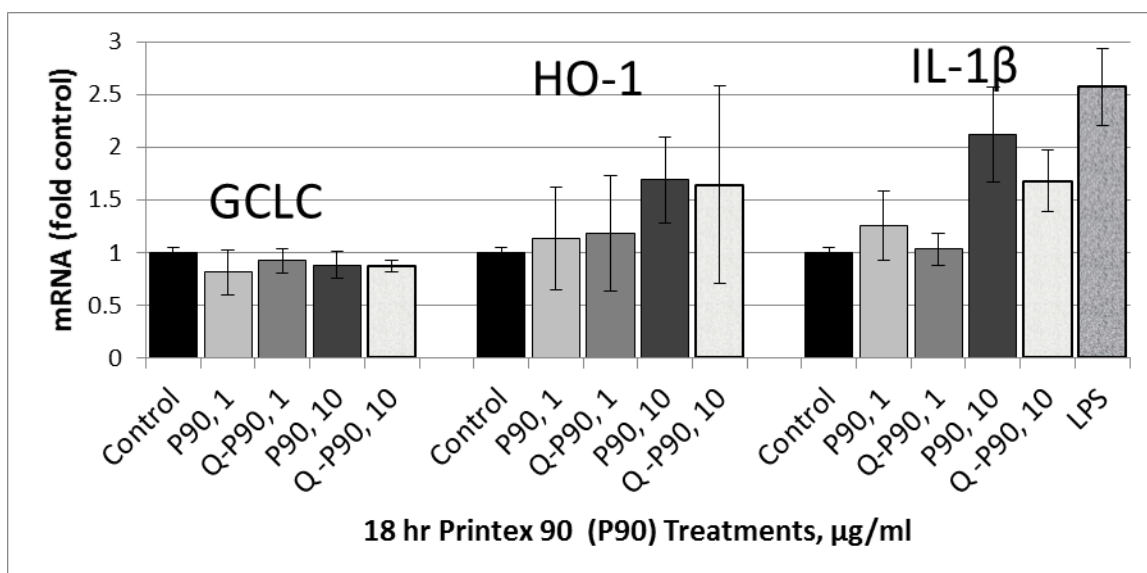
Figure 5.13: Biological response of Printex 90 and Q-Printex 90.

CHAPTER 6: Conclusions and Future Directions

Determining the effect of particle size, morphology, and chemical composition on health risks is important for mitigation efforts to improve respiratory health. Chemical speciation is important for identifying the parameters in air pollution we need to focus on for mitigation to obtain the most health benefits. Awareness of what specifically harms public health will allow us to make informed decisions on what chemical, agricultural, or industrial processes we should focus on to reduce the air pollution.

Here we analyzed natural PM and determined the parameters needed to make a proxy PM particle for biological testing for health risk assessment. The main components of the particulate matter in the SJV were aluminosilicates (40 to 50 nm) with ferrihydrite on its surface. In addition, these natural PM contained elemental carbon and organic carbon, so a carbon-based proxy PM can also model natural PM. We also analyzed the emissions from an automobile shredding plant and found iron oxide fine particulate matter to be a common pollutant, supporting the relevance of iron in proxy particulate systems.

A silica proxy PM particle was developed to mimic the naturally occuring aluminosilicates, while carbon black (Printex 90) was used to represent soot and elemental carbon pollution. Natural PM contains metals and organic carbon on its surface; therefore, in this experiment, iron represented the metal contaminants, and quinones represented organic carbon, such as PAHs, on the surface of the proxy PM particles. These particles were synthesized/purchased and then were modified to model the naturally occurring PM. Their properties were verified with materials characterization and chemical speciation. In addition, mesoporous silica tested for the effect of surface area and mass dose on toxicity. Ferrihydrite was successfully added onto the surface of the particles.

From the silica model, we showed that the surface coating affects the cytotoxicity of the silica nanoparticles. Quinone coating on silica reduced cell death, while an iron hydroxide coating increased cell death relative to silica alone. However, mesoporous silica at the same mass dose drastically increased cell death. This showed that mitigation of high surface area pollutants might be more beneficial in air pollution mitigation per mass dose compared to reductions in surface contaminant sources. For the future, other types of quinones and surface contaminants, based on ambient air pollution parameters, can coat on silica to determine the potential health risks through biological experiments, such as lead and zinc found in the automobile shredder plant. In future work, the proxy PM can be tested for other biological mechanisms and different iron oxides can be coated on its surface. In addition, an aluminosilicate proxy PM particle can replace the silica model with the development of new methods to synthesize aluminosilicate nanoparticles [134, 208, 209]. This may provide a novel proxy PM for nanoparticle aluminosilicates. The surface of the aluminosilicates may have different affinities for iron or quinones compared to silica. New experiments can determine this. For example, different concentrations of iron can coat the surface of the particles for comparison with silica.

For the carbon model using Printex 90, iron, quinones, and both coated the particles. However, the Printex 90 particles were not an ideal simple model. The particles were too small to allow coating with the quinones and iron particles due to greater surface area compared to the silica model. A uniform coated requires a higher

 concentration of iron and quinone to match the surface area of Printex 90. Furthermore, the lack of availability of Printex 90 (no longer commercially available) will make it an issue for future studies.

In future work, analysis of SJV samples from different locations during at various time points throughout the year can be used improve the model SJV PM. These may help set different policies for each regions during different times of the year for the best mitigation strategies for reducing air pollution health related risks. Specific sampling locations near major sources of air pollution can also be analyzed, similar to the case with the automobile shredder plant. In addition, chemical speciation of the SJV samples can test the effects of mitigations efforts over time to see if there are any changes to its physical and chemical properties as evidence.

REFERENCES

[1]   M. V. Mateos, G. A. Salvador, and N. M. Giusto, "Selective localization of phosphatidylcholine-derived signaling in detergent-resistant membranes from synaptic endings," *Biochim Biophys Acta,* vol. 1798, pp. 624-36, Mar 2010.

[2]   R. B. Everett, J. Capitman, S. Wolff, S. Sedlock, N. Burke, V. LaFronza, Smedley, F. Eaves, C. Gullatt, and M. Wenger, "Place Matters For Health in the San Joaquin Valley: Ensuring Opportunities for Good Health for All - A report on Health Inequalities in the San Joaquin Valley," Joint Center for Political and Economic Studies, San Joaquin Valley Place Matters Team, Center on Human Needs Virginia Commonwealth University, and Virginia Network for Geospatial Health Research2012.

[3]   AmericanLungAssociation. (2015). *State of the Air*. Available: http://www.stateoftheair.org/2015/assets/ALA_State_of_the_Air_2015.pdf

[4]   S. Sadredin, "Item Number 8: Consider the Need and Options for Rebranding the District's Risk-Based Strategy," pp. Available at: http://www.valleyair.org/Board_meetings/GB/agenda_minutes/Agenda/2013/May/StudySession/i8-FinalGBItemRebrandRiskBasedStrategy.pdf, 2013.

[5]   SJVAPCD, "Annual Report 2013-2014: Report to the Community," pp. http://www.valleyair.org/2013-14-annualreport.pdf, 2014.

[6]   A. Kot and J. Namiesńik, "The role of speciation in analytical chemistry," *TrAC Trends in Analytical Chemistry,* vol. 19, pp. 69-79, 2000.

[7]   U.S.EPA, "Air Quality Criteria for Particulate Matter," vol. Available at http://cfpub2.epa.gov/ncea/cfm/recordisplay.cfm?deid=87903., 2004.

[8]   SJVAPCD, "Annual Report 2012-2013: Report to the Community," pp. Available at: http://www.valleyair.org/2012-13annualreport.pdf, 2013.

[9]   J. N. Gangwar, T. Gupta, and A. K. Agarwal, "Composition and comparative toxicity of particulate matter emitted from a diesel and biodiesel fuelled CRDI engine," *Atmospheric Environment,* vol. 46, pp. 472-481, 2012.

[10]   K. Donaldson, V. Stone, A. Clouter, L. Renwick, and W. MacNee, "Ultrafine particles," *Occupational and Environmental Medicine,* vol. 58, pp. 211-216, March 1, 2001 2001.

[11]   U.S.EPA, "Final Report: Integrated Science Assessment for Particulate Matter," U.S. Environmental Protection Agency, Washington, DC2009.

[12]   E. Jimenez, C. Linares, D. Martinez, and J. Diaz, "Role of Saharan dust in the relationship between particulate matter and short-term daily mortality among the elderly in Madrid (Spain)," *Science of the Total Environment,* vol. 408, pp. 5729-36, Nov 1 2010.

[13]   Z. Qian, Q. He, H. M. Lin, L. Kong, D. Zhou, S. Liang, Z. Zhu, D. Liao, W. Liu, C. M. Bentley, J. Dan, B. Wang, N. Yang, S. Xu, J. Gong, H. Wei, H. Sun, Z. Qin, and H. E. I. H. R. Committee, "Part 2. Association of daily mortality with ambient air pollution, and effect modification by extremely high temperature in Wuhan, China," *Research Report / Health Effects Institute,* pp. 91-217, Nov 2010.

[14]   G. J. Prescott, G. R. Cohen, R. A. Elton, F. G. Fowkes, and R. M. Agius, "Urban air pollution and cardiopulmonary ill health: a 14.5 year time series study," *Occupational and Environmental Medicine,* vol. 55, pp. 697-704, Oct 1998.

[15]   J. Schwartz, "Air pollution and hospital admissions for respiratory disease," *Epidemiology,* vol. 7, pp. 20-8, Jan 1996.

[16]   P. Zimniak, "Detoxification reactions: relevance to aging," *Ageing Res Rev,* vol. 7, pp. 281-300, Dec 2008.

[17]   A. E. Nel, D. Diaz-Sanchez, D. Ng, T. Hiura, and A. Saxon, "Enhancement of allergic inflammation by the interaction between diesel exhaust particles and the immune system," *Journal of Allergy and Clinical Immunology,* vol. 102, pp. 539-554, 1998.

[18]   A. Chambellan, Crestani, B., Soler, P., Moreau, J., Aubier, M., "Diesel particles and allergy: cellular mechanisms," *Allerg Immunol (Paris),* vol. 32, pp. 43-48, 2000.

[19]   N. Li, C. Sioutas, A. Cho, D. Schmitz, C. Misra, and J. Sempf, "Ultrafine particulate pollutants induce oxidative stress and mitochondrial damage," *Environ Health Perspect,* vol. 111, pp. 455 - 460, 2003.

[20]   P. Borm, D. Robbins, S. Haubold, T. Kuhlbusch, H. Fissan, K. Donaldson, R. Schins, V. Stone, W. Kreyling, J. Lademann, J. Krutmann, D. Warheit, and E. Oberdorster, "The potential risks of nanomaterials: a review carried out for ECETOC," *Particle and Fibre Toxicology,* vol. 3, p. 11, 2006.

[21]   N. Li, M. Hao, R. F. Phalen, W. C. Hinds, and A. E. Nel, "Particulate air pollutants and asthma: A paradigm for the role of oxidative stress in PM-induced adverse health effects," *Clinical Immunology,* vol. 109, pp. 250-265, 2003.

[22]   K. Donaldson, D. Brown, A. Clouter, R. Duffin, W. MacNee, and L. Renwick, "The pulmonary toxicology of ultrafine particles," *J Aerosol Med,* vol. 15, pp. 213 - 220, 2002.

[23]   C. A. Pope III, R. T. Burnett, M. J. Thun, E. E. Calle, D. Krewski, K. Ito, and G. D. Thurston, "Lung Cancer, Cardiopulmonary Mortality, and Long-term Exposure to Fine Particulate Air Pollution," *JAMA,* vol. 287, pp. 1132-1141, March 6, 2002 2002.

[24]   M. S. O'Neill, A. Veves, A. Zanobetti, J. A. Sarnat, D. R. Gold, P. A. Economides, E. S. Horton, and J. Schwartz, "Diabetes Enhances Vulnerability to Particulate Air Pollution–Associated Impairment in Vascular Reactivity and Endothelial Function," *Circulation,* vol. 111, pp. 2913-2920, June 7, 2005 2005.

[25]   A. Zanobetti and J. Schwartz, "Are Diabetics More Susceptible to the Health Effects of Airborne Particles?," *American Journal of Respiratory and Critical Care Medicine,* vol. 164, pp. 831-833, 2001/09/01 2001.

[26]   C. A. Pope and D. W. Dockery, "Health Effects of Fine Particulate Air Pollution: Lines that Connect," *Journal of the Air & Waste Management Association,* vol. 56, pp. 709-742, 2006/06/01 2006.

[27]   E. I. Thaller, S. A. Petronella, D. Hochman, S. Howard, R. S. Chhikara, and E. G. Brooks, "Moderate Increases in Ambient PM2.5 and Ozone Are Associated With Lung Function Decreases in Beach Lifeguards," *Journal of Occupational and Environmental Medicine,* vol. 50, pp. 202-211, 2008.

[28]   A. Zanobetti, J. Schwartz, E. Samoli, A. Gryparis, G. Touloumi, J. Peacock, R. H. Anderson, A. Le Tertre, J. Bobros, M. Celko, A. Goren, B. Forsberg, P. Michelozzi, D. Rabczenko, S. P. Hoyos, H. E. Wichmann, and K. Katsouyanni, "The temporal pattern of respiratory and heart disease mortality in response to air pollution," *Environmental Health Perspectives,* vol. 111, pp. 1188-1193, 2003.

[29]   F. Dominici, A. McDermott, S. L. Zeger, and J. M. Samet, "Airborne Particulate Matter and Mortality: Timescale Effects in Four US Cities," *Am J Epidemiol,* vol. 157, pp. 1055-1065, June 15, 2003 2003.

[30]   C. A. Pope, "Epidemiology of fine particulate air pollution and human health: biologic mechanisms and who's at risk?," *Environmental Health Perspectives,* vol. 108, pp. 713-723, 2000.

[31]   C. A. Pope, M. Ezzati, and D. W. Dockery, "Fine-Particulate Air Pollution and Life Expectancy in the United States," *New England Journal of Medicine,* vol. 360, pp. 376-386, 2009.

[32]   A. W. Correia, C. A. Pope, D. W. Dockery, Y. Wang, M. Ezzati, and F. Dominici, "The Effect of Air Pollution Control on Life Expectancy in the United States: An Analysis of 545 US counties for the period 2000 to 2007," *Epidemiology,* vol. 24, pp. 23-31, 2013.

[33]   I. C. Pope, R. T. Burnett, M. J. Thun, and et al., "Lung cancer, cardiopulmonary mortality, and long-term exposure to fine particulate air pollution," *JAMA,* vol. 287, pp. 1132-1141, 2002.

[34]   U.S.EPA, "National Ambient Air Quality Standards (NAAQS)," p. Available at: http://www3.epa.gov/ttn/naaqs/criteria.html, 2016.

[35]   Y. Zhou, J. S. Fu, G. Zhuang, and J. I. Levy, "Risk-Based Prioritization among Air Pollution Control Strategies in the Yangtze River Delta, China," *Environmental Health Perspectives,* vol. 118, pp. 1204-1210, 2010.

[36]   A. Lacey, "Early Data Could Spur Push For EPA to Adopt Risk-Based PM Air Standard," *Inside EPA's Clean Air Report: An exclusive biweekly report on the Clean Air Act and U.S. air policy,* vol. 23, pp. 1,3-4., 2012.

[37]   D. Lighthall and J. Capitman, "The Long Road to Clean Air in the San Joaquin Valley: Facing the Challenge of Public Engagement," California State University, Fresno, Fresno, CA2007.

[38]   SJVAPCD. Web-based Archived Air Quality (WAAQ) System [Online].

[39]   D. Bulwa, "Firefighters battling hundreds of blazes," in *SFGate*, ed. San Francisco, CA, 2008.

[40]   CARB, "Almanac Emission Projection Data: 2015 Estimated Annual Average Emissions San Joaquin Valley Air Basin," p. Available at: http://www.arb.ca.gov/app/emsinv/2013/emssumcat.php, 2013.

[41]   J. C. Chow, J. G. Watson, L. L. Ashbaugh, and K. L. Magliano, "Similarities and differences in PM10 chemical source profiles for geological dust from the San Joaquin Valley, California," *Atmos Environ,* vol. 37, pp. 1317-1340, Mar 2003.

[42]   W. F. Rogge, P. M. Medeiros, and B. R. T. Simoneit, "Organic Compounds in Dust from Rural and Urban Paved and Unpaved Roads Taken During the San Joaquin Valley Fugitive Dust Characterization Study," *Environmental Engineering Science,* vol. 29, pp. 1-13, Jan 2012.

[43] J. Jasinski, K. E. Pinkerton, I. M. Kennedy, and V. J. Leppert, "Spatially resolved energy electron loss spectroscopy studies of iron oxide nanoparticles," *Microsc Microanal,* vol. 12, pp. 424-31, 2006.

[44] T. C. Bond, D. G. Streets, K. F. Yarber, S. M. Nelson, Jung-Hun Woo, and Z. Klimont, "A technology-based global inventory of black and organic carbon emissions from combustion," *Journal of Geophysical Research,* vol. 109, p. D14203, 2004.

[45] P. Stelmachowski, A. Kopacz, P. Legutko, P. Indyka, M. Wojtasik, L. Ziemiański, G. Żak, Z. Sojka, and A. Kotarba, "The role of crystallite size of iron oxide catalyst for soot combustion," *Catalysis Today,* 2015.

[46] J. C. Chow, J. G. Watson, D. H. Lowenthal, P. A. Solomon, K. L. Magliano, S. D. Ziman, and L. Willard Richards, "PM10 source apportionment in California's San Joaquin valley," *Atmospheric Environment. Part A. General Topics,* vol. 26, pp. 3335-3354, 1992/12/01 1992.

[47] J. C. Chow, J. G. Watson, D. H. Lowenthal, P. A. Solomon, K. L. Magliano, S. D. Ziman, and L. W. Richards, "PM10 and PM2.5 Compositions in California's San Joaquin Valley," *Aerosol Science and Technology,* vol. 18, pp. 105-128, 1993/01/01 1993.

[48] P. Reisinger, A. Wonaschütz, R. Hitzenberger, A. Petzold, H. Bauer, N. Jankowski, H. Puxbaum, X. Chi, and W. Maenhaut, "Intercomparison of Measurement Techniques for Black or Elemental Carbon Under Urban Background Conditions in Wintertime: Influence of Biomass Combustion," *Environmental Science & Technology,* vol. 42, pp. 884-889, 2008.

[49] B. Ostro, R. Broadwin, S. Green, W. Y. Feng, and M. Lipsett, "Fine particulate air pollution and mortality in nine California counties: results from CALFINE," *Environ Health Perspect,* vol. 114, pp. 29-33, Jan 2006.

[50] F. Dominici, R. D. Peng, M. L. Bell, L. Pham, A. McDermott, S. L. Zeger, and J. M. Samet, "Fine particulate air pollution and hospital admission for cardiovascular and respiratory diseases," *JAMA,* vol. 295, pp. 1127-34, Mar 8 2006.

[51] G. J. Prescott, G. R. Cohen, R. A. Elton, F. G. Fowkes, and R. M. Agius, "Urban air pollution and cardiopulmonary ill health: a 14.5 year time series study," *Occ Environ Med,* vol. 55, pp. 697-704, Oct 1998.

[52] N. Fann, M. L. Bell, K. Walker, and B. Hubbell, "Improving the Linkages between Air Pollution Epidemiology and Quantitative Risk Assessment," *Environmental Health Perspectives,* vol. 119, pp. 1671-1675, 2011.

[53] S. Sengupta and S. Banerji, "Prevalance of dry eye diseases in rural and urban population in West Bengal and the role of air pollution," *Journal of Environmental Science, Toxicology and Food Technology,* vol. 8, pp. 45-50, 2014.

[54] G. Oberdorster, E. Oberdorster, and J. Oberdorster, "Nanotoxicology: an emerging discipline evolving from studies of ultrafine particles," *Environ Health Perspect,* vol. 113, pp. 823 - 839, 2005.

[55] G. Oberdorster, A. Maynard, K. Donaldson, V. Castranova, J. Fitzpatrick, K. Ausman, J. Carter, B. Karn, W. Kreyling, D. Lai, S. Olin, N. Monteiro-Riviere, D.

Warheit, H. Yang, and A. r. f. t. I. R. F. R. S. I. N. T. S. W. Group, "Principles for characterizing the potential human health effects from exposure to nanomaterials: elements of a screening strategy," *Particle and Fibre Toxicology,* vol. 2, p. 8, 2005.

[56]   G. Oberdorster, "Toxicology of ultrafine particles: in vivo studies," *Phil Trans Roy Soc London Series,* vol. 358, pp. 2719 - 2740, 2000.

[57]   G. Premasekharan, K. Nguyen, H. J. Forman, and V. J. Leppert, "The effect of particle size, phase and iron on low dose engineered silica-induced proinflammatory production," *Env. Sci. and Tech.,* pp. submitted March 6, 2015., 2015.

[58]   D. Napierska, L. C. J. Thomassen, V. Rabolli, D. Lison, L. Gonzalez, M. Kirsch-Volders, J. A. Martens, and P. H. Hoet, "Size-Dependent Cytotoxicity of Monodisperse Silica Nanoparticles in Human Endothelial Cells," *Small,* vol. 5, pp. 846-853, 2009.

[59]   K. Yu, C. Grabinski, A. Schrand, R. Murdock, W. Wang, B. Gu, J. Schlager, and S. Hussain, "Toxicity of amorphous silica nanoparticles in mouse keratinocytes," *Journal of Nanoparticle Research,* vol. 11, pp. 15-24, 2009.

[60]   D. Warheit, "Nanoparticles: Health impacts?," *Materials Today,* vol. 7, pp. 32 - 35, 2004.

[61]   R. B. Hefland, P. E. Schwarzel, B. V. Johansen, T. Myran, N. Uthus, and M. Refsnes, "Silica-induced cytokine release from A549 cells: importance of surface area versus size," *Human & Experimental Toxicology,* vol. 20, pp. 46-55, January 1, 2001 2001.

[62]   C. Monteiller, L. Tran, W. MacNee, S. Faux, A. Jones, B. Miller, and K. Donaldson, "The pro-inflammatory effects of low-toxicity low-solubility particles, nanoparticles and fine particles, on epithelial cells in vitro: the role of surface area," *Occupational and Environmental Medicine,* vol. 64, pp. 609-615, September 1, 2007 2007.

[63]   W. G. Kreyling, M. Semmler-Behnke, and W. Möller, "Ultrafine Particle–Lung Interactions: Does Size Matter?," *Journal of Aerosol Medicine,* vol. 19, pp. 74-83, 2006.

[64]   G. Oberdorster, Z. Sharp, V. Atudorei, A. Elder, R. Gelein, and W. Kreyling, "Translocation of inhaled ultrafine particles to the brain," *Inhal Toxicol,* vol. 16, pp. 437 - 445, 2004.

[65]   W. Kreyling, M. Semmler, F. Erbe, P. Mayer, S. Takenaka, and H. Schulz, "Translocation of ultrafine insoluble iridium particles from lung epithelium to extrapulmonary organs is size dependent but very low," *J Toxicol Environ Health A,* vol. 65, pp. 1513 - 1530, 2002.

[66]   C. F. D. Control and Prevention, "Screening young children for lead poisoning: guidance for state and local public health officials," in *Screening young children for lead poisoning: guidance for state and local public health officials*, ed: CDC, 1997.

[67]   Y. M. Zhou, C. Y. Zhong, I. M. Kennedy, V. J. Leppert, and K. E. Pinkerton, "Oxidative stress and NFκB activation in the lungs of rats: a synergistic

interaction between soot and iron particles," *Toxicology and Applied Pharmacology,* vol. 190, pp. 157-169, 7/15/ 2003.

[68]   L. W. A. Chen, J. G. Watson, J. C. Chow, and K. L. Magliano, "Quantifying PM2.5 source contributions for the San Joaquin Valley with multivariate receptor models," *Environmental Science & Technology,* vol. 41, pp. 2818-2826, Apr 2007.

[69]   X. L. Ge, A. Setyan, Y. L. Sun, and Q. Zhang, "Primary and secondary organic aerosols in Fresno, California during wintertime: Results from high resolution aerosol mass spectrometry," *Journal of Geophysical Research-Atmospheres,* vol. 117, Oct 2012.

[70]   S. Liu, L. Ahlm, D. A. Day, L. M. Russell, Y. L. Zhao, D. R. Gentner, R. J. Weber, A. H. Goldstein, M. Jaoui, J. H. Offenberg, T. E. Kleindienst, C. Rubitschun, J. D. Surratt, R. J. Sheesley, and S. Scheller, "Secondary organic aerosol formation from fossil fuel sources contribute majority of summertime organic mass at Bakersfield," *Journal of Geophysical Research-Atmospheres,* vol. 117, Dec 2012.

[71]   P. Avogbe, L. Yi Fanou, H. Autrup, S. Loft, B. Fayomi, and A. Sanni, "Ultrafine particulate matter and high-level benzene urban air pollution in relation to oxidative DNA damage," *Carcinogenesis,* vol. 26, pp. 613 - 620, 2005.

[72]   R. Hitzenberger, S. G. Jennings, S. M. Larson, A. Dillner, H. Cachier, Z. Galambos, A. Rouc, and T. G. Spain, "Intercomparison of measurement methods for black carbon aerosols," *Atmospheric Environment,* vol. 33, pp. 2823-2833, 1999.

[73]   M. O. Andreae and A. Gelencsér, "Black carbon or brown carbon? The nature of light-absorbing carbonaceous aerosols," *Atmospheric Chemistry and Physics,* vol. 6, pp. 3131-3148, 2006-07-28 2006.

[74]   V. Ramanathan and G. Carmichael, "Global and regional climate changes due to black carbon," *Nature Geosci,* vol. 1, pp. 221-227, 2008.

[75]   B. Wang, W. Y. Feng, T. C. Wang, G. Jia, M. Wang, J. W. Shi, F. Zhang, Y. L. Zhao, and Z. F. Chai, "Acute toxicity of nano- and micro-scale zinc powder in healthy adult mice," *Toxicology Letters,* vol. 161, pp. 115-123, 2006.

[76]   K. Midander, P. Cronholm, H. L. Karlsson, K. Elihn, L. Möller, C. Leygraf, and I. O. Wallinder, "Surface Characteristics, Copper Release, and Toxicity of Nano- and Micrometer-Sized Copper and Copper(II) Oxide Particles: A Cross-Disciplinary Study," *Small,* vol. 5, pp. 389-399, 2009.

[77]   J. D. Byrne and J. A. Baugh, "The significance of nanoparticles in particle-induced pulmonary fibrosis," *McGill Journal of Medicine,* vol. 11, pp. 43-50, 2008.

[78]   A. J. Ghio, T. P. Kennedy, A. R. Whorton, A. L. Crumbliss, G. E. Hatch, and J. R. Hoidal, "Role of surface complexed iron in oxidant generation and lung inflammation induced by silicates," *American Journal of Physiology - Lung Cellular and Molecular Physiology,* vol. 263, pp. L511-518, November 1, 1992 1992.

[79]   M. Bencherif, P. Lippiello, R. Lucas, and M. Marrero, "Alpha7 nicotinic receptors as novel therapeutic targets for inflammation-based diseases," *Cellular and Molecular Life Sciences,* vol. 68, pp. 931-949, 2011.

[80]   W. James Gauderman, R. O. B. McConnell, F. Gilliland, S. London, D. Thomas, E. Avol, H. Vora, K. Berhane, E. B. Rappaport, F. Lurmann, H. G. Margolis, and J. Peters, "Association between Air Pollution and Lung Function Growth in Southern California Children," *American Journal of Respiratory and Critical Care Medicine,* vol. 162, pp. 1383-1390, 2000/10/01 2000.

[81]   W. J. Gauderman , E. Avol , F. Gilliland , H. Vora , D. Thomas , K. Berhane , R. McConnell , N. Kuenzli , F. Lurmann , E. Rappaport , H. Margolis , D. Bates , and J. Peters "The Effect of Air Pollution on Lung Development from 10 to 18 Years of Age," *New England Journal of Medicine,* vol. 351, pp. 1057-1067, 2004.

[82]   G. Premasekharan, K. Nguyen, J. Contreras, V. Ramon, V. J. Leppert, and H. J. Forman, "Iron-mediated lipid peroxidation and lipid raft disruption in low-dose silica-induced macrophage cytokine production," *Free Radical Biology and Medicine,* vol. 51, pp. 1184-1194, 2011.

[83]   J. Mangum, E. Turpin, A. Antao-Menezes, M. Cesta, E. Bermudez, and J. Bonner, "Single-Walled Carbon Nanotube (SWCNT)-induced interstitial fibrosis in the lungs of rats is associated with increased levels of PDGF mRNA and the formation of unique intercellular carbon structures that bridge alveolar macrophages In Situ," *Particle and Fibre Toxicology,* vol. 3, p. 15, 2006.

[84]   L. K. Limbach, P. Wick, P. Manser, R. N. Grass, A. Bruinink, and W. J. Stark, "Exposure of Engineered Nanoparticles to Human Lung Epithelial Cells: Influence of Chemical Composition and Catalytic Activity on Oxidative Stress," *Environmental Science & Technology,* vol. 41, pp. 4158-4163, 2007.

[85]   E. Gazzano, F. Turci, E. Foresti, M. G. Putzu, E. Aldieri, F. Silvagno, I. G. Lesci, M. Tomatis, C. Riganti, C. Romano, B. Fubini, N. Roveri, and D. Ghigo, "Iron-Loaded Synthetic Chrysotile: A New Model Solid for Studying the Role of Iron in Asbestos Toxicity," *Chemical Research in Toxicology,* vol. 20, pp. 380-387, 2007/03/01 2007.

[86]   B. Fubini and L. Mollo, "Role of iron in the reactivity of mineral fibers," *Toxicology Letters,* vol. 82–83, pp. 951-960, 1995.

[87]   T. Xia, P. Korge, J. N. Weiss, N. Li, M. I. Venkatesen, C. Sioutas, and A. Nel, "Quinones and aromatic chemical compounds in particulate matter induce mitochondrial dysfunction: implications for ultrafine particle toxicity," *Environmental Health Perspectives,* vol. 112, pp. 1347-58, Oct 2004.

[88]   T. Xia, P. Korge, J. N. Weiss, N. Li, M. I. Venkatesen, C. Sioutas, and A. Nel, "Quinones and aromatic chemical compounds in particulate matter induce mitochondrial dysfunction: implications for ultrafine particle toxicity," *Environ Health Perspect,* vol. 112, pp. 1347-58, Oct 2004.

[89]   UCDAVIS-DELTAGROUP. (2016). *The DELTA Group for the Detection and Evaluation of the Long-Range Transport of Aerosols*. Available: http://delta.ucdavis.edu/technology.htm#8-DRUM Sampler

[90]   D. Vaniman, "Environmental Restoration Project Standard Operating Procedure for:Clay Mineral and Zeolite Separation," D. o. Energy, Ed., ed: Los Alamos National Laboratory, 2001.

[91]   W. Stöber, A. Fink, and E. Bohn, "Controlled growth of monodisperse silica spheres in the micron size range," *Journal of Colloid and Interface Science,* vol. 26, pp. 62-69, 1968.

[92]   A. J. Ghio, T. P. Kennedy, A. R. Whorton, A. L. Crumbliss, G. E. Hatch, and J. R. Hoidal, "Role of surface complexed iron in oxidant generation and lung inflammation induced by silicates," *Am J Physiol Lung Cell Mol Physiol,* vol. 263, pp. L511-518, November 1, 1992 1992.

[93]   R. S. Pandurangi, M. S. Seehra, B. L. Razzaboni, and P. Bolsaitis, "Surface and Bulk Infrared Modes of Crystalline and Amorphous Silica Particles: A Sutdy of the Relation of Sufrace Structureto Cytotoxicity of Resirable Silica," *Environmental Health Perspectives,* vol. 86, pp. 327-336, 1990.

[94]   X. Jiang, Y.-B. Jiang, and C. J. Brinker, "Hydrothermal synthesis of monodisperse single-crystalline alpha-quartz nanospheres," *Chemical Communications,* vol. 47, pp. 7524-7526, 2011.

[95]   J. I. Goldstein, D. E. Newbury, P. Echlin, D. C. Joy, C. E. Lyman, E. Lifshin, L. Sawyer, and J. R. Michael, *Scanning Electron Microscopy and X-Ray Microanalysis*, Third Ediition ed. New York: Springer Science + Business Media, LLC, 2003.

[96]   D. B. Williams and C. B. Carter, *Transmission Electron Microscopy*. New York: Springer Science + Business Media, LLC 2009.

[97]   J. Jasinski, K. E. Pinkerton, I. M. Kennedy, and V. J. Leppert, "Spatially Resolved Energy Electron Loss Spectroscopy Studies of Iron Oxide Nanoparticles," *Microscopy and Microanalysis,* vol. 12, pp. 424-431, 2006.

[98]   J. Everett, E. Céspedes, L. R. Shelford, C. Exley, J. F. Collingwood, J. Dobson, G. van der Laan, C. A. Jenkins, E. Arenholz, and N. D. Telling, "Ferrous iron formation following the co-aggregation of ferric iron and the Alzheimer's disease peptide β-amyloid (1–42)," *Journal of The Royal Society Interface,* vol. 11, 2014-06-06 00:00:00 2014.

[99]   R. M. Cornell and U. Schwertmann, *The iron oxides: structure, properties, reactions, occurrences and uses Weinhein*. VCH, New York, 1996.

[100]   P. A. O'day, N. Rivera, R. Root, and S. A. Carroll, "X-ray absorption spectroscopic study of Fe reference compounds for the analysis of natural sediments," *American Mineralogist,* vol. 89, pp. 572-585, 2004.

[101]   B. Ravel and M. Newville, "ATHENA, ARTEMIS, HEPHAESTUS: data analysis for X-ray absorption spectroscopy using IFEFFIT," *Journal of synchrotron radiation,* vol. 12, pp. 537-541, 2005.

[102]   B. D. Cullity, *Elements of X-ray Diffraction* 2nd ed.: Addison-Wesley Publishing Company, 1978.

[103]   G. Leofanti, M. Padovan, G. Tozzola, and B. Venturelli, "Surface area and pore texture of catalysts," *Catalysis Today,* vol. 41, pp. 207-219, 1998.

[104] H. L. Michael and D. J. A. Williams, "Electrochemical properties of quartz," *Journal of Electroanalytical Chemistry and Interfacial Electrochemistry,* vol. 179, pp. 131-139, 1984.

[105] A. Salis, D. F. Parsons, M. Boström, L. Medda, B. Barse, B. W. Ninham, and M. Monduzzi, "Ion Specific Surface Charge Density of SBA-15 Mesoporous Silica," *Langmuir,* vol. 26, pp. 2484-2490, 2010/02/16 2009.

[106] K. He, F. Yang, Y. Ma, Q. Zhang, X. Yao, C. K. Chan, S. Cadle, T. Chan, and P. Mulawa, "The characteristics of PM2.5 in Beijing, China," *Atmospheric Environment,* vol. 35, pp. 4959-4970, 2001.

[107] P. R. Haddad, "Ion chromatography," *Handbook on Metals in Clinical and Analytical Chemistry,* p. 135, 1994.

[108] J. C. Chow, J. G. Watson, L. C. Pritchett, W. R. Pierson, C. A. Frazier, and R. G. Purcell, "The dri thermal/optical reflectance carbon analysis system: description, evaluation and applications in U.S. Air quality studies," *Atmospheric Environment. Part A. General Topics,* vol. 27, pp. 1185-1201, 1993/06/01 1993.

[109] M. Daigneault, J. A. Preston, H. M. Marriott, M. K. B. Whyte, and D. H. Dockrell, "The Identification of Markers of Macrophage Differentiation in PMA-Stimulated THP-1 Cells and Monocyte-Derived Macrophages," *PLoS ONE,* vol. 5, p. e8668, 2010.

[110] H. Schwende, E. Fitzke, P. Ambs, and P. Dieter, "Differences in the state of differentiation of THP-1 cells induced by phorbol ester and 1,25-dihydroxyvitamin D3," *Journal of Leukocyte Biology,* vol. 59, pp. 555-61, April 1, 1996 1996.

[111] L. A. Bottalico, R. E. Wager, L. B. Agellon, R. K. Assoian, and I. Tabas, "Transforming growth factor-beta 1 inhibits scavenger receptor activity in THP-1 human macrophages," *The Journal of Biological Chemistry,* vol. 266, pp. 22866-22871, December 5, 1991 1991.

[112] H. Takemura, H. Yamamoto, H. Kunishima, H. Ikejima, T. Hara, K. Kanemitsu, S. Terakubo, Y. Shoji, M. Kaku, and J. Shimada, "Evaluation of a human monocytic cell line THP-1 model for assay of the intracellular activities of antimicrobial agents against Legionella pneumophila," *Journal of Antimicrobial Chemotherapy,* vol. 46, pp. 589-594, October 1, 2000 2000.

[113] M. E. Samberg, S. J. Oldenburg, and N. A. Monteiro-Riviere, "Evaluation of Silver Nanoparticle Toxicity in Skin in Vivo and Keratinocytes in Vitro," *Environ Health Perspect,* vol. 118, 2009.

[114] M. Fisichella, H. Dabboue, S. Bhattacharyya, M.-L. Saboungi, J.-P. Salvetat, T. Hevor, and M. Guerin, "Mesoporous silica nanoparticles enhance MTT formazan exocytosis in HeLa cells and astrocytes," *Toxicology in Vitro,* vol. 23, pp. 697-703, 2009.

[115] H. Liu, H. Zhang, and H. J. Forman, "Silica induces macrophage cytokines through phosphatidylcholine-specific phospholipase C with H_2O_2," *American Journal of Respiratory Cell and Molecular Biology,* pp. 2006-0297OC, December 7, 2006 2006.

[116] C. Colliex, T. Manoubi, and C. Ortiz, "Electron-energy-loss-spectroscopy near-edge fine structures in the iron-oxygen system," *Physical Review B,* vol. 44, pp. 11402-11411, 1991.

[117] M. Obst and G. Schmid, "3D chemical mapping: application of scanning transmission (soft) X-ray microscopy (STXM) in combination with angle-scan tomography in bio-, geo-, and environmental sciences.," *Methods in Molecular Biology,* vol. 1117, pp. 757-81, 2014.

[118] J. Grebenkemper. (2016, April 21, 2016). *Powder X-Ray Diffraction*. Available: http://chemwiki.ucdavis.edu/Core/Analytical_Chemistry/Instrumental_Analysis/Diffraction/Powder_X-ray_Diffraction

[119] X. Ge, A. Setyan, Y. Sun, and Q. Zhang, "Primary and secondary organic aerosols in Fresno, California during wintertime: Results from high resolution aerosol mass spectrometry," *Journal of Geophysical Research: Atmospheres,* vol. 117, 2012.

[120] E. Peré-Trepat, E. Kim, P. Paatero, and P. K. Hopke, "Source apportionment of time and size resolved ambient particulate matter measured with a rotating DRUM impactor," *Atmospheric Environment,* vol. 41, pp. 5921-5933, 2007.

[121] T. Cahill, K. Boberg, and D. E. Barnes, "Deposition of coarse toxic particles in Wilmington, CA for the Department of Toxic Substances Control (DTSC): Summer, 2008, and Spring, 2009," The UC Davis DELTA Group2011.

[122] C. Perrino, S. Canepari, and M. Catrambone, "Comparing the Performance of Teflon and Quartz Membrane Filters Collecting Atmospheric PM: Influence of Atmospheric Water," *Aerosol and Air Quality Research,* vol. 13, pp. 137-147, 2013.

[123] S. K. Friedlander, "Chemical element balances and identification of air pollution sources," *Environmental Science & Technology,* vol. 7, pp. 235-240, 1973/03/01 1973.

[124] W. Licht, *Air pollution control engineering: basic calculations for particulate collection*, 2nd ed. New York: Marcel Dekker, Inc., 1988.

[125] D. N. Stooto and E. D. Dikio, "Morphological Characterization of Soot From the Combustion of Candle Wax " *International Journal of Electrochemical Science,* 2011.

[126] W. MacNee and K. Donaldson, "Mechanism of lung injury caused by PM10 and ultrafine particles with special reference to COPD," *European Respiratory Journal,* vol. 21, pp. 47s-51s, 2003.

[127] J. L. Fabec and M. L. Ruschak, "Determination of nickel, vanadium, and sulfur in crudes and heavy crude fractions by inductively coupled argon plasma atomic emission spectrometry and flame atomic absorption spectrometry," *Analytical Chemistry,* vol. 57, pp. 1853-1863, 1985/08/01 1985.

[128] C.-N. Millet, R. Chédotal, and P. Da Costa, "Synthetic gas bench study of a 4-way catalytic converter: Catalytic oxidation, NOx storage/reduction and impact of soot loading and regeneration," *Applied Catalysis B: Environmental,* vol. 90, pp. 339-346, 2009.

[129] M. A. Peralta, V. G. Milt, L. M. Cornaglia, and C. A. Querini, "Stability of Ba,K/CeO2 catalyst during diesel soot combustion: Effect of temperature, water, and sulfur dioxide," *Journal of Catalysis,* vol. 242, pp. 118-130, 2006.

[130] H. Ohno, K. Matsubae, K. Nakajima, Y. Kondo, S. Nakamura, and T. Nagasaka, "Toward the efficient recycling of alloying elements from end of life vehicle steel scrap," *Resources, Conservation and Recycling,* vol. 100, pp. 11-20, 2015.

[131] W. L. Dalmijn and J. A. v. Houwelingen, *New developments in the processing of the non ferrous metal fraction of car scrap*. Warrendale, PA: Minerals, Metals and Materials Society, 1995.

[132] W. L. Dalmijn and T. P. R. Jong, "The development of vehicle recycling in Europe: Sorting, shredding, and separation," *JOM,* vol. 59, pp. 52-56, 2007.

[133] N. Ojeda, E. D. Greaves, J. Alvarado, and L. Sajo-Bohus, "Determination of V, Fe, Ni and S in petroleum crude oil by total-reflection X-ray fluorescence," *Spectrochimica Acta Part B: Atomic Spectroscopy,* vol. 48, pp. 247-253, 1993/02/01 1993.

[134] P. Sreenivasulu, N. Viswanadham, and S. K. Saxena, "Facile synthesis of mesoporous aluminosilicate nanoparticles for the selective production of N-benzylidenaniline in a solvent-free reaction of aniline with benzyl alcohol," *Journal of Materials Chemistry A,* vol. 2, pp. 7354-7359, 2014.

[135] D. Krewski, R. A. Yokel, E. Nieboer, D. Borchelt, J. Cohen, J. Harry, S. Kacew, J. Lindsay, A. M. Mahfouz, and V. Rondeau, "HUMAN HEALTH RISK ASSESSMENT FOR ALUMINIUM, ALUMINIUM OXIDE, AND ALUMINIUM HYDROXIDE," *J Toxicol Environ Health Part B,* vol. 10, pp. 1-269, 2007.

[136] G. B. Alexander, W. M. Heston, and R. K. Iler, "The Solubility of Amorphous Silica in Water," *The Journal of Physical Chemistry,* vol. 58, pp. 453-455, 1954/06/01 1954.

[137] N. E. Sánchez, A. Callejas, Á. Millera, R. Bilbao, and M. U. Alzueta, "Polycyclic Aromatic Hydrocarbon (PAH) and Soot Formation in the Pyrolysis of Acetylene and Ethylene: Effect of the Reaction Temperature," *Energy & Fuels,* vol. 26, pp. 4823-4829, 2012/08/16 2012.

[138] N. Li, T. Xia, and A. E. Nel, "The role of oxidative stress in ambient particulate matter-induced lung diseases and its implications in the toxicity of engineered nanoparticles," *Free Radical Biology and Medicine,* vol. 44, pp. 1689-1699, 2008.

[139] U. Schwertmann and E. Murad, "Effect of pH on the Formation of Goethite and Hematite from Ferrihydrte," *Clays and Clay Minerals,* vol. 31, pp. 272-284, 1983.

[140] SJVAPCD, "2015 Air Monitoring Network Plan," pp. Available at: www.valleyair.org/aqinfo/Docs/2015-Air-Monitoring-Network-Plan.pdf, August 28, 2015 2015.

[141] B. De Berardis, E. Incocciati, S. Massera, G. Gargaro, and L. Paoletti, "Airborne silica levels in an urban area," *Science of The Total Environment,* vol. 382, pp. 251-258, 2007.

[142] B. L. Davis, L. R. Johnson, R. K. Stevens, W. J. Courtney, and D. W. Safriet, "The quartz content and elemental composition of aerosols from selected sites of

the EPA inhalable particulate network," *Atmospheric Environment (1967),* vol. 18, pp. 771-782, 1984.

[143] V. Castranova, N. Dalal, and V. Vallyathan, Eds., *Silica and silica-induced lung diseases*. New York: CRC Press, 1996, p.^pp. Pages.

[144] L. M. Costantini, R. M. Gilberti, and D. A. Knecht, "The Phagocytosis and Toxicity of Amorphous Silica," *PLoS ONE,* vol. 6, p. e14647, 2011.

[145] C. J. Johnston, K. E. Driscoll, J. N. Finkelstein, R. Baggs, M. A. O'Reilly, J. Carter, R. Gelein, and G. Oberdörster, "Pulmonary chemokine and mutagenic responses in rats after subchronic inhalation of amorphous and crystalline silica," *Toxicological Sciences,* vol. 56, pp. 405-413, August 1, 2000 2000.

[146] A. Sayari, S. Hamoudi, and Y. Yang, "Applications of Pore-Expanded Mesoporous Silica. 1. Removal of Heavy Metal Cations and Organic Pollutants from Wastewater," *Chemistry of Materials,* vol. 17, pp. 212-216, 2005/01/01 2005.

[147] J. Fan, C. Yu, F. Gao, J. Lei, B. Tian, L. Wang, Q. Luo, B. Tu, W. Zhou, and D. Zhao, "Cubic Mesoporous Silica with Large Controllable Entrance Sizes and Advanced Adsorption Properties," *Angewandte Chemie,* vol. 115, pp. 3254-3258, 2003.

[148] W. Kreyling, M. Semmler-Behnke, and W. Möller, "Health implications of nanoparticles," *Journal of Nanoparticle Research,* vol. 8, pp. 543-562, 2006.

[149] A. G. Heppleston, "Silica, pneumoconiosis, and carcinoma of the lung," *American Journal of Industrial Medicine,* vol. 7, pp. 285-294, 1985.

[150] K. Steenland and D. F. Goldsmith, "Silica exposure and autoimmune diseases," *American Journal of Industrial Medicine,* vol. 28, pp. 603-608, 1995.

[151] J. J. Wang, B. J. S. Sanderson, and H. Wang, "Cytotoxicity and genotoxicity of ultrafine crystalline SiO2 particulate in cultured human lymphoblastoid cells," *Environmental and Molecular Mutagenesis,* vol. 48, pp. 151-157, 2007.

[152] Y. Chen, J. Chen, J. Dong, and Y. Jin, "Comparing study of the effect of nanosized silicon dioxide and microsized silicon dioxide on fibrogenesis in rats," *Toxicology and Industrial Health,* vol. 20, pp. 21-27, February/June 2004 2004.

[153] D. B. Warheit, T. R. Webb, V. L. Colvin, K. L. Reed, and C. M. Sayes, "Pulmonary Bioassay Studies with Nanoscale and Fine-Quartz Particles in Rats: Toxicity is Not Dependent upon Particle Size but on Surface Characteristics," *Toxicological Sciences,* vol. 95, pp. 270-280, January 1, 2007 2007.

[154] Z. Chu, Y. Huang, Q. Tao, and Q. Li, "Cellular uptake, evolution, and excretion of silica nanoparticles in human cells," *Nanoscale,* vol. 3, pp. 3291-3299, 2011.

[155] K. S. Rao, K. El-Hami, T. Kodaki, K. Matsushige, and K. Makino, "A novel method for synthesis of silica nanoparticles," *Journal of Colloid and Interface Science,* vol. 289, pp. 125-131, 9/1/ 2005.

[156] G. H. Bogush, M. A. Tracy, and C. F. Zukoski Iv, "Preparation of monodisperse silica particles: Control of size and mass fraction," *Journal of Non-Crystalline Solids,* vol. 104, pp. 95-106, 1988.

[157] V. A. Fadok, D. L. Bratton, A. Konowal, P. W. Freed, J. Y. Westcott, and P. M. Henson, "Macrophages that have ingested apoptotic cells in vitro inhibit proinflammatory cytokine production through autocrine/paracrine mechanisms

involving TGF-beta, PGE2, and PAF," *The Journal of Clinical Investigation,* vol. 101, pp. 890-898, 1998.

[158]   K. Kurosaka, N. Watanabe, and Y. Kobayashi, "Production of Proinflammatory Cytokines by Resident Tissue Macrophages after Phagocytosis of Apoptotic Cells," *Cellular Immunology,* vol. 211, pp. 1-7, 2001.

[159]   H. R. Paur, F. R. Cassee, J. Teeguarden, H. Fissan, S. Diabate, M. Aufderheide, W. G. Kreyling, O. Hänninen, G. Kasper, M. Riediker, B. Rothen-Rutishauser, and O. Schmid, "In-vitro cell exposure studies for the assessment of nanoparticle toxicity in the lung—A dialog between aerosol science and biology," *Journal of Aerosol Science,* vol. 42, pp. 668-692, 2011.

[160]   S. Takahama, S. Liu, and L. M. Russell, "Coatings and clusters of carboxylic acids in carbon-containing atmospheric particles from spectromicroscopy and their implications for cloud-nucleating and optical properties," *J Geophysl Res,* vol. 115, p. D01202, 2010.

[161]   C. Antognelli, A. Gambelunghe, C. Del Buono, N. Murgia, V. N. Talesa, and G. Muzi, "Crystalline silica Min-U-Sil 5 induces oxidative stress in human bronchial epithelial cells BEAS-2B by reducing the efficiency of antiglycation and antioxidant enzymatic defenses," *Chemico-Biological Interactions,* vol. 182, pp. 13-21, 2009.

[162]   D. M. Brown, M. R. Wilson, W. MacNee, V. Stone, and K. Donaldson, "Size-Dependent Proinflammatory Effects of Ultrafine Polystyrene Particles: A Role for Surface Area and Oxidative Stress in the Enhanced Activity of Ultrafines," *Toxicology and Applied Pharmacology,* vol. 175, pp. 191-199, 2001.

[163]   J. S. Chang, K. L. B. Chang, D. F. Hwang, and Z. L. Kong, "In Vitro Cytotoxicitiy of Silica Nanoparticles at High Concentrations Strongly Depends on the Metabolic Activity Type of the Cell Line," *Environmental Science & Technology,* vol. 41, pp. 2064-2068, 2007.

[164]   B. Fubini, "Surface reactivity in the pathogenic response to particulates," *Environ Health Perspect,* vol. 105, pp. 1013-1020, 1997.

[165]   D. Napierska, L. Thomassen, D. Lison, J. Martens, and P. Hoet, "The nanosilica hazard: another variable entity," *Particle and Fibre Toxicology,* vol. 7, p. 39, 2010.

[166]   E. S. Gurzau, C. Neagu, and A. E. Gurzau, "Essential metals—case study on iron," *Ecotoxicology and Environmental Safety,* vol. 56, pp. 190-200, 2003.

[167]   Y. Kumagai, Y. Shinkai, T. Miura, and A. K. Cho, "The chemical biology of naphthoquinones and its environmental implications," *Annu Rev Pharmacol Toxicol,* vol. 52, pp. 221-47, 2012.

[168]   R. M. Liu, L. Gao, J. Choi, and H. J. Forman, "g-Glutamylcysteine synthetase: mRNA stabilization and independent subunit transcription by 4-hydroxy-2-nonenal," *Am J Physiol,* vol. 275, pp. L861-9, 1998.

[169]   S. Levy, A. K. Jaiswal, and H. J. Forman, "The role of c-Jun phosphorylation in EpRE activation of phase II genes," *Free Radic Biol Med,* vol. 47, pp. 1172-9, Oct 15 2009.

[170] S. Levy and H. J. Forman, "c-Myc is a Nrf2-interacting protein that negatively regulates phase II genes through their electrophile responsive elements," *IUBMB Life,* vol. 62, pp. 237-46, Mar 2010.

[171] D. M. Krzywanski, D. A. Dickinson, K. E. Iles, A. F. Wigley, C. C. Franklin, R. M. Liu, T. J. Kavanagh, and H. J. Forman, "Variable regulation of glutamate cysteine ligase subunit proteins affects glutathione biosynthesis in response to oxidative stress," *Arch Biochem Biophys,* vol. 423, pp. 116-125, Mar 1 2004.

[172] N. Kaul and H. J. Forman, "Activation of NF kappa B by the respiratory burst of macrophages," *Free Radic Biol Med,* vol. 21, pp. 401-5, 1996.

[173] N. Kaul, R. Gopalakrishna, U. Gundimeda, J. Choi, and H. J. Forman, "Role of protein kinase C in basal and hydrogen peroxide-stimulated NF-kappa B activation in the murine macrophage J774A.1 cell line," *Arch Biochem Biophys,* vol. 350, pp. 79-86, Feb 1 1998.

[174] J. Giron-Calle, K. Srivatsa, and H. J. Forman, "Priming of alveolar macrophage respiratory burst by H_2O_2 is prevented by phosphatidylcholine-specific phospholipase C inhibitor Tricyclodecan-9-yl-xanthate (D609)," *J Pharmacol Exp Ther* vol. 301, pp. 87-94, Apr 2002.

[175] H. Liu, H. Zhang, and H. J. Forman, "Silica induces macrophage cytokines through phosphatidylcholine-specific phospholipase C with hydrogen peroxide," *Am J Respir Cell Mol Biol,* vol. 36, pp. 594-9, May 2007.

[176] L. C. Varanda, M. P. Morales, J. M. Jafelicci, and C. J. Serna, "Monodispersed spindle-type goethite nanoparticles from FeIII solutions," *Journal of Materials Chemistry,* vol. 12, pp. 3649-3653, 2002.

[177] A. Navrotsky, L. Mazeina, and J. Majzlan, "Size-Driven Structural and Thermodynamic Complexity in Iron Oxides," *Science,* vol. 319, pp. 1635-1638, March 21, 2008 2008.

[178] T. N. Perkins, P. M. Peeters, A. Shukla, I. Arijs, J. Dragon, E. F. M. Wouters, N. L. Reynaert, and B. T. Mossman, "Indications for distinct pathogenic mechanisms of asbestos and silica through gene expression profiling of the response of lung epithelial cells," *Human Molecular Genetics,* vol. 24, pp. 1374-1389, March 1, 2015 2015.

[179] J. S. Lighty, J. M. Veranth, and A. F. Sarofim, "Combustion Aerosols: Factors Governing Their Size and Composition and Implications to Human Health," *Journal of the Air & Waste Management Association,* vol. 50, pp. 1565-1618, 2000/09/01 2000.

[180] X. Huang, "Iron overload and its association with cancer risk in humans: evidence for iron as a carcinogenic metal," *Mutation Research/Fundamental and Molecular Mechanisms of Mutagenesis,* vol. 533, pp. 153-171, 12/10/ 2003.

[181] J. L. Turi, F. Yang, M. D. Garrick, C. A. Piantadosi, and A. J. Ghio, "The iron cycle and oxidative stress in the lung," *Free Radical Biology and Medicine,* vol. 36, pp. 850-857, 4/1/ 2004.

[182] C. C. Koch, O. B. Cavin, C. G. McKamey, and J. O. Scarbrough, "Preparation of amorphous; NiNb by mechanical alloying," *Applied Physics Letters,* vol. 43, pp. 1017-1019, 1983.

[183] M. T. Costello, "X-ray diffraction of amorphous and crystalline overbased sulphonates," *Tribotest,* vol. 11, pp. 207-212, 2005.

[184] M. Inada, A. Nishinosono, K. Kamada, N. Enomoto, and J. Hojo, "Microwave-assisted sol–gel process for production of spherical mesoporous silica materials," *Journal of Materials Science,* vol. 43, pp. 2362-2366, 2008.

[185] A. d. Sousa, K. C. d. Souza, N. D. S. Mohallem, R. G. d. Sousa, and E. s. M. B. d. Sousa., "Multifunctional Nanocomposites Based on Mesoporous Silica: Potential Applications in Biomedicine," *Advances in Diverse Industrial Applications of Nanocomposites,* pp. 177-202, 2011.

[186] M. Kruk, M. Jaroniec, and A. Sayari, "Adsorption Study of Surface and Structural Properties of MCM-41 Materials of Different Pore Sizes," *The Journal of Physical Chemistry B,* vol. 101, pp. 583-589, 1997/01/01 1997.

[187] J. Wloch, M. Rozwadowski, M. Lezanska, and K. Erdmann, "Analysis of the pore structure of the MCM-41 materials," *Applied Surface Science,* vol. 191, pp. 368-374, 2002.

[188] H. E. Bumsted, "Determination of Alpha-Quartz in the Respirable Portion of Airborne Participates by X-ray Diffraction," *American Industrial Hygiene Association Journal,* vol. 34, pp. 150-158, 1973/04/01 1973.

[189] J. F. Bertone, J. Cizeron, R. K. Wahi, J. K. Bosworth, and V. L. Colvin, "Hydrothermal Synthesis of Quartz Nanocrystals," *Nano Letters,* vol. 3, pp. 655-659, 2003/05/01 2003.

[190] D. Warheit, G. George, L. Hill, R. Snyderman, and A. Brody, "Inhaled asbestos activates a complement-dependent chemoattractant for macrophages," *Laboratory Investigation,* vol. 52, pp. 505 - 514, 1985.

[191] D. M. Krzywanski, D. A. Dickinson, K. E. Iles, A. F. Wigley, C. C. Franklin, R.-M. Liu, T. J. Kavanagh, and H. J. Forman, "Variable regulation of glutamate cysteine ligase subunit proteins affects glutathione biosynthesis in response to oxidative stress," *Archives of Biochemistry and Biophysics,* vol. 423, pp. 116-125, 2004.

[192] S. A. Rushworth, X.-L. Chen, N. Mackman, R. M. Ogborne, and M. A. O'Connell, "Lipopolysaccharide-Induced Heme Oxygenase-1 Expression in Human Monocytic Cells Is Mediated via Nrf2 and Protein Kinase C," *The Journal of Immunology,* vol. 175, pp. 4408-4415, October 1, 2005 2005.

[193] T. Laaksonen, H. Santos, H. Vihola, J. Salonen, J. Riikonen, T. Heikkilä, L. Peltonen, N. Kumar, D. Y. Murzin, V.-P. Lehto, and J. Hirvonen, "Failure of MTT as a Toxicity Testing Agent for Mesoporous Silicon Microparticles," *Chemical Research in Toxicology,* vol. 20, pp. 1913-1918, 2007.

[194] N. A. Monteiro-Riviere and A. O. Inman, "Challenges for assessing carbon nanomaterial toxicity to the skin," *Carbon,* vol. 44, pp. 1070-1078, 2006.

[195] Y. Okimoto, A. Watanabe, E. Niki, T. Yamashita, and N. Noguchi, "A novel fluorescent probe diphenyl-1-pyrenylphosphine to follow lipid peroxidation in cell membranes," *FEBS Letters,* vol. 474, pp. 137-140, 2000.

[196] M. Takahashi, M. Shibata, and E. Niki, "Estimation of lipid peroxidation of live cells using a fluorescent probe, Diphenyl-1-pyrenylphosphine," *Free Radical Biology and Medicine,* vol. 31, pp. 164-174, 2001.

[197] F. Hong, K. R. Sekhar, M. L. Freeman, and D. C. Liebler, "Specific patterns of electrophile adduction trigger Keap1 ubiquitination and Nrf2 activation," *J Biol Chem,* vol. 280, pp. 31768-75, Sep 9 2005.

[198] A. Malloy, "Count, size and visualize nanoparticles," *Materials Today,* vol. 14, pp. 170-173, 2011.

[199] H. Dongeun, G. Wei, K. Yoko, B. G. James, and T. Shuichi, "Microfluidics for flow cytometric analysis of cells and particles," *Physiological Measurement,* vol. 26, p. R73, 2005.

[200] R. M. Cornell, R. Giovanoli, and P. W. Schindler, "Effect of Silicate Species on the Transformation of Ferrihydrite into Goethite and Hematite in Alkaline Media," *Clays and Clay Minerals,* vol. 35, pp. 21-28, 1987.

[201] J. Zhao, F. E. Huggins, Z. Feng, and G. P. Huffman, "Ferrihydrite: Surface Structure and its Effects on Phase Transformations," *Clays and Clay Minerals,* vol. 42, pp. 737-746, 1994.

[202] M. Ozaki, S. Kratohvil, and E. Matijević, "Formation of monodispersed spindle-type hematite particles," *Journal of Colloid and Interface Science,* vol. 102, pp. 146-151, 1984/11/01 1984.

[203] M. Spuch-Calvar, J. Pérez-Juste, and L. M. Liz-Marzán, "Hematite spindles with optical functionalities: Growth of gold nanoshells and assembly of gold nanorods," *Journal of Colloid and Interface Science,* vol. 310, pp. 297-301, 2007.

[204] T. Nagano, S. Nakashima, S. Nakayama, and M. Senoo, "The Use of Color to Quantify the Effects of pH and Temperature on teh Crystallization Kinetics of Goethite under Highly Alkaline Conditions," *Clays and Clay Minerals,* vol. 42, pp. 226-234, 1994.

[205] A. W. Schroth, J. Crusius, E. R. Sholkovitz, and B. C. Bostick, "Iron solubility driven by speciation in dust sources to the ocean," *Nat Geosci,* vol. 2, pp. 337-340, May 2009.

[206] D. M. Cwiertny, M. A. Young, and V. H. Grassian, "Chemistry and photochemistry of mineral dust aerosol," *Annu Rev Phys Chem,* vol. 59, pp. 27-51, 2008 2008.

[207] Y. Xu and L. Axe, "Synthesis and characterization of iron oxide-coated silica and its effect on metal adsorption," *Journal of Colloid and Interface Science,* vol. 282, pp. 11-19, 2005.

[208] B. Chamnankid, T. Witoon, P. Kongkachuichay, and M. Chareonpanich, "One-pot synthesis of core–shell silica–aluminosilicate composites: Effect of pH and chitosan addition," *Colloids and Surfaces A: Physicochemical and Engineering Aspects,* vol. 380, pp. 319-326, 2011.

[209] J. Shin, N. H. Ahn, M. A. Camblor, C. M. Zicovich-Wilson, and S. B. Hong, "Synthesis of Aluminosilicate Natrolites and Control of Their Tetrahedral Atom Ordering," *Chemistry of Materials,* vol. 26, pp. 3361-3363, 2014/06/10 2014.

[210] P. Nioi and J. D. Hayes, "Contribution of NAD(P)H:quinone oxidoreductase 1 to protection against carcinogenesis, and regulation of its gene by the Nrf2 basic-region leucine zipper and the arylhydrocarbon receptor basic helix-loop-helix transcription factors," *Mutation Research/Fundamental and Molecular Mechanisms of Mutagenesis,* vol. 555, pp. 149-171, 2004.

[211] R. S. Hamilton and T. A. Mansfield, "Airborne particulate elemental carbon: Its sources, transport and contribution to dark smoke and soiling," *Atmospheric Environment. Part A. General Topics,* vol. 25, pp. 715-723, 1991.

[212] J. E. Penner, H. Eddleman, and T. Novakov, "Towards the development of a global inventory for black carbon emissions," *Atmospheric Environment. Part A. General Topics,* vol. 27, pp. 1277-1295, 1993.

[213] T. C. Bond and H. Sun, "Can Reducing Black Carbon Emissions Counteract Global Warming?," *Environmental Science & Technology,* vol. 39, pp. 5921-5926, 2005.

[214] S. Sharma, J. R. Brook, H. Cachier, J. Chow, A. Gaudenzi, and G. Lu, "Light absorption and thermal measurements of black carbon in different regions of Canada," *Journal of Geophysical Research,* vol. 107, p. 4771, December 20, 2002 2002.

[215] J. F. Lamarque, T. C. Bond, V. Eyring, C. Granier, A. Heil, Z. Klimont, D. Lee, C. Liousse, A. Mieville, B. Owen, M. G. Schultz, D. Shindell, S. J. Smith, E. Stehfest, J. Van Aardenne, O. R. Cooper, M. Kainuma, N. Mahowald, J. R. McConnell, V. Naik, K. Riahi, and D. P. van Vuuren, "Historical (1850–2000) gridded anthropogenic and biomass burning emissions of reactive gases and aerosols: methodology and application," *Atmos. Chem. Phys.,* vol. 10, pp. 7017-7039, 2010.

[216] U.S.EPA, "Chapter 4: Emissions of Black Carbon," *Report to Congress on Carbon Black,* pp. 85-114, 2012.

[217] D. Sahu, G. M. Kannan, and R. Vijayaraghavan, "Carbon Black Particle Exhibits Size Dependent Toxicity in Human Monocytes," *International Journal of Inflammation,* vol. 2014, p. 10, 2014.

[218] A. Onoda, M. Umezawa, K. Takeda, T. Ihara, and M. Sugamata, "Effects of Maternal Exposure to Ultrafine Carbon Black on Brain Perivascular Macrophages and Surrounding Astrocytes in Offspring Mice," *PLoS ONE,* vol. 9, p. e94336, 2014.

[219] N. R. Jacobsen, P. A. White, J. Gingerich, P. Møller, A. T. Saber, G. R. Douglas, U. Vogel, and H. Wallin, "Mutation spectrum in FE1-MUTATMMouse lung epithelial cells exposed to nanoparticulate carbon black," *Environmental and Molecular Mutagenesis,* vol. 52, pp. 331-337, 2011.

[220] N. R. Jacobsen, A. T. Saber, P. White, P. Møller, G. Pojana, U. Vogel, S. Loft, J. Gingerich, L. Soper, G. R. Douglas, and H. Wallin, "Increased mutant frequency by carbon black, but not quartz, in the lacZ and cII transgenes of muta™mouse lung epithelial cells," *Environmental and Molecular Mutagenesis,* vol. 48, pp. 451-461, 2007.

[221] A. T. Saber, K. A. Jensen, N. R. Jacobsen, R. Birkedal, L. Mikkelsen, P. Møller, S. Loft, H. Wallin, and U. Vogel, "Inflammatory and genotoxic effects of nanoparticles designed for inclusion in paints and lacquers," *Nanotoxicology,* vol. 6, pp. 453-471, 2012/08/01 2012.

[222] N. R. Jacobsen, P. Moller, K. A. Jensen, U. Vogel, O. Ladefoged, S. Loft, and H. Wallin, "Lung inflammation and genotoxicity following pulmonary exposure to nanoparticles in ApoE-/- mice," *Part Fibre Toxicol,* vol. 6, p. 2, 2009.

[223] E. Herzog, A. Casey, F. M. Lyng, G. Chambers, H. J. Byrne, and M. Davoren, "A new approach to the toxicity testing of carbon-based nanomaterials--the clonogenic assay," *Toxicology Letters,* vol. 174, pp. 49-60, Nov 1 2007.

[224] I. Beck-Speier, N. Dayal, E. Karg, K. L. Maier, G. Schumann, H. Schulz, M. Semmler, S. Takenaka, K. Stettmaier, W. Bors, A. Ghio, J. M. Samet, and J. Heyder, "Oxidative stress and lipid mediators induced in alveolar macrophages by ultrafine particles," *Free Radical Biology and Medicine,* vol. 38, pp. 1080-92, Apr 15 2005.

[225] J. A. Bourdon, A. T. Saber, N. R. Jacobsen, K. A. Jensen, A. M. Madsen, J. S. Lamson, H. Wallin, P. Moller, S. Loft, C. L. Yauk, and U. B. Vogel, "Carbon black nanoparticle instillation induces sustained inflammation and genotoxicity in mouse lung and liver," *Part Fibre Toxicol,* vol. 9, p. 5, 2012.

[226] SCCS. (2013). *OPINION ON Carbon Black (nano-form).* Available: http://ec.europa.eu/health/scientific_committees/consumer_safety/docs/sccs_o_14 4.pdf

[227] "Carbon black in the form of inhalable dust," in *The MAK-Collection for Occupational Health and Safety*, ed: Wiley-VCH Verlag GmbH & Co. KGaA, 2002.

[228] N. R. Jacobsen, G. Pojana, P. White, P. Møller, C. A. Cohn, K. Smith Korsholm, U. Vogel, A. Marcomini, S. Loft, and H. Wallin, "Genotoxicity, cytotoxicity, and reactive oxygen species induced by single-walled carbon nanotubes and C60 fullerenes in the FE1-Muta™Mouse lung epithelial cells," *Environmental and Molecular Mutagenesis,* vol. 49, pp. 476-487, 2008.

[229] A. Elder, R. Gelein, J. N. Finkelstein, K. E. Driscoll, J. Harkema, and G. Oberdörster, "Effects of Subchronically Inhaled Carbon Black in Three Species. I. Retention Kinetics, Lung Inflammation, and Histopathology," *Toxicological Sciences,* vol. 88, pp. 614-629, December 1, 2005 2005.

[230] P. J. A. Borm, G. Cakmak, E. Jermann, C. Weishaupt, P. Kempers, F. J. van Schooten, G. Oberdörster, and R. P. F. Schins, "Formation of PAH–DNA adducts after in vivo and vitro exposure of rats and lung cells to different commercial carbon blacks," *Toxicology and Applied Pharmacology,* vol. 205, pp. 157-167, 6/1/ 2005.

[231] J. Gallagher, R. Sams Ii, J. Inmon, R. Gelein, A. Elder, G. Oberdörster, and A. K. Prahalad, "Formation of 8-oxo-7,8-dihydro-2′-deoxyguanosine in rat lung DNA following subchronic inhalation of carbon black," *Toxicology and Applied Pharmacology,* vol. 190, pp. 224-231, 8/1/ 2003.

[232] E. J. Park, Y. M. Kim, S. W. Park, H. J. Kim, J. H. Lee, D. U. Lee, and K. C. Chang, "Induction of HO-1 through p38 MAPK/Nrf2 signaling pathway by ethanol extract of Inula helenium L. reduces inflammation in LPS-activated RAW 264.7 cells and CLP-induced septic mice," *Food Chem Toxicol,* vol. 55, pp. 386-95, May 2013.

[233] W. M. Haynes, *CRC handbook of chemistry and physics : a ready-reference book of chemical and physical data*. Boca Raton, FL.: CRC Press, 2011.

[234] N. C. Bell, C. Minelli, J. Tompkins, M. M. Stevens, and A. G. Shard, "Emerging Techniques for Submicrometer Particle Sizing Applied to Stöber Silica," *Langmuir,* vol. 28, pp. 10860-10872, 2012/07/24 2012.

[235] V. M. Masalov, N. S. Sukhinina, E. A. Kudrenko, and G. A. Emelchenko, "Mechanism of formation and nanostructure of Stöber silica particles," *Nanotechnology,* vol. 22, p. 275718, 2011.

[236] P. C. Van Metre, B. J. Mahler, and E. T. Furlong, "Urban Sprawl Leaves Its PAH Signature," *Environmental Science & Technology,* vol. 34, pp. 4064-4070, 2000/10/01 2000.

[237] S. Schraml, S. Will, and A. Leipertz, "Simultaneous Measurement of Soot Mass Concentration and Primary Particle Size in the Exhaust of a DI Diesel Engine by Time-Resolved Laser-Induced Incandescence (TIRE-LII)," *SAE Technical Paper,* vol. 1999-01-0146, pp. doi:10.4271/1999-01-0146, 1993.

[238] G. Lammel and T. Novakov, "Water nucleation properties of carbon black and diesel soot particles," *Atmospheric Environment,* vol. 29, pp. 813-823, 1995.

[239] M. Lapuerta, F. J. Martos, and J. M. Herreros, "Effect of engine operating conditions on the size of primary particles composing diesel soot agglomerates," *Journal of Aerosol Science,* vol. 38, pp. 455-466, 2007.

[240] B. David and P. Boule, "Phototransformation of hydrophobic pollutants in aqueous-medium .1. PAHs adsorbed on silica," *Chemosphere,* vol. 26, pp. 1617-1630, May 1993.

[241] H. Tatsumi, H. Nakase, K. Kano, and T. Ikeda, "Mechanistic study of the autoxidation of reduced flavin and quinone compounds," *J. Electroanal. Chem.Journal of Electroanalytical Chemistry,* vol. 443, pp. 236-242, Feb 1998.

[242] T. M. Sager, D. W. Porter, V. A. Robinson, W. G. Lindsley, D. E. Schwegler-Berry, and V. Castranova, "Improved method to disperse nanoparticles for in vitro and in vivo investigation of toxicity," *Nanotoxicology,* vol. 1, pp. 118-129, 2007.

[243] Y.-K. Kim, J.-W. Moon, J.-G. Lee, Y.-K. Baek, and S.-H. Hong, "Porous carbon-coated silica macroparticles as anode materials for lithium ion batteries: Effect of boric acid," *Journal of Power Sources,* vol. 272, pp. 689-695, 2014.

[244] J. Y. Park, S. H. Back, S.-J. Chang, S. J. Lee, K. G. Lee, and T. J. Park, "Dopamine-Assisted Synthesis of Carbon-Coated Silica for PCR Enhancement," *ACS Applied Materials & Interfaces,* vol. 7, pp. 15633-15640, 2015/07/22 2015.

[245] T. Kwon, H. Nishihara, Y. Fukura, K. Inde, N. Setoyama, Y. Fukushima, and T. Kyotani, "Carbon-coated mesoporous silica as an electrode material," *Microporous and Mesoporous Materials,* vol. 132, pp. 421-427, 2010.

APPENDIX A - Size distribution Histograms and EDX Spectra from Merced/Fresno.
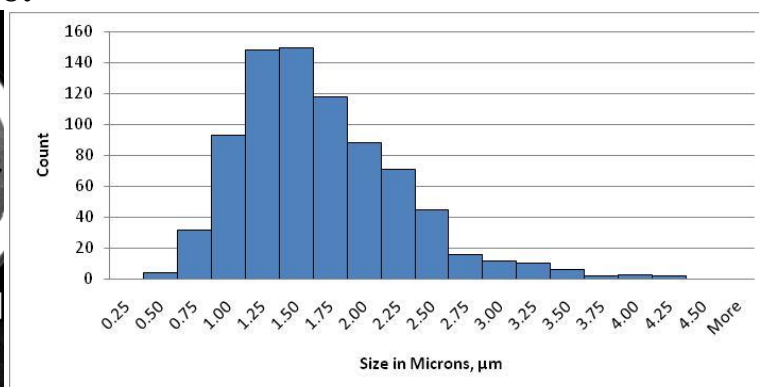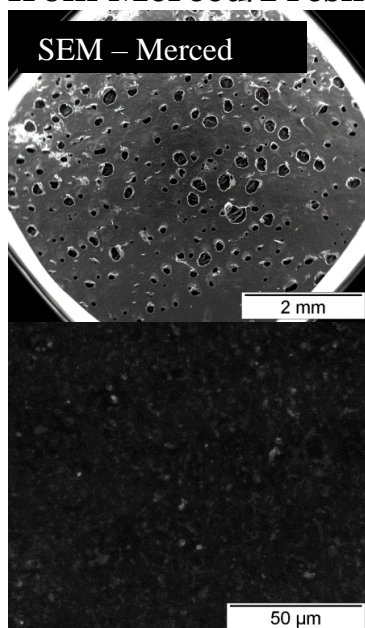
Count	800
Mean	1.56 µm
Minimum	0.43 µm
Maximum	4.14 µm
Standard Deviation	0.60 µm
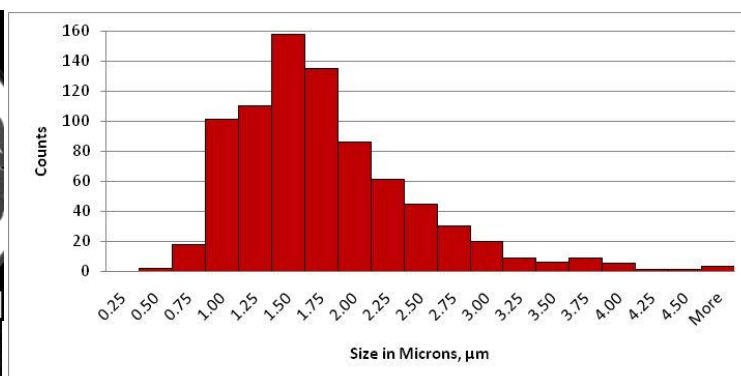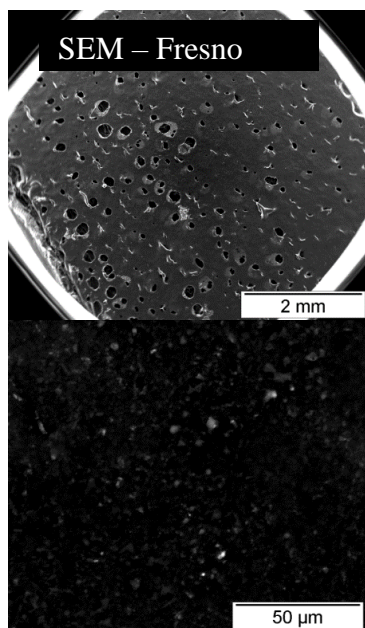
Count	800
Mean	1.65 µm
Minimum	0.32 µm
Maximum	7.39 µm
Standard Deviation	0.72 µm

**Figure A1**: Size Distribution and Histogram of Size Distributions of Merced and Fresno samples analyzed in SEM.
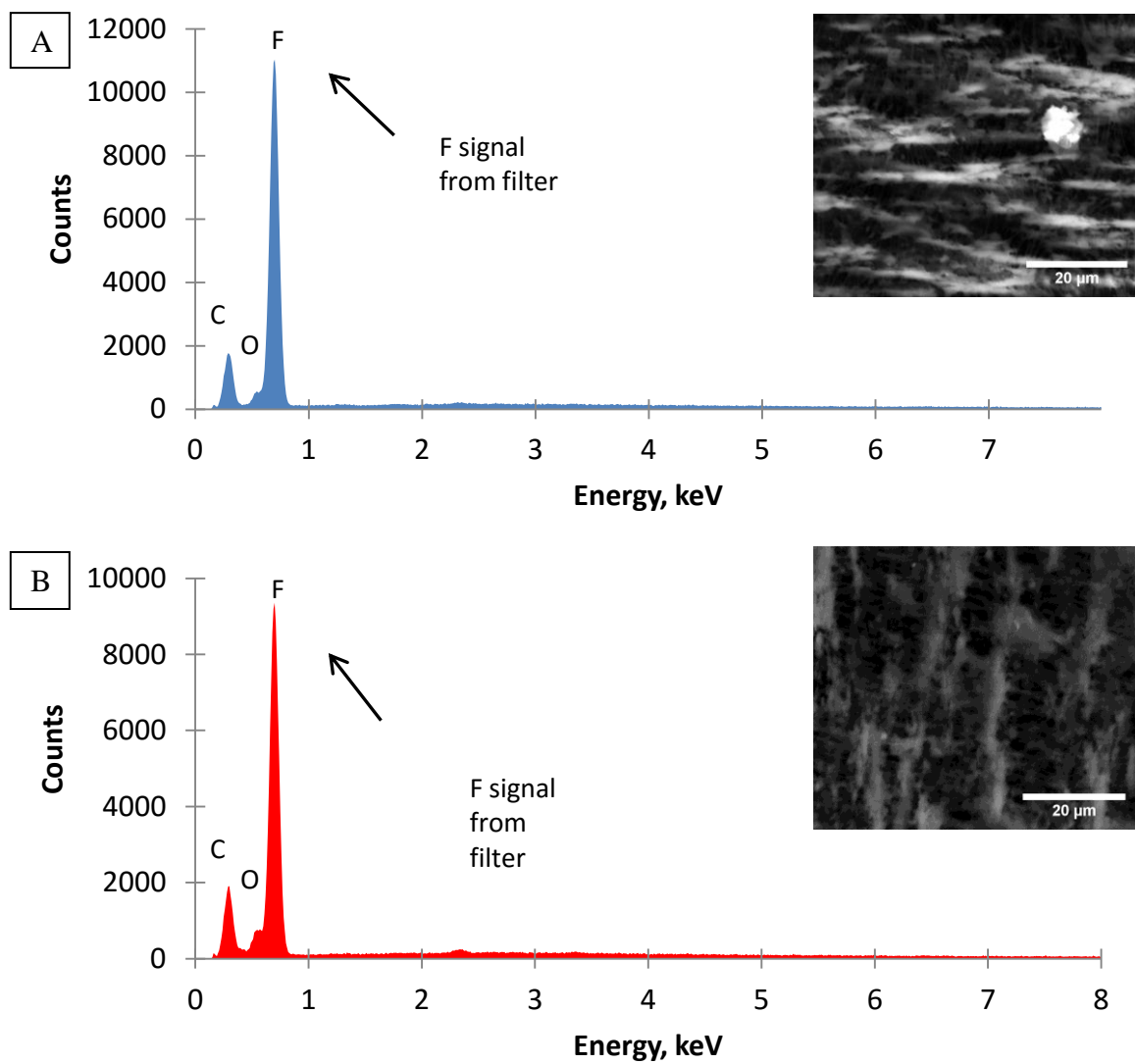
Figure A2: (A) Merced Air Particle filter and (B) Fresno Air Particle Filter analyzed using SEM with EDX.

Count	400	
Mean	43.0 nm	
Minimum	12.6 nm	
Maximum	124.2 nm	
Standard Deviation	15.6 nm	
Count	400	
Mean	40.0 nm	
Minimum	16.1 nm	
Maximum	93.6 nm	
Standard Deviation	12.9 nm	
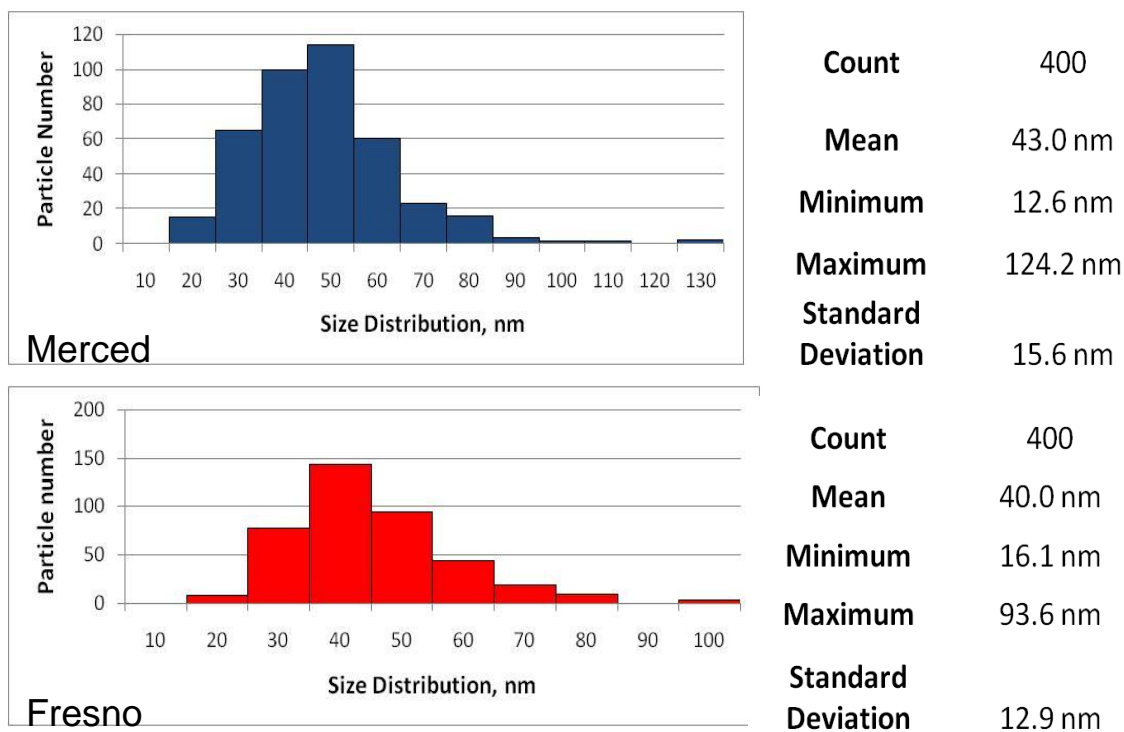
Figure A4: Size Distribution and Histogram of Size distributions using TEM.
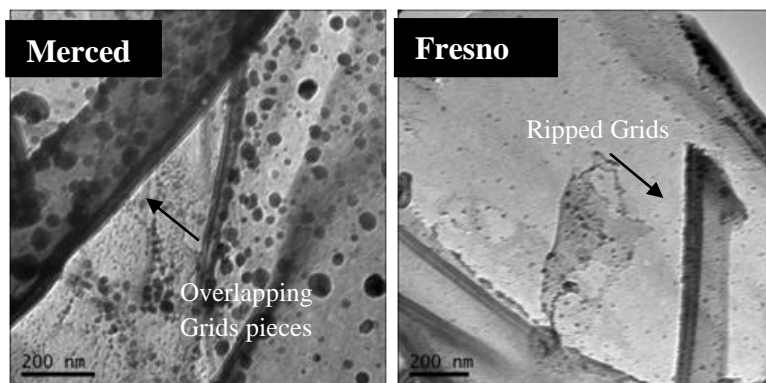
Figure A5: Merced (left) and Fresno (right) air particles using too much water to prepare TEM grid.
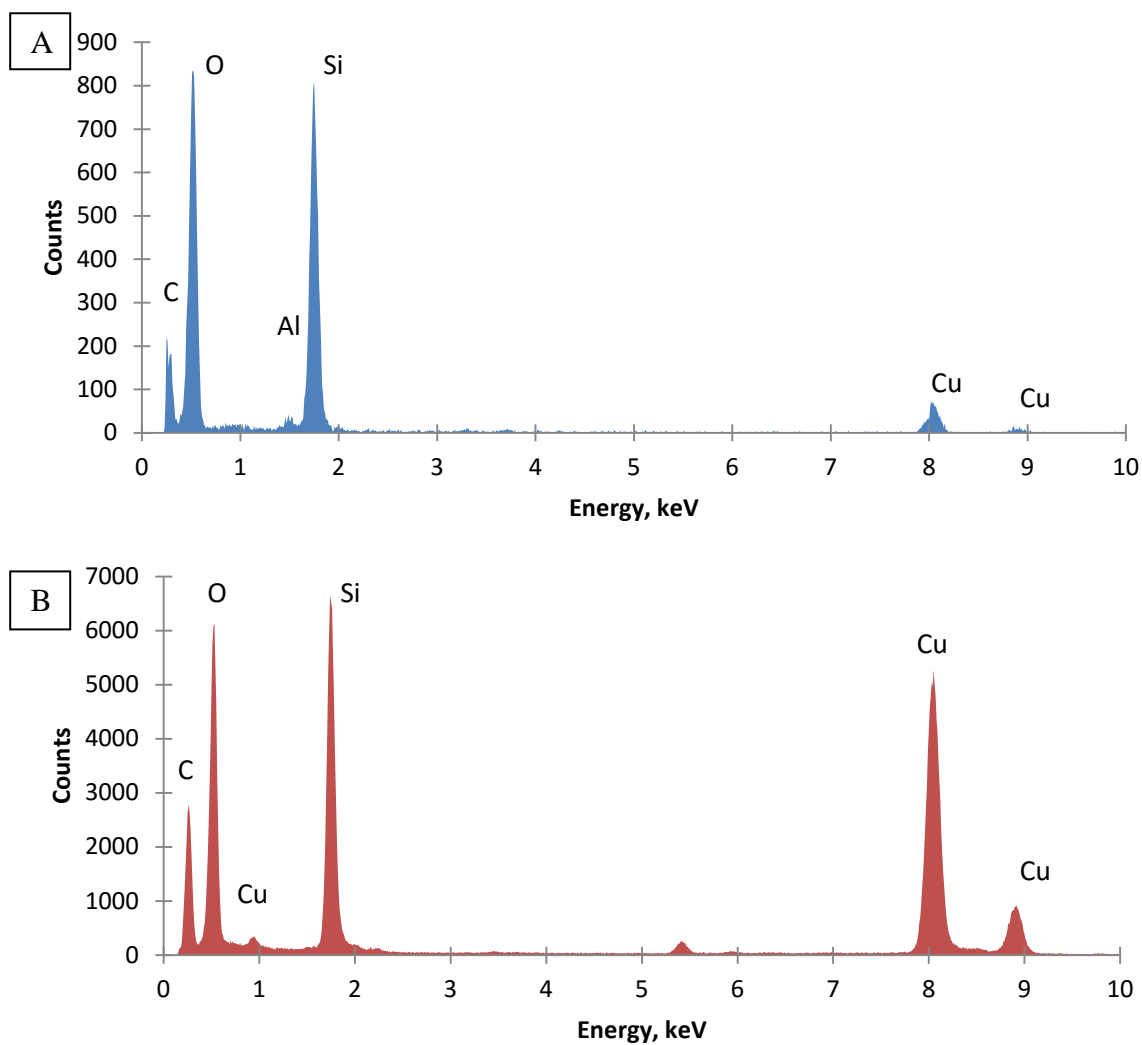
Figure A6. EDX spectra of (A) Merced and (B) Fresno air samples extracted using water.

APPENDIX B - TEM Micrographs from Automobile Shredder Plant Study
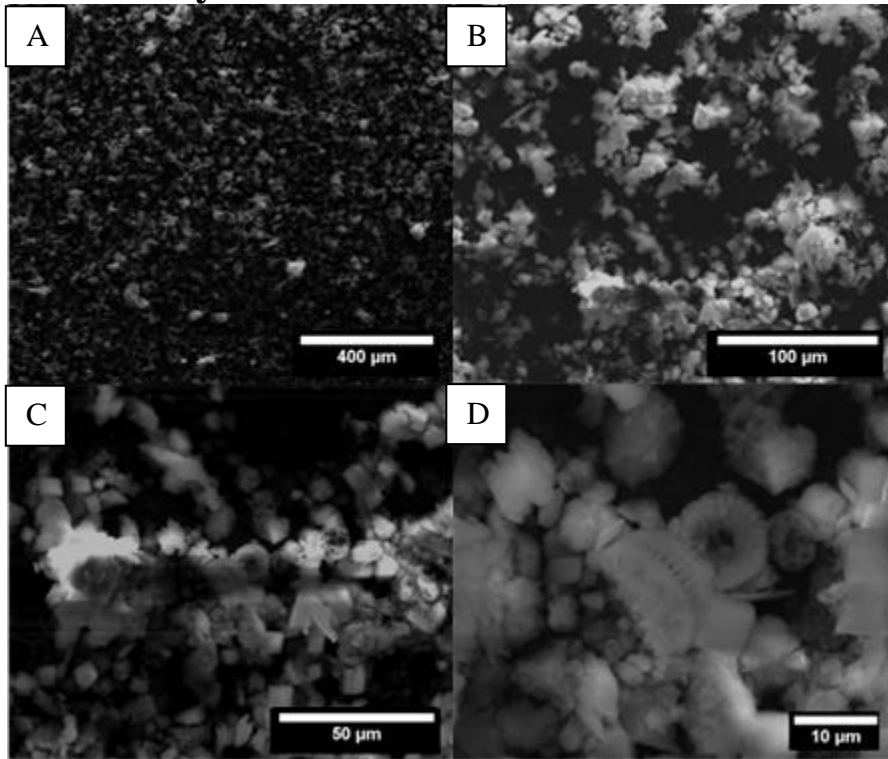
Figure B.1: Stage 1. Particles were separated to 10 to 5 µm size fraction.
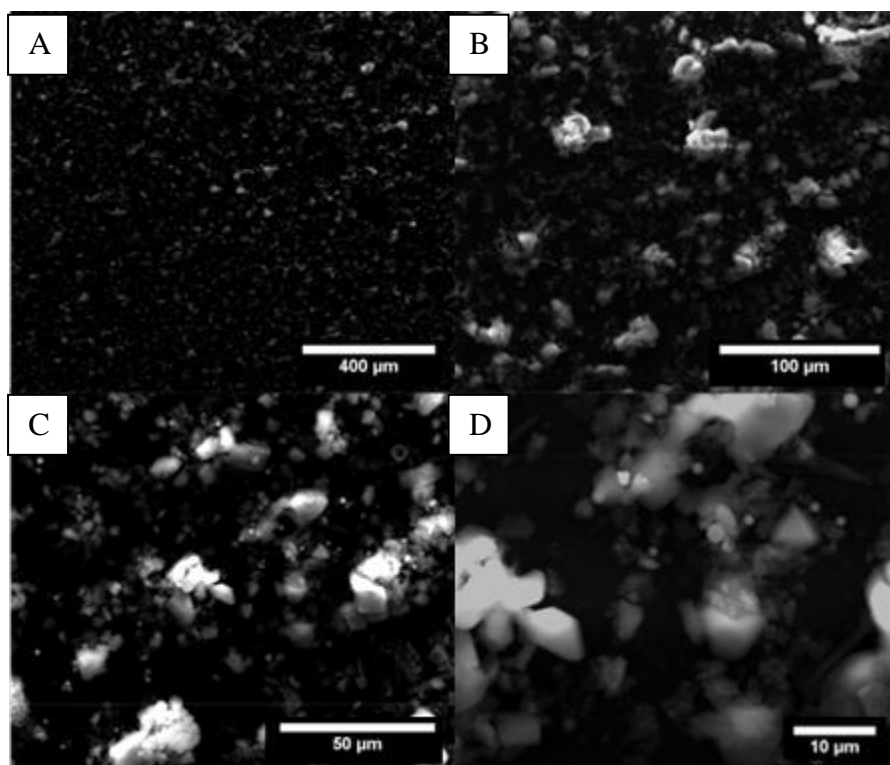
Figure B.2: Stage 2. Particles were separated to 5 to 2.5 µm size fraction.
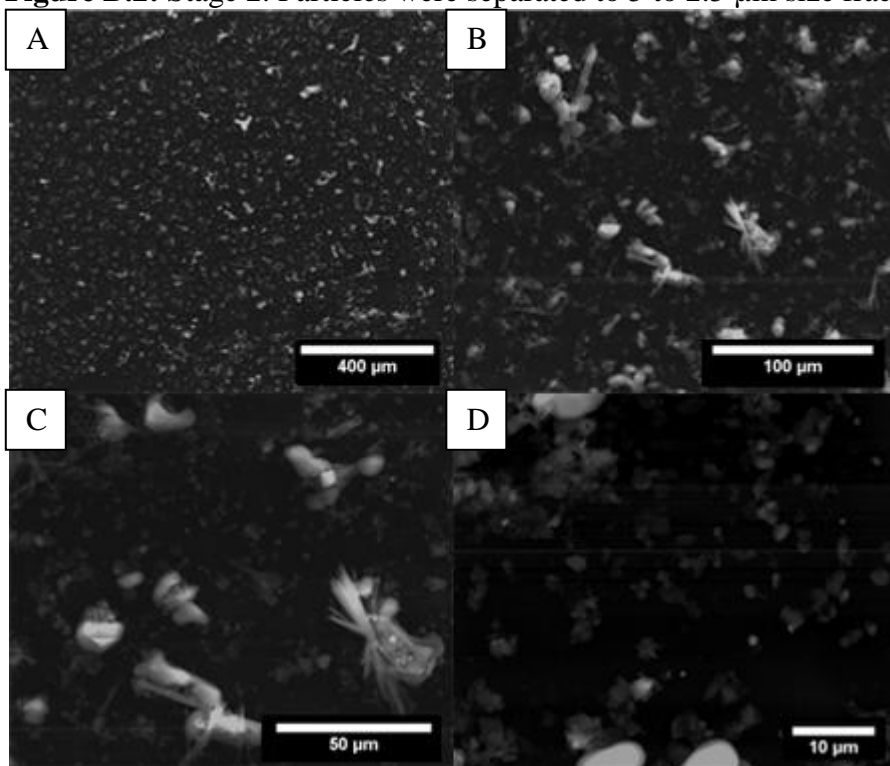
Figure B.3: Stage 3. Particles were separated to 2.5 to 1.15 µm size fraction.
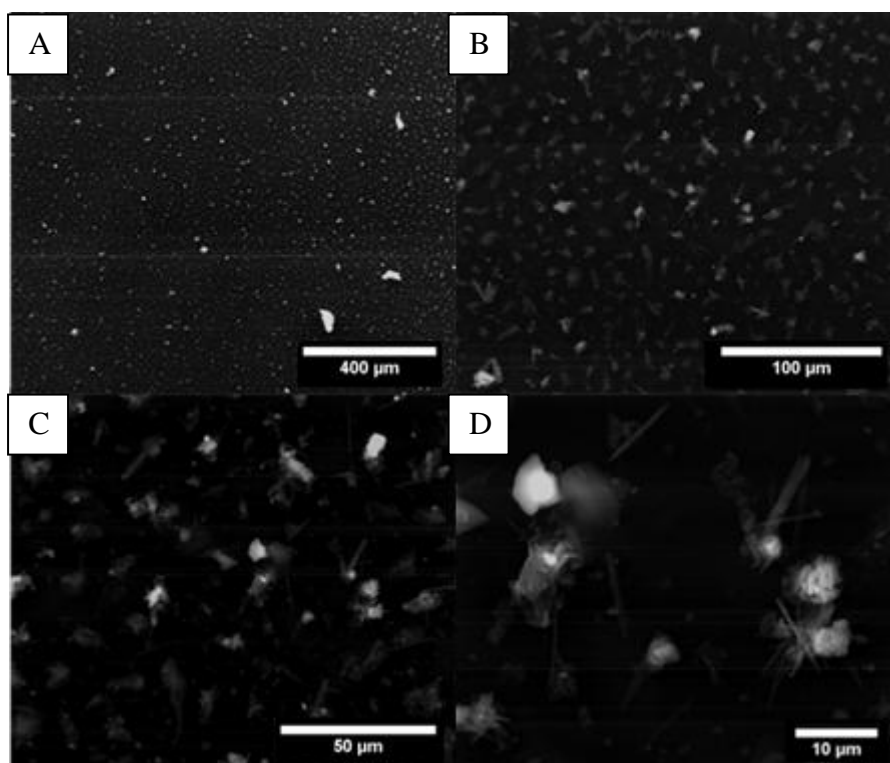
Figure B.4: Stage 4. Particles were separated to 1.15 to 0.75 µm size fraction.
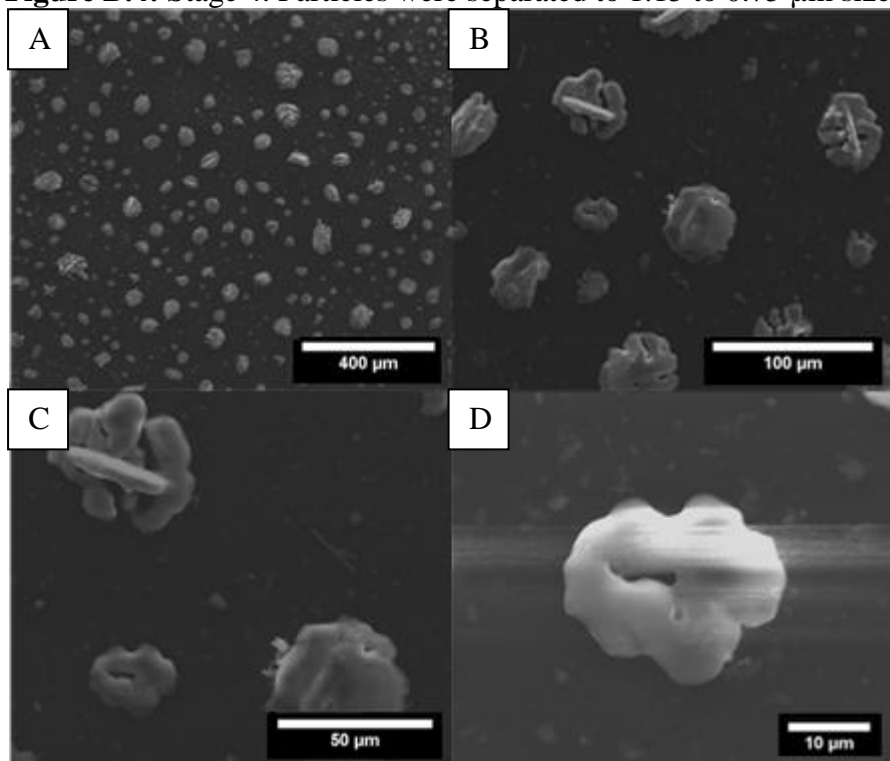
Figure B.5: Stage 5. Particles were separated to 0.75 to 0.56 µm size fraction.
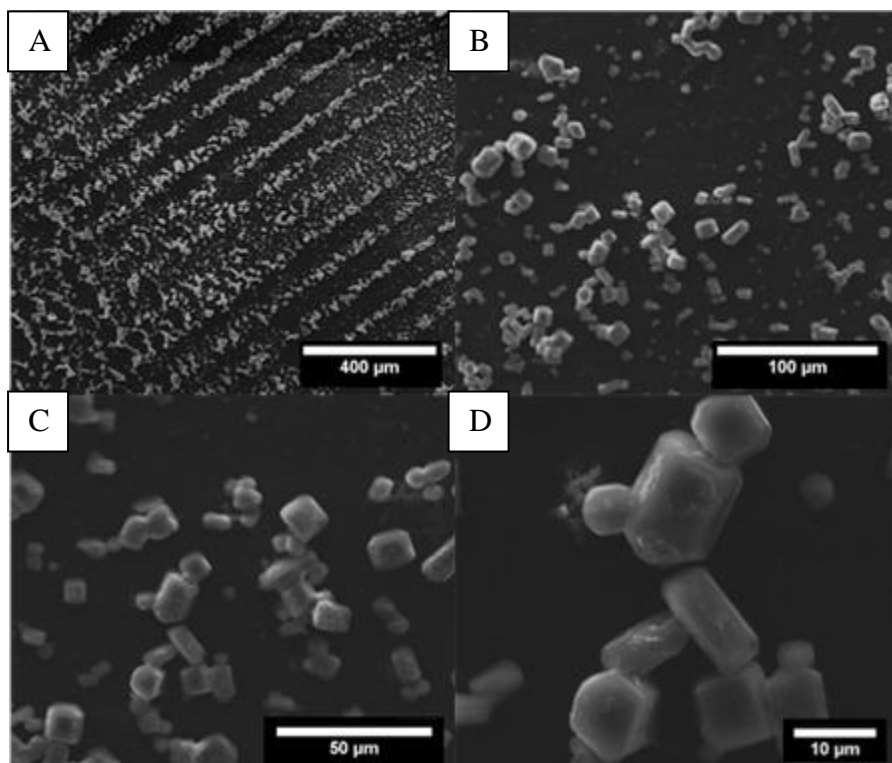
Figure B.6: Stage 6. Particles were separated to 0.56 to 0.34 µm size fraction.
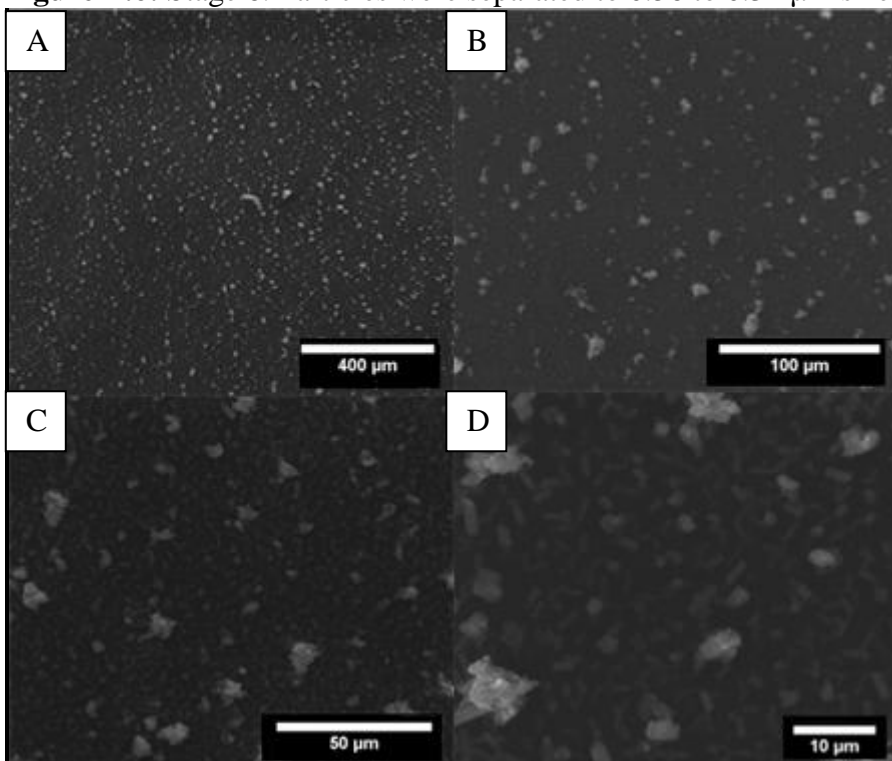
Figure B.7: Stage 7. Particles were separated to 0.34 to 0.26 µm size fraction.
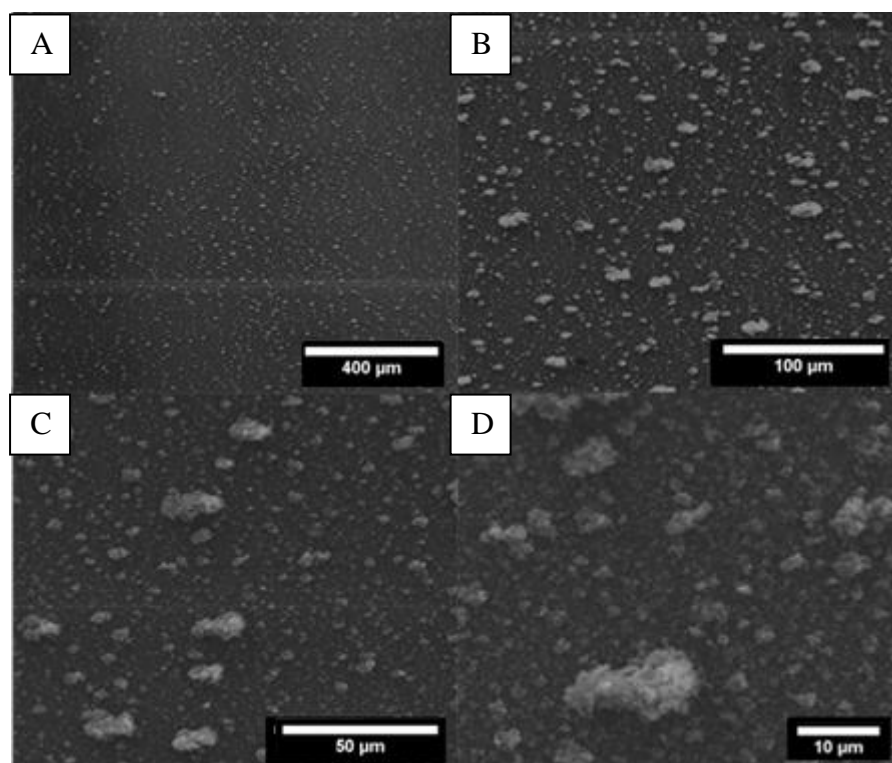
Figure B.8: Stage 8. Particles were separated to 0.26 to 0.09 µm size fraction.

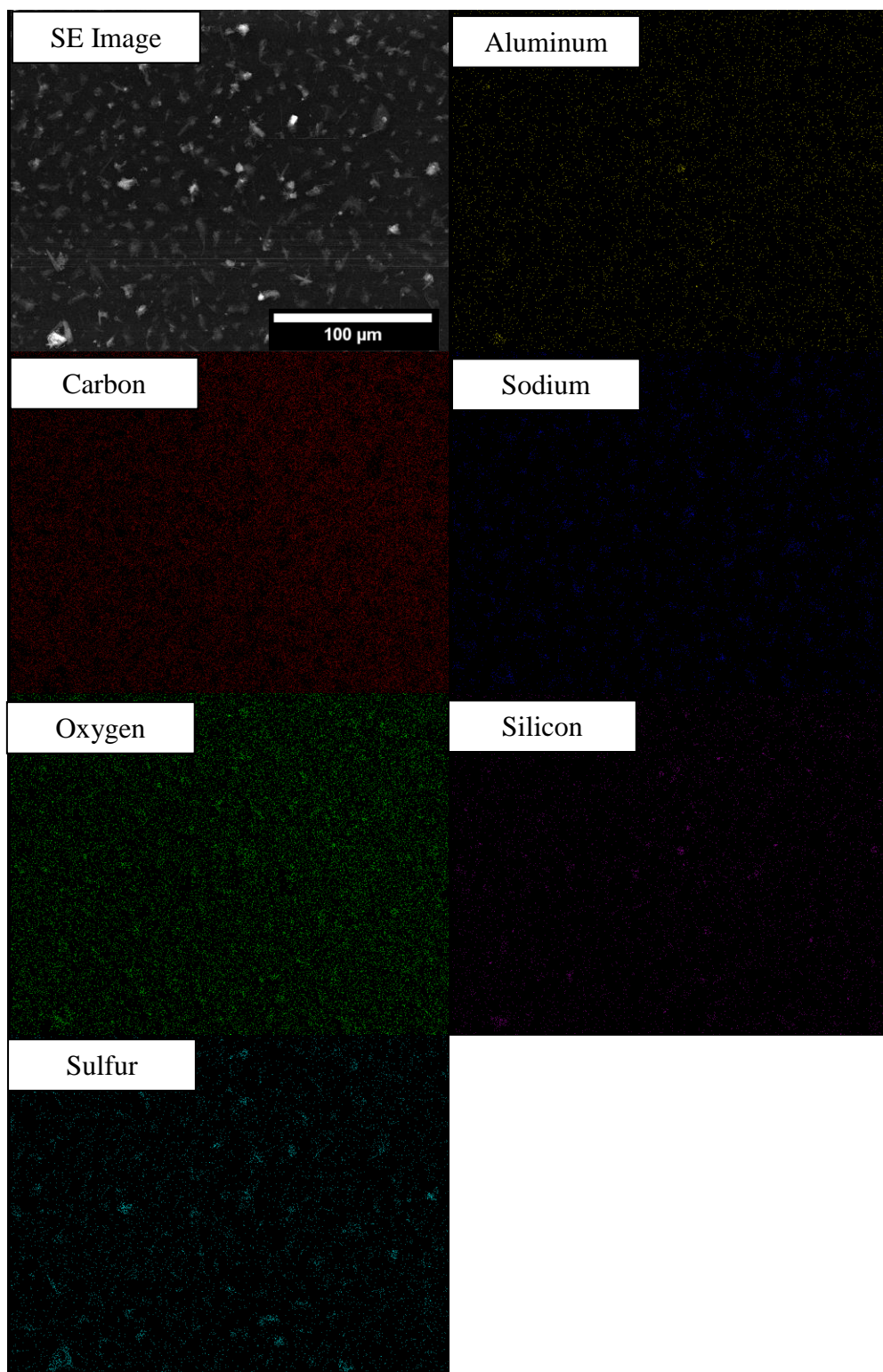# APPENDIX C - EDX Elemental Maps from Automobile Shredder Plant Study
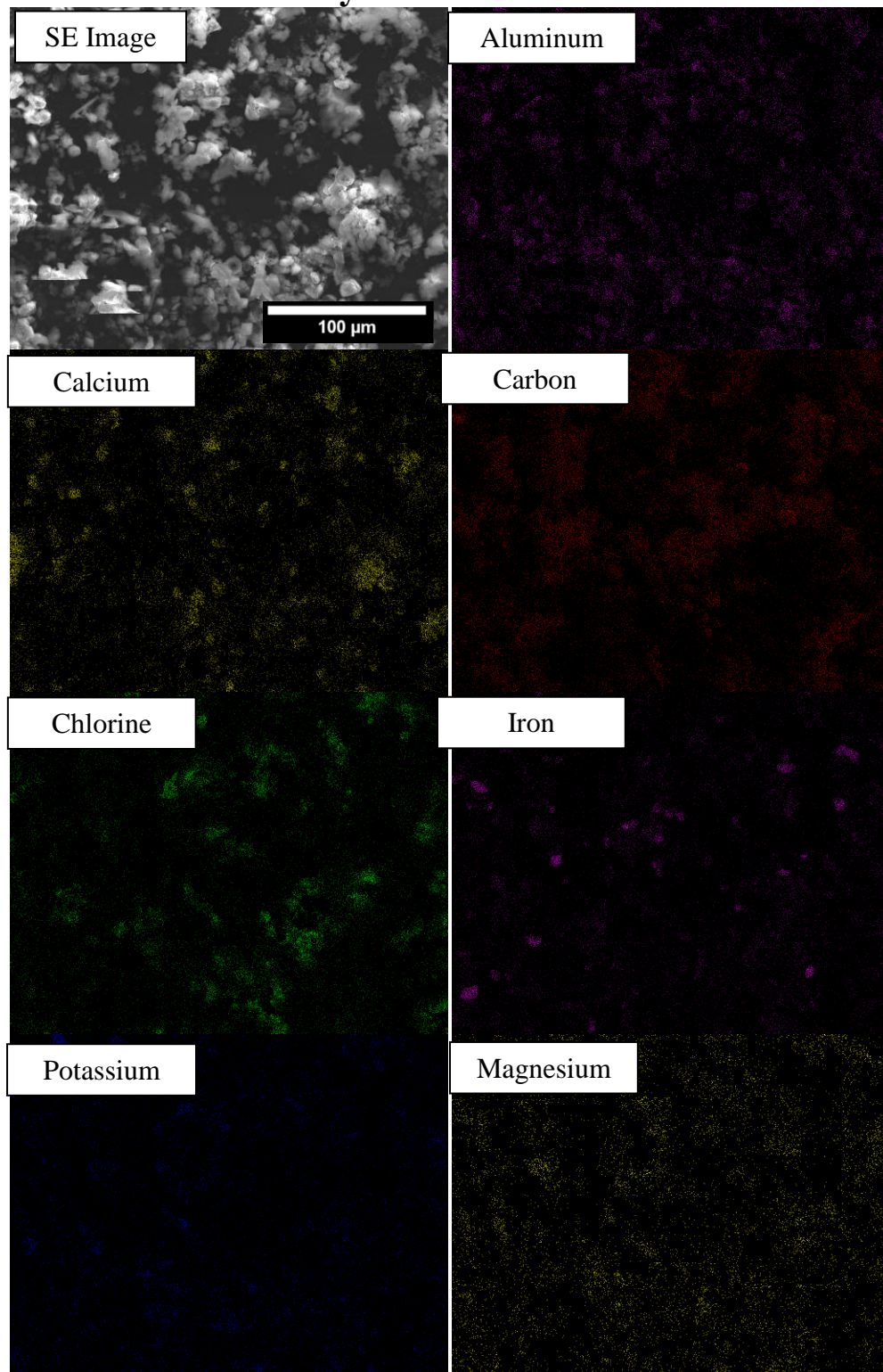
Figure C1: A) Stage 1A: EDX MAPs
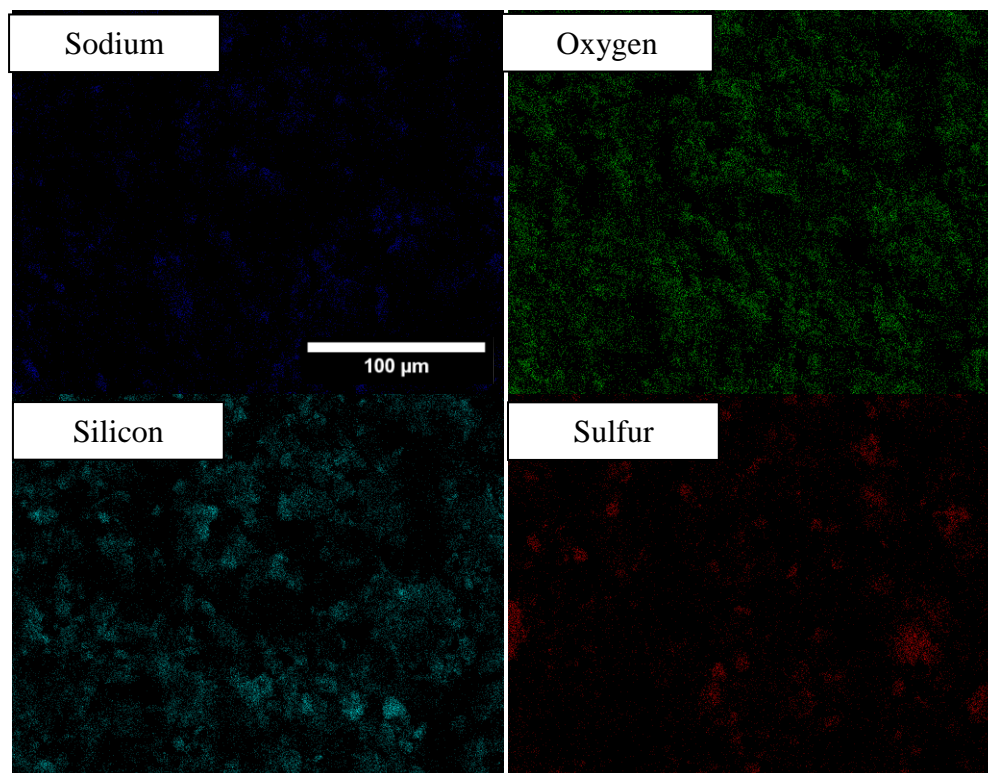
Figure C1. B) Stage 1B: EDX MAPs
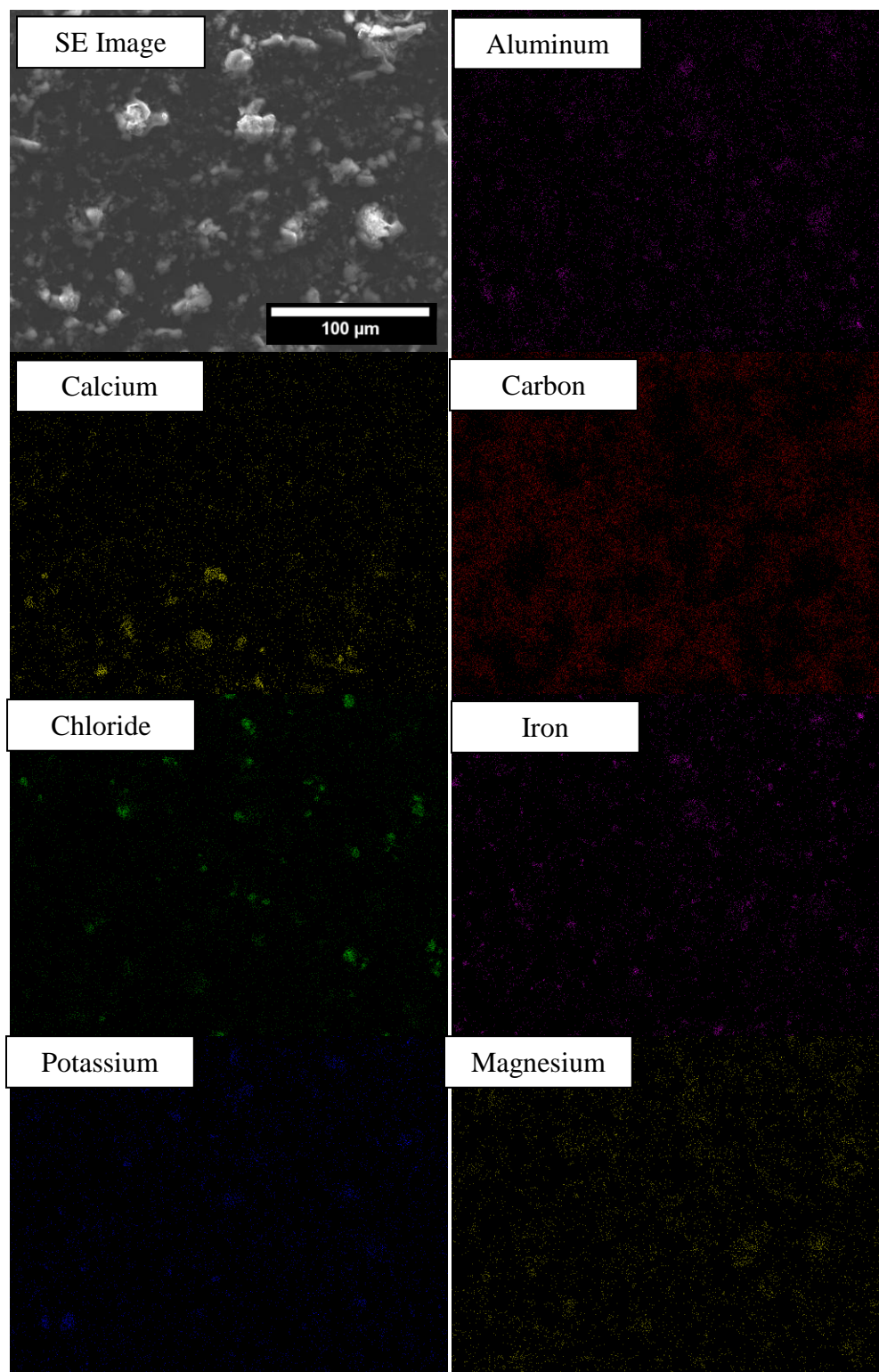
Figure C2. A) Stage 2A: EDX MAPs
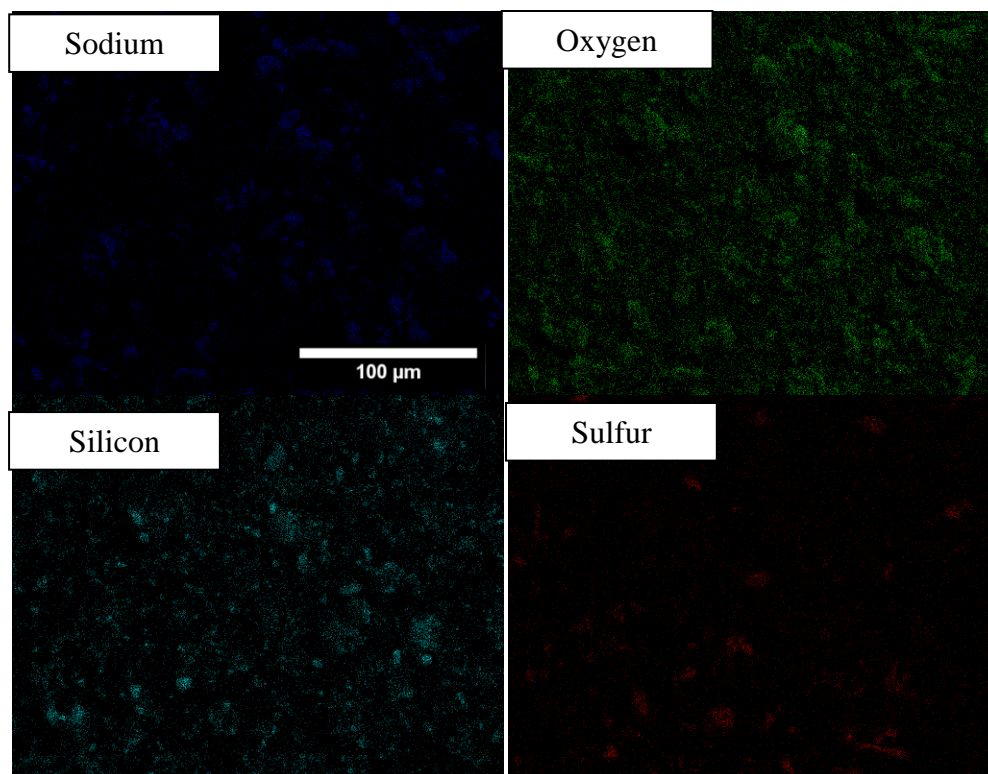
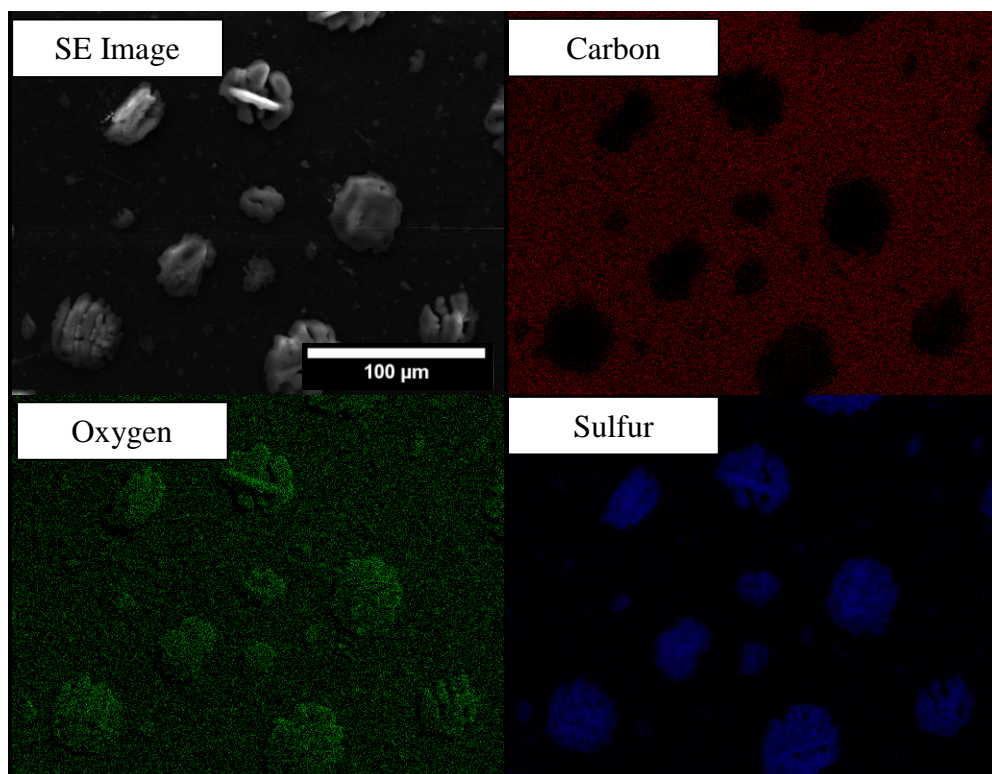**Figure C2. B) Stage 2B: EDX MAPs**
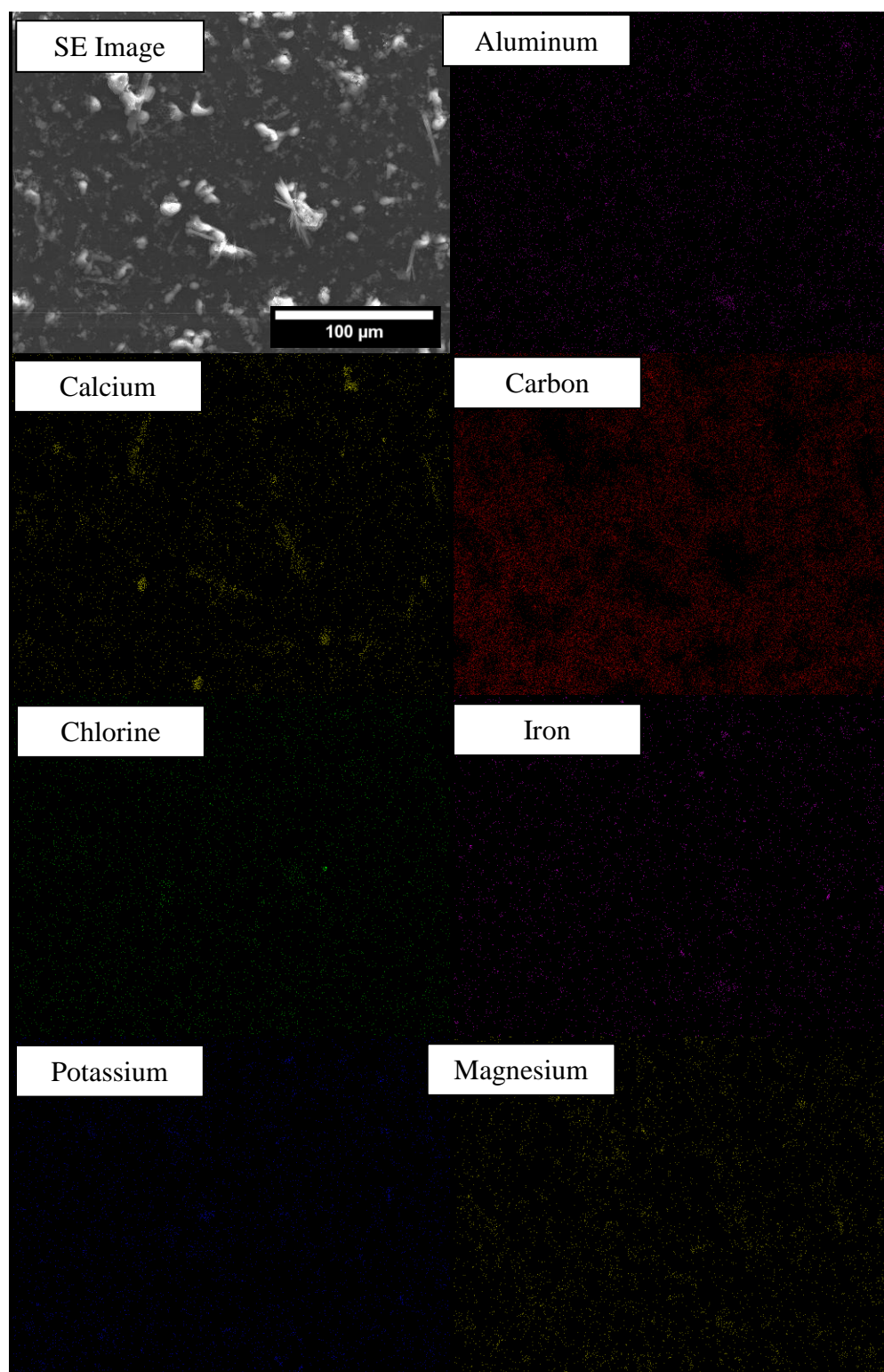
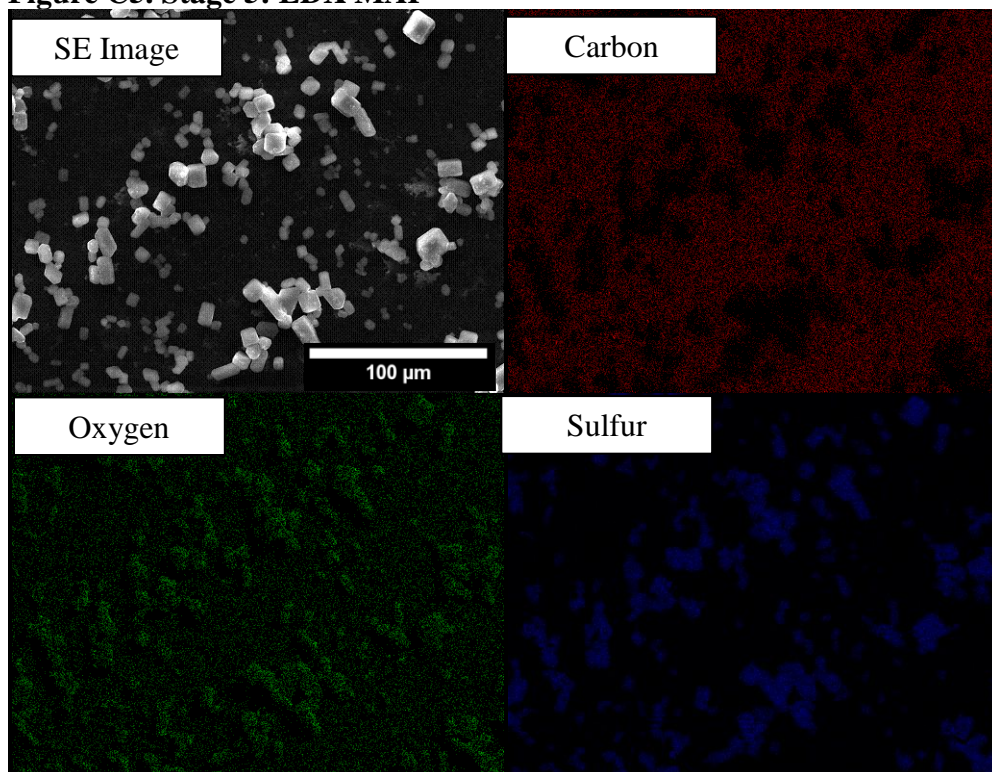**Figure C3. B) Stage 3B: EDX MAPs**
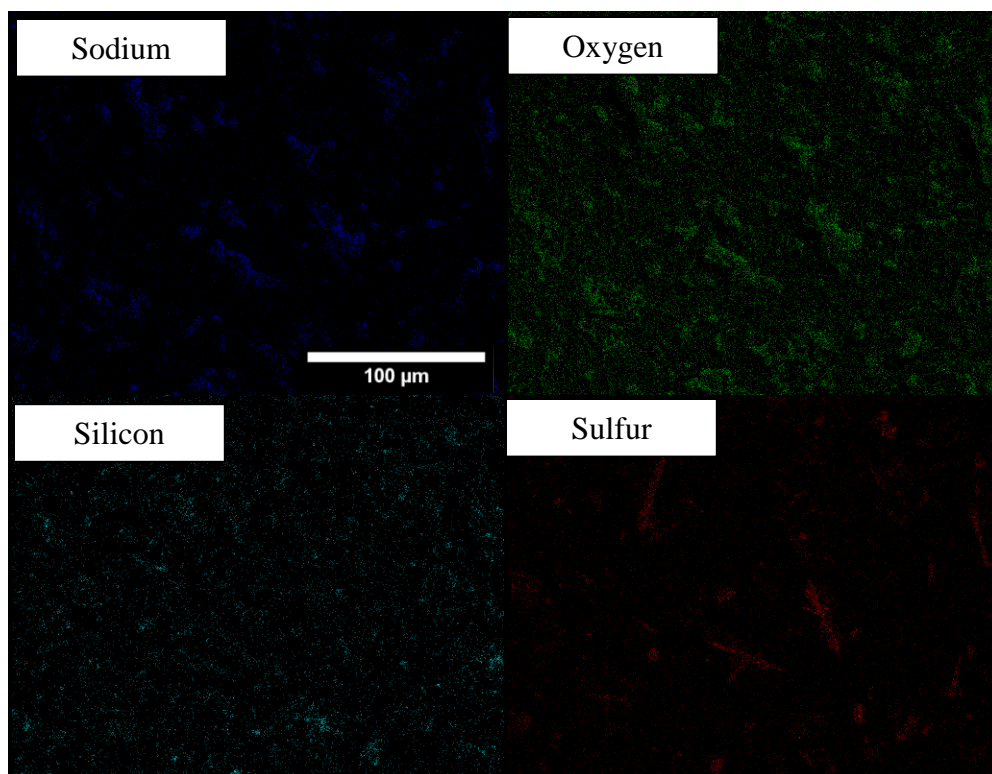
Figure C3. B) Stage 3B: EDX MAPs
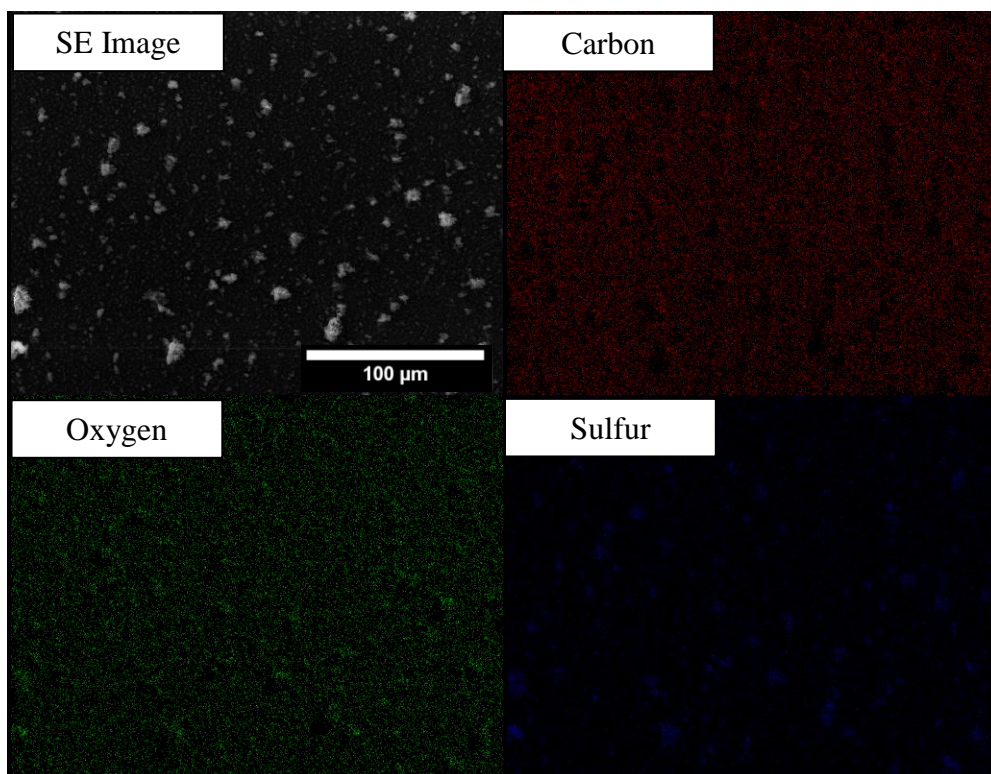
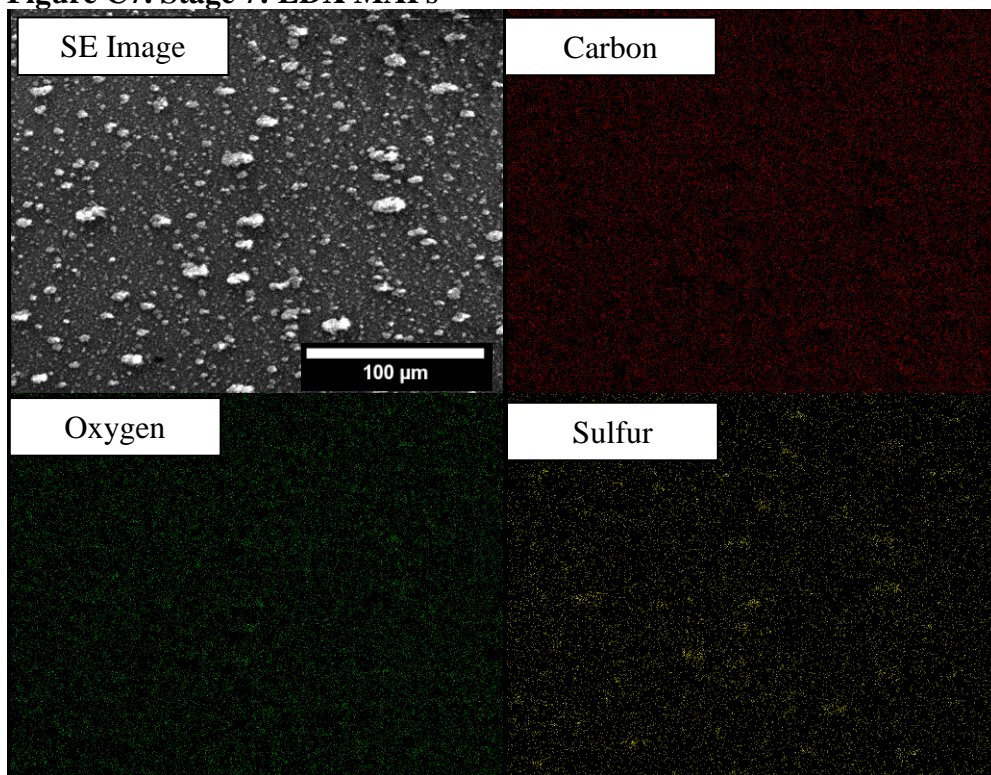**Figure C4. Stage 4: EDX MAPs**

Figure C5. Stage 5: EDX MAP

Figure C6. Stage 6: EDX MAPs

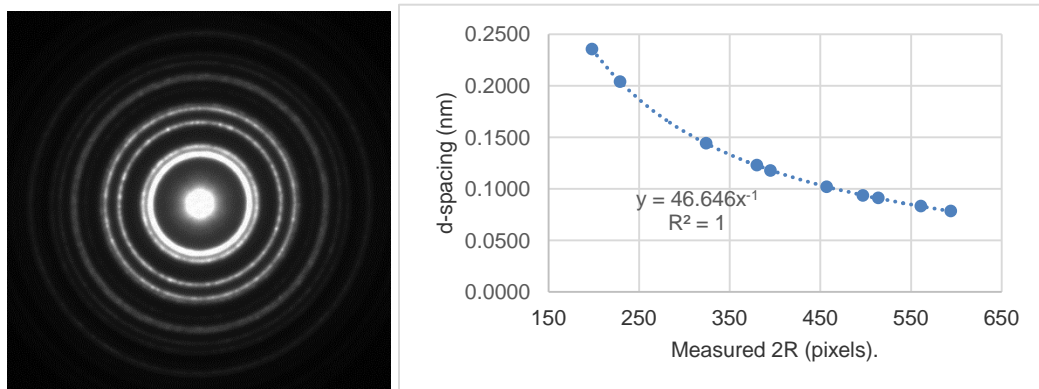**Figure C7. Stage 7: EDX MAPs**

Figure C8. Stage 8: EDX MAPs

APPENDIX D - Diffraction Calibration and References for Identification

Figure D1: Gold calibration for SAED. 2R is the ring diameter, so the calibration is 23.323 nm-pixels.

Gold	Pixels at L = 100cm	ring ratios	(hkl)	Theoretic values (nm)	Theoretic Rx/R1
R1	198	1.000	111	0.2354	1.000
R2	229	1.157	200	0.2039	1.155
R3	324	1.636	220	0.1442	1.633
R4	380	1.919	311	0.1230	1.915
R5	395	1.995	222	0.1177	2.000
R6	457	2.308	400	0.1020	2.309
R7	497	2.510	331	0.0936	2.517
R8	514	2.596	420	0.0912	2.582
R9	561	2.833	422	0.0832	2.828
R10	594	3.000	333,511	0.0785	3.000

Table B1: Calibration for gold on diffraction pattern
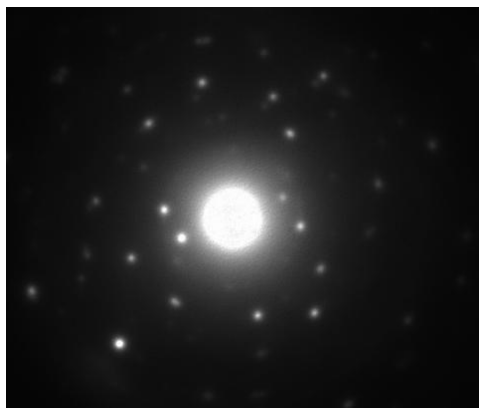
Measured (2R) = "x"	d-spacing (nm) = "y"
108.1	0.431
139.9	0.333
205.6	0.227
252.4	0.185
277.3	0.168
300	0.155

Figure D2: Iron Coated Commercial Silica Representative image and "spot pattern" SAED.

Iron Oxide Hydroxide		
FeOOH	Crystal structure: orthorhombic	
JCPDF#: 00-026-0792		
(hkl)	d-spacing, nm	Intensity in XRD
010	0.4446	20
110	0.3301	100
101	0.2554	80
011	0.2477	100
200	0.2462	60
020	0.2213	80
210	0.2152	80
120	0.202	60
021	0.178	40
211	0.1747	100
121	0.1674	100
220	0.1649	80
310	0.1542	60
002	0.1496	60
301	0.1442	80
012	0.1418	60

Table D.2: Iron Oxide Hydroxide JCPDF# 00-026-0792.

This was the closest matching iron oxide hydroxide.